Silica Particle Formation from Supersaturated Aqueous Solution and the Influence of Polymeric Additives

Von der Fakultät für Naturwissenschaften
der Universität Paderborn
genehmigte

Dissertation

zur Erlangung des Grades eines
Doktors der Naturwissenschaften

— Dr. rer. nat. —

von
Marina Elena Kley, geb. Sake
aus Paderborn

Juni 2017

Die vorliegende Arbeit entstand in der Zeit von Februar 2011 bis Juni 2017 im Fachbereich für Physikalische Chemie (Arbeitskreis Prof. Dr. Klaus Huber) der Fakultät für Naturwissenschaften der Universität Paderborn.

1. Gutachter: Prof. Dr. Klaus Huber
2. Gutachter: Prof. Dr. Wolfgang Bremser

Tag der Einreichung : 12.06.2017
Tag der mündlichen Prüfung: 13.07.2017

Hiermit erkläre ich, die vorliegende Dissertationsschrift selbstständig verfasst zu haben. Die dazu genutzte Literatur, zu Hilfeleistungen herangezogene Institutionen sowie Beiträge anderer Personen zu dieser Arbeit werden im Rahmen der Dissertationsschrift vollständig angegeben bzw. kenntlich gemacht. Teilergebnisse der vorliegenden Arbeit wurden in folgenden Artikeln vorab publiziert: Kley. M., Kempter, A. Boyko, V. and Huber, K., *Mechanistic Studies of Silica Polymerization from Supersaturated Aqueous Solutions by Means of Time-resolved Light Scattering*, Langmuir, **2014**, 30 (42), pp 12664–12674 bzw. zur Veröffentlichung bei Langmuir angenommen: Kley. M., Kempter, A. Boyko, V. and Huber, K., *Silica Polymerization from Supersaturated Dilute Solutions in the Presence of Alkaline Earth Salts*, Langmuir, **2017**.

Paderborn, Juni 2017

Marina Kley

Danksagung

An dieser Stelle möchte ich mich bei den Menschen bedanken, die auf unterschiedliche Art und Weise zum Gelingen der vorliegenden Dissertation beigetragen haben.

Mein Dank gilt zunächst Herrn Prof. Dr. Klaus Huber, für die Überlassung des Themas und die geduldige und kritische Betreuung dieser Arbeit. Seine stetige Bereitschaft Fragen zu beantworten und Hilfestellungen zu leisten habe ich sehr geschätzt. Die zahlreichen fachlichen Diskussionen mit ihm haben in unschätzbarer Weise zum Gelingen dieser Arbeit beigetragen.

Ein herzlicher Dank geht an die BASF Ludwigshafen für die finanzielle Unterstützung im Rahmen des Projektes „Polymer assisted silica polymerization“. Namentlich möchte ich mich vor allem bei Herrn Andreas Kempter und Herrn Volodymyr Boyko für die fruchtbare Kooperation, den regen Ideenaustausch und die wertvollen Diskussionen bedanken.

Bei Herrn Prof. Dr. Wolfgang Bremser bedanke ich mich herzlich für die bereitwillige Übernahme des Korreferats.

Für die freundschaftliche Atmosphäre, die gute Zusammenarbeit und die anregenden wissenschaftlichen Diskussionen bedanke ich mich herzlich bei allen ehemaligen und aktuellen Mitarbeiterinnen und Mitarbeitern des Arbeitskreises Huber.

Bei den Mitarbeiterinnen und Mitarbeitern der Physikalischen Chemie möchte ich mich für das kollegiale Arbeitsklima und die stetige Hilfsbereitschaft bedanken. Namentlich möchte ich mich ausdrücklich bei Frau Jünnemann-Held für die angenehme Zusammenarbeit im Labor und für die Unterstützung bei den Messungen mit der Molybdänblau Methode bedanken.

Meinen Schwestern, deren Familien und meinen langjährigen Freundinnen danke ich für die aufmunternden Gespräche und den großen Rückhalt, den sie mir gegeben haben.

Ein ganz besonderes Dankschön geht an meine Eltern, die mir meinen bisherigen Lebensweg ermöglicht und mich immer unterstützt und mir liebevoll zur Seite gestanden haben.

Mein innigster Dank gilt meinem Mann. Ich danke ihm von ganzem Herzen für sein großes Verständnis, seine Geduld und seine bedingungslose Unterstützung.

Kurzfassung

Für die Polymerisation von Silikaten aus übersättigter, wässriger Lösung wird ein 3-stufiger Mechanismus bestehend aus Nukleation, Partikelwachstum und Partikelagglomeration angenommen. Die vorliegende Arbeit untersucht den durch pH Erniedrigung induzierten Bildungsprozess der Silikatpartikel mittels zeitaufgelöster statischer und dynamischer Lichtstreuung. Diese liefern zusammen mit der zeitabhängigen, spektrophotometrischen Bestimmung der Monomerkonzentration mit Hilfe der Molybdänblau Methode umfassende Informationen sowohl der wachsendenden Partikel als auch der partikelbildenden Spezies. Das Partikelwachstum wird ausgehend von einer Lösung aus Natriumsilikat ($Na_2H_2SiO_4 \cdot 8H_2O$) in Wasser mit variabler SiO_2 Konzentration bei einer Temperatur von 37 °C im neutralen pH Bereich (pH 7 und pH 8) untersucht. Ein möglicher Einfluss von Metallkationen auf das Partikelwachstum wird durch Experimente in Gegenwart von $(Mg_{1/5}Ca_{4/5})Cl_2$ bzw. NaCl getestet. Die Ergebnisse ermöglichen die klare Unterscheidung der drei Wachstumsschritte und bestätigen das 3-Stufen Modell. Die Nukleation/Initiation ist bei geringer Übersättigung durch eine vom SiO_2 Gehalt und den Salzbedingungen abhängige Induktionszeit charakterisiert, während der weder eine signifikante Streuintensität noch ein Monomerverbrauch detektiert werden kann. Das Wachstum der Partikel setzt ein sobald ein Abfall der Monomerkonzentration bei gleichzeitigem Anstieg der molaren Masse M_w zu beobachten ist und endet beim Erreichen der SiO_2 Gleichgewichtskonzentration. Die Partikel wachsen gemäß eines Monomer-Additions-Mechanismus zu homogenen, kompakten Partikeln, Hinweise auf eine Ostwald-Reifung der Partikel können nicht gefunden werden. Der finale Radius R_h der Partikel liegt unterhalb von 20 nm und weist einen abfallenden Trend mit zunehmender SiO_2 Anfangskonzentration auf. Sofern die zeitliche Entwicklung von M_w durch die Monomer-Addition dominiert wird kann diese erfolgreich mit einem einfachen Modell, das eine Präkursorreaktion, Nukleation und Monomer-Additions-Wachstum umfasst, beschrieben werden. Oberhalb einer bestimmten vom pH Wert und vom Salzgehalt abhängigen SiO_2 Grenzkonzentration agglomerieren die in Schritt 2 generierten kompakten Partikel aufgrund zunehmender Partikel-Partikel Wechselwirkungen diffusionskontrolliert. Die resultierenden Agglomerate besitzen eine fraktale Dimension von 2 und sind aus Untereinheiten der gleichen Größe zusammengesetzt. Zusätzlich wird der Einfluss von drei Modellpolymeren (PEO, PA und AA-AMPS) im Hinblick auf einen inhibierenden Effekt auf den Partikelbildungsprozess untersucht. Obwohl PEO den Monomerverbrauch stark inhibiert, führt PEO in Gegenwart von Silikaten zur Flockenbildung. PA bildet in Gegenwart von divalenten Kationen kugelförmige Hybridaggregate aus Silikat und PA. Für AA-AMPS kann allerdings bei den vorliegenden Bedingungen kein Einfluss auf das Wachstum der Silikatpartikel festgestellt werden.

Abstract

Silica polymerization in aqueous solution is assumed to proceed according to a 3-step mechanism: nucleation, particle growth and agglomeration of particles. The present study applies time-resolved static and dynamic light scattering in combination with UV-vis spectrometry revealing the monomer consumption based on the molybdenum blue method to investigate the silica polymerization in solutions of sodium silicate ($Na_2H_2SiO_4 \cdot 8H_2O$) at a temperature of 37 °C. Particle formation was investigated at variable silica content at pH 7 and 8. Experiments were carried out in pure water and in the presence of either 5 mM of a mixture of $CaCl_2$ and $MgCl_2$ ($Ca : Mg = 4 : 1$) or 10 mM NaCl in order to analyse the impact of electrolytes on the process. With the results from the applied analytical methods we are able to unambiguously discriminate the three mechanistic steps of the silica polymerization. Experiments at low degree of supersaturation shows a characteristic lag-time, which depends in its length on the initial silica content and the salt conditions. During this lag-time neither a formation of particles nor a significant consumption of monomeric silica is observed. The growth stage starts with a loss of monomers, coinciding with an increase of the weight-averaged molar mass until the equilibrium concentration of silica is reached. Independent of the presence or absence of salt, particle growth in step 2 turned out to proceed via a monomer-addition process without being interfered significantly by Ostwald-ripening. The growing particles are compact with a homogeneous density. The final particle size lies below 20 nm, with an increasing trend with decreasing silica content. Independent of the salt conditions, evolution of the weight-averaged molar mass of experiments dominated by the monomer-addition growth of homogeneous particles, could be successfully described with a simple nucleation and growth model including a precursor reaction. Above a certain silica concentration, which depends on the level of added salt and the pH value, particle-particle interactions caused agglomeration following a diffusion-limited growth. The resulting agglomerates have a fractal dimension of 2 composed of the same constituent particles independent on the salt conditions. In addition, the influence of three model polymers (PEO, PA, and AA-AMPS) on the particle formation under salt and salt-free conditions was investigated. For PEO a good inhibition effect was observed. However, PEO is not able to reduce effectively silica depositions, as it promotes flocculation. In the presence of divalent cations PA led to the formation of spherical hybrid aggregates of silica and PA. An inhibition effect on the monomer concentration of silica was not observed. AA-AMPS had no significant influence on the formation of silica particles at the applied polymer concentration independent whether electrolytes were present or absent.

Contents

1. Introduction

Silicon is the second most common element on the earth, it is only surpassed by oxygen. More than one quarter, 26.3 % of the earth's crust consists of silicon. It has a great affinity to react with oxygen. The energy of a Si-O bond is twice as large as the energy for a Si-Si bond.[1] Therefore silicon can only be found chemically bound, mainly as salts of different silicic acids and never as a free element. Naturally silicon dioxide appears in eight different modifications as crystals. Examples are quartz, crystobalite and tridymite. Natural sources of amorphous silica is the anhydrous quartz glass, hydrous forms occur in opals and in sinter rocks. Plants use amorphous silica to stabilize special parts of their structure, silica can be found for example in blades of grass, in bamboo canes, in spines and in palm leafs. Also a few organisms like diatoms and sponges stabilize their skeleton with amorphous silica.[2] Silicon, silicates and silica are also very important as raw materials and as products in technical processes. Compounds with anionic silicon groups like SiO_3^{2-} and salts like Na_2SiO_3 are denoted as silicates. The term silica is a short designation for silicon dioxide in all its crystalline, amorphous and hydrated or hydroxylated forms.

Beside the use as natural building material (granite and sandstone) and as base for the production of cement, silicate glass, stoneware, ceramic and porcelain, the sol-gel chemistry of silica and the synthesis of zeolites opened new fields of technical applications. Of special interest for many applications is the synthesis of monodispersed and well-defined nanoparticles in size and mass. For this purpose the Stöber[3] synthesis has become a very popular route, in which ammonium tetraethylorthosilicate (TEOS) or tetramethylorthosilicate (TMOS) is used as precursor dissolved in a mixture of water and ethanol or methanol. Condensation and hydolysis of the alkoxysilanes strongly depends on parameters like the nature of the precursor and the catalyst, solvent, temperature and pH.[4] The effect of these parameters are well investigated and hence this procedure provides a very good control of the particle size. The silica structures can be modified by the type of catalyst. Large linear structures can be obtained via acid catalysis and branched structures can be achieved via base catalysis. The alkyl chain of the precursor has also an influence on hydrolysis and condensation reactions. Depending on the precursor either a three-silicon ring or a four-silicon ring dominates in the early stages of the process, which influences the structure of the material produced.[5] With respect to the mechanism the Stöber synthesis was the base for various studies on the nucleation and growth of silica particles. One approach is to monitor the particle growth by light scattering or small angle x-ray scattering (SAXS) techniques[6–10] or to follow the concentration of the different intermediates of the condensation process via ^{29}Si-NMR[11]. Detailed time-resolved characterization by means of these techniques provided information about the changes in physical and chemical properties of the particles synthesized via the Stöber process.[6,12]

Furthermore models describing this special particle growth have been introduced.[13]

Unlike to the previously mentioned investigations which have been performed with solutions with a relatively high degree of supersaturation, we want to focus on the formation of amorphous silica from solutions with a low degree of supersaturation. Silica concentrations in the investigated solutions are comparable with the silica content in soils and natural water. Unfortunately, the well-established models for the particle formation concerning the Stöber synthesis cannot be applied to the silica polymerization process under the conditions occurring in natural water. Analysis of the particle formation from low supersaturated, aqueous solutions can provide information, which are highly relevant in the following fields: (a) geologic processes, (b) biomineralization/bioinspired silification, (c) synthesis of zeolites and (d) inhibition of silica scaling in facilities of the water-treatment industry.

Dissolution and precipitation of silica can affect the permeability and the porosity of crustal rocks, which is highly relevant for various geologic processes. Kinetics of the formation of silica polymers play a critical role in thermally enhanced oil recovery and subsurface contaminant remediation, disposal of radioactive waste by burial and geothermal waste-waters by injection into the subsurface.[14]

Biological organisms are able to control the formation of hierarchically structured biominerals. These materials are composed of an inorganic component (e.g. silicon dioxide, calcium carbonate, calcium phosphate, iron dioxide) and an organic matrix, directing the morphology of the inorganic component. Hydrated silica ($SiO_2 \cdot n\ H_2O$) is assembled by protozoa, sponges, mollusks and higher plants to precise nano- and microstructures.[15] Synthetic silica is prepared from supersaturated solutions and under acidic conditions. In contrast, biosilification in organisms occurs in the mildly acidic or neutral pH regime and starts from undersaturated solutions (environmental concentration of inorganic material). One strategy of the biosilicifying organisms to overcome this problem is to concentrate and store silica in specialised vesicles[16]. Particularly the diatoms have developed mechanisms to generate various types of shell structures based on hydrated silica. Furtunately, the shell structure of the diatoms had been already extensively investigated via scanning electron microscopy in the past, as they served as a popular object to demonstrate the resolution of newly developed scanning electron microscopes. With the increasing industrial interest in porous silica materials for catalysis, adsorption and filtration, the investigation of the morphogenesis of the diatomic shell were promoted. It is known that the formation of the diatomic shell is linked to the cell cycle. The process can be divided into four stages. Uptake of inorganic material into the cell and storage in specialised vesicles. Synthesis of the organic matrix. Merging of the organic matrix and the inorganic component in a special compartment, usually also in a vesicle.[17] In the last step the primarily formed structure elements are merged to a three-dimensional framework. The mechanism of the fusion of the two materials is still unknown. By means of SEM investigations it has been found that silicic acid is pressed into a form which is also defined by small vesicles. These vesicles for example can be positioned as highest-density packed spheres. The resulting form of the diatomic shell is then a hexagonal honeycomb structure (see Figure 1.1). The mould-prepattern hypothesis postulated for the shell formation describes this process based on analytical results but does not explain the mechanistic features. It is still unset-

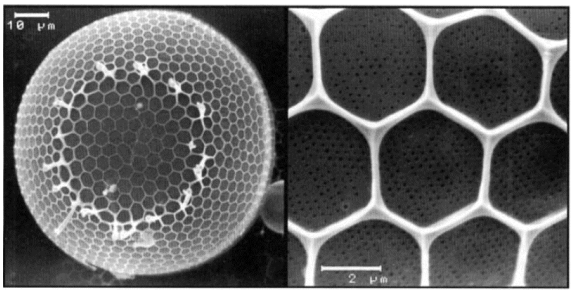

Figure 1.1.: SEM micrograph of the shell of the diatom *Stephanpyxis turris*. Total view of the shell (left) and close up of the hexagonal honeycomb structure with the underlying microporous membrane (right). From the review of D. Volkmer[17].

tled how exactly the various structures can be directed by the cell .[17] Another approach is the extraction of biomaterial from biosilicifying organisms and investigations of their composition and structure. Inspired by the properties of these materials the research field of bioinspired silification has developed and investigates the synthesis of biomimetic analogues. From the selective removal of biosilica and isolation of biomolecules it has been revealed that the additives play a key role in the process of silification, as they are able to control the rates of formation of oligomers and stable nuclei together with further properties like surface area, pore structure, particle size and aggregation patterns. Additives can be small inorganic or organic molecules as well as organic polymers, which are able to control the bioinspired silification in three ways: (i) by catalysis, (ii) by aggregation and (iii) by scaffolding.[18]

Zeolites as microporous materials have become very important for application in adsorption, catalysis and filtration. Among these, zeolites are of particular importance in catalysis e.g. for cracking of heavy hydrocarbons or gasoline production from methanol, as ion exchangers, or in other molecular sieve applications like sulfur elimination from gas streams.[19] Precise information about the formation of oligomers in the early stages of the growth process provide opportunities to control the morphology and porosity of the particles with suitable reaction conditions. The synthesis is based on silicate or alkoxysilane in alkaline solutions. The specific structure of the zeolites is caused by organic additives which act as structure-directing agents and play a key role in synthesis. The structure-directing effect of tetraalkylammonium ions should be emphasized which is strongly dependent on the length of the alkyl group. A very important intermediate species is the silicate octamer, which is preferentially formed in the presence of tetramethylammonium ions. It has a cubic structure, where the corners are occupied by the silicon atoms and the oxygen atoms build the bridges in between.[20]

Polycondensation of silicic acid in natural water is also important from an industrial point of view, because silica causes fouling and scaling on equipments like boilers and cooling towers in water-treatment facilities and on the membranes for reverse osmosis (RO) in desalination. Deposits on RO membranes lead to severe flux reduction and with that to restricted water recoveries in the desalination process.[21] This and high costs for

cleaning of such contaminated components has induced intensive investigations regarding the mechanism of silica polymerization in natural waters and the successful inhibition of the silica polymerization by polymeric additives.

A detailed knowledge of the mechanism and kinetics of the silica polymerization at variable conditions like the pH, salinity or temperature of the aqueous medium may unravel the role and importance of silica and reactions of silica in all the complex processes mentioned above and is expected to promote the development of routes to materials with specific properties leading to variable industrial applications and to an inhibition of the precipitation of silica, which is a challenging problem in many industrial processes.

1.1. Silica Polymerization

The following paragraphs present an overview about the behaviour of silica and polymerization reactions of silica in aqueous medium based on the review about silica chemistry provided by Iler[22] in the late seventies and several studies selected among the considerable number of works available today.

1.1.1. Silica in Aqueous Solution

The solubility limit of anhydrous, nonporous, amorphous SiO_2 lies around 70 ppm at 25 °C. Amorphous silica as small particles or porous aggregates exhibit a hydrated surface with Si(OH)-groups and hence has a solubility limit around 100-130 ppm SiO_2 which is higher than 70 ppm. A supersaturated solution of orthosilicic acid $Si(OH)_4$ can be prepared in two ways. Dissolution of silica in water at high temperature under high pressure followed by cooling on the one hand and dissolution of silica at high pH succeeded by acidification of the alkaline aqueous silica solution on the other hand. The latter approach has been followed in the present work.

Generally, supersaturated, aqueous solutions of silicic acid are thermodynamically unstable, as dehydration leads to condensation. Dissolution and deposition of silica in water always involves hydration and dehydration according to[22]:

$$[Si_nO_{2n-(nx/2)}(OH)_{nx}]+m\cdot Si(OH)_4 \rightleftharpoons [Si_{n+m}O_{2n-(nx/2)+2m(2-p)}(OH)_{nx+4(m-p)}]+2pm\cdot H_2O \tag{1.1}$$

where n is the number of silicon atoms in a polymer, x the number of OH groups per silicon atom in the polymer not exceeding 4, m the number of monomeric silicic acid added to the polymer and p the fraction of OH groups per monomeric silicic acid, that is converted to water during the polymerization reaction. n and m have to be integers and x and p are limited by the possible structures of polymers and conditions of polymerization.

From various theoretical studies it has been concluded that the condensation reaction of silica takes place via an ionic two-step mechanism illustrated in Figure 1.2. In a first step the negatively charged silica attacks the silicon atom of a neutral monomer, which results in a penta-coordinated intermediate. In a second step water is released.[23]

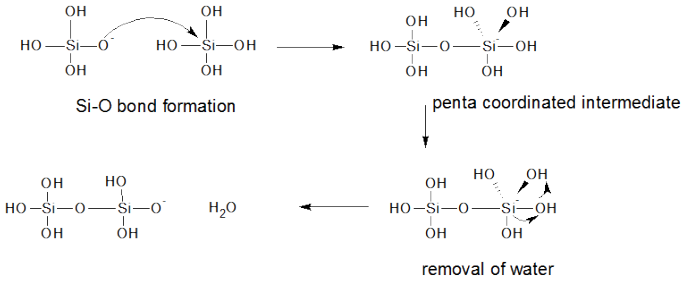

Figure 1.2.: Mechanism of silica condensation.[23]

Orthosilicic acid is a weak acid with a pK_a of 9.8 and undergoes oligomerization as soon as the solubility limit of amorphous silica (100-130 ppm SiO_2), which depends on temperature, pH and pressure, is exceeded. Oligomerization leads to the formation of dimers, trimers and small rings (3-ring and 4-ring) or higher linear oligomers. The pK_a of the oligomers is decreasing with increasing number of silicon atoms. For higher polymeric species the pK_a approaches a value of 6.7. This means that with increasing number of siloxane linkages and with decreasing number of OH groups on a silicon atom the acidity is increasing. From this and from the fact, that the condensation is a reaction of an ionized silanol group with a nonionized silanol group a few conclusions/facts can be derived. At low pH the dimerization is low, as the fraction of ionized $Si(OH)_4$ is very small. As soon as the concentration of dimers is increasing most of the reactions, which are happening, involve an ionized dimer due to the higher acidity of the dimer. If higher oligomers exists in the solutions like a linear tetramer or cyclic species, monomers and dimers will preferentially react with these (partially ionized) higher species to form polymers of higher molecular weight.[22]

On the basis of various works from different authors and Iler's[22] own extensive studies on the solubility of amorphous silica and the different parameters influencing the silica particle formation, Iler[22] postulated a mechanism for the silica polymerization process, which has become generally accepted. The condensation rate from supersaturated solution is proportional to the H^+-concentration for pH < 2 and proportional to the concentration of hydroxyl ions for pH > 2. The process of polymerization is based on three steps: nucleation, particle growth and agglomeration of the particles. The polymerization sets in with the formation of small cyclic oligomers because these structures enable them to form more siloxane bonds than other structures with the same number of Si atoms do. These small cyclic oligomers act as nuclei and grow by the addition of monomers to form condensed particles with an outer shell of SiOH groups. With increasing salinity and pH, the particles can also gel or precipitate via particle-particle agglomeration. In regimes where agglomeration is suppressed, Ostwald ripening may occur via dissolution of small particles and deposition of the resulting monomers on the larger particles. A schematic overview of this mechanism presumed by Iler[22] is shown in Figure 1.3.

At pH values higher than pH 2, where OH^- acts as catalyst two different pH regimes should be distinguished. The condensation of silica below and above pH 7. At a regime of $2 \leq pH \leq 7$ the condensation reaction is essentially slower than above pH

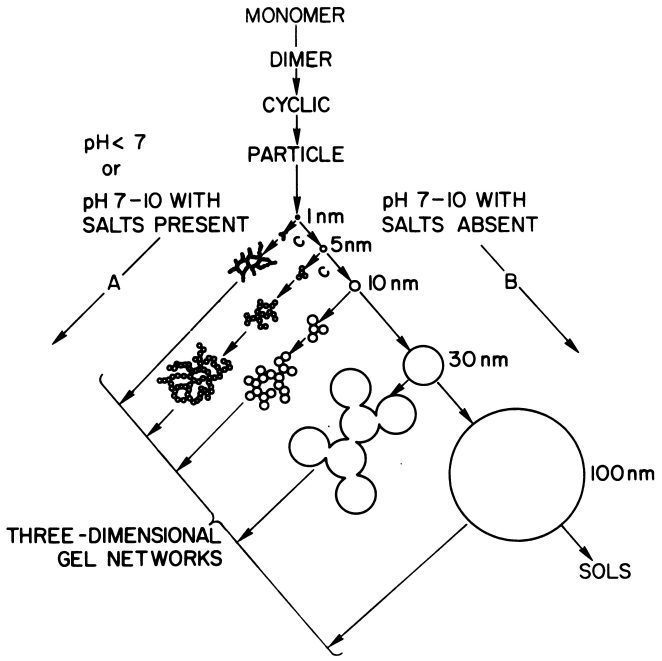

Figure 1.3.: Schematic overview of the mechanism for the silica polymerization postulated by Iler[22]. Depending on the conditions of the polymerization two pathways are possible: (A) Formation of a gel, (B) Formation of a sol.

7. Under acidic conditions silica particles bear no charges and already at small concentrations of the particles aggregation sets in. The particles reach diameters of 2-3 nm. In contrast at a pH above 7 the ionization of the polymeric species is much higher, therefore polymerization and depolymerization occurs very rapidly. Due to this, many mechanistic studies have been performed at low pH in order to be able to follow the polymerization of the monomeric silica or even at a decreased temperature to slow down the process. In general it is assumed that the mechanism of the formation of the primary particles is the same above and below pH 7. Only the aggregation of the primary particles to a three-dimensional gel differs below and above pH 7.

Weitz et al.[24] provided basic features of the mechanism of silica formation as they successfully combined the monitoring of the number averaged particle size by means of ultracentrifuge experiments with the recording of the monomer consumption via molybdate-reactive silica. Their investigation has been performed at 4000 ppm and pH 3. Given the existence of three species, monomers, oligomers and polymers, the results indicated loss of monomers accompanied with the formation of oligomers, followed by a coincidence of the onset of polymerization with the start of oligomer loss and further monomer consumption. Most likely, part of the oligomers like polycyclic octamers and decamers, which have also been observed in processes based on hydrolysis of silicic acid esters by ESI-MS[20,25,26] turn into nuclei and the nuclei grow by adding further monomers and oligomers. Alexander[27] performed experiments at pH 4.36 and observed a dependency of the number-averaged molecular mass according to $M \sim \sqrt{t}$

indicating a second-order reaction. Polymers formed at higher pH showed a slower reaction with molybdic acid. From this it was assumed that the particles formed at higher pH are internally more condensed. The reaction order of 2 at a pH of 2-5 was confirmed by a study of Okkerse[28]. Interestingly he found a dependency of the rate constant of the reaction expressed as a second order reaction on the initial silica concentration. A reason for that could be the phenomenon of a lag-time, which for the first time was observed by Baumann[29], who investigated monomer consumption close to neutral pH at variable silica contents and found sigmoidal curves of monomer concentration as a function of time. The curves indicate a lag-time preceding the actual monomer loss, which decreases with increasing silica concentration. The results could be nicely reconciled with nucleation which closes the lag-time and which is followed by growth via monomer addition. The final particle size determined from the solubility was 3 nm. Estimation of the particle size from the solubility is based on the fact that the solubility of silica is higher when the silica surface is convex, and lower when it is concave. It is a matter of the radius of curvature of the surface. The smaller the radius of the particles, which corresponds to a small positive curvature, the higher the solubility (see also Figure 1.5).[22] This dependency between particle radius and solubility is also known as Thompson-Gibbs effect. Alexander[30] was the first who could observe this behaviour experimentally. In a study on silica sols with a fixed ratio of SiO_2 : Na_2O also Iler[22] could show that the solubility of amorphous silica is decreasing with increasing diameter of the silica particles, whereas the size of the particles was determined by surface titration. However, it has to be conceded that the determination of the particle size from the solubility is only an indirect method and the solubility is influenced by impurities and the degree of hydration within the particles.[22]

Marsh et al.[31] published closely related results at a pH of 8, which confirms and extends the data of Baumann[29]. Furthermore Marsh et al.[31] determined a critical supersaturation ratio for the onset of nucleation to the order of 5-10. This lies in the same range as the value Iler[22] calculated as a critical supersaturation ratio for silica based on the assumption that the supersaturation ratio and the interfacial energy of silica follows the same relationship as for ionic materials. Furthermore Iler[22] assumed that supersaturated silica solutions undergo homogeneous nucleation, like ionic materials. The nucleus size of these ionic materials have been determined to 10-100 ions[32]. Based on this, Iler[22] postulated the same number of units for the nuclei of silica (10-100 SiO_2 units), corresponding to nuclei with a size of 1-2 nm and which grow in size up to a radius of a few nano-meters.

Makrides et al.[33] could confirm the existence of an induction period, already observed by Baumann[29] in case of a supersaturation less than 3. On the basis of a linear trend of the induction period with the inverse degree of supersaturation, Makrides et al.[33] postulated that the nuclei are predominantly formed during the induction period. They modeled this behaviour in terms of a simplified version of the classical nucleation theory that unlike to exact classical nucleation theory is based on a constant free energy of the activation for nucleation independent of the critical nuclei size leading to a nucleation rate constant that is independent of the degree of supersaturation.

An unsettled question concerning the silica polymerization is whether Ostwald-ripening sets in at the later stages of particle growth. One evidence for Ostwald-ripening

was given by the long-term study of Hoebbel and Wieker[34,35]. They aged silica solutions at pH 2 over 24 days following the concentrations of different oligomeric species and of the polymers identified via ^{23}Si-NMR. They could observe the initial formation of dimers and linear trimers followed by the formation of cyclic tetramers and then polycyclic species and three-dimensional polymers. Investigations on the reaction rate of the particles with molybdic acid made them to define a period of Ostwald-ripening for the time range between day 1 and day 8. They determined a decreasing rate constant with increasing size of the particles corresponding to an increase in the molecular weight. The size of the particles was determined by means of the solubility at the equilibrium state of the particles. However, these investigations were based on indirect determinations of the molecular weight and the particle size.

Richardson and Waddams[36] supplemented the mechanistic scheme by demonstrating that monomer consumption is fastest in the range of $7 < pH < 9$ with an optimum at $pH = 8.3$ and by demonstrating that the equilibrium concentrations approached at the end of the polymerization lies in the regime of 120-180 ppm. Adopting again the above mentioned correlation between experimentally accessible solubility and corresponding equilibrium particle size, final values for particle radii were estimated to lie in a range of 1.5-2.0 nm. Although, two further studies focused on the impact of temperature[37] and the influence of added salts[38] their detailed sets of data also supported the findings by the preceding works. Aside from this confirmation they also revealed a strong acceleration with the salt content[38] but only a moderate acceleration of the maximum reaction rate with temperature[37].

The acceleration of the monomer consumption with increasing concentration of an added salt was later confirmed by Icopini et al.[39], whereby the latter authors also identified a reaction rate for the monomer consumption of fourth order in terms of the monomer concentration interpreting this as a hint for tetramers to act as nuclei. Once the initial concentration of monomeric silica exceeded a certain level, the particles start to agglomerate[40], which at high enough silica concentrations appears as a macroscopic gelation.[24] As demonstrated by Merrill and Spencer[41], the exact level of the silica content where this agglomeration sets in depends on the salinity and pH of the solution.

Other researchers focus on the oligomerization of silica by using molecular dynamics simulations[23,42–45] in order to clarify the role of solvent molecules and counter ions for the formation of dimers, trimers and small rings. It could be found that the presence of sodium ions decreases the reaction rates of oligomerization for smaller chains. However, sodium is not directly coordinated to the silica, as this has been verified for other ions. In fact sodium is found in the second solvation shell of the reactive atoms. They postulated that sodium increases the reaction barriers for oligomerization by a rearrangement of the hydrogen bond network of the water around the reactants.

In two other recent contributions use could be made of modern scattering techniques in order to reveal further mechanistic details. Tobler et al.[46] performed time-resolved small angle x-ray scattering (SAXS) and dynamic light scattering at one angle together with the molybdate yellow based analysis of the depletion of monomeric silica at two different silica concentrations and succeeded to support the 3-step mechanism. In the first step, homogeneous nucleation leads to particles of 1-2 nm inferred from an ex-

trapolation of the kinetic model fits to time zero, in agreement with Iler[22], who already assumed that the silica polymerization follows a homogeneous nucleation. Iler speculated that the nucleation may be similar to that of ionic materials. Surprisingly, the resulting size coincides with the value evaluated by Tobler[46] based on the SAXS measurements. As a second step Tobler et al.[46] identified particles growing to a size not larger than 4 nm. It is the kinetic modelling of this step which establishes a key feature of the work by Tobler et al.[46] and which reveals a particle growth by surface controlled monomer incorporation. However, no clear picture could be provided of the morphology of the particles growing in this step. Do those particles have a spherical shape or do they have a mass fractal nature? The third stage was postulated by Tobler et al.[46] to include Ostwald-ripening and growth via particle-particle aggregation discernible by a steep increase of particle size values to radii close to 30 nm.

New insight into the origin of the lag-time is provided by Noguera et al.[47], who published a computational approach based on the classical nucleation theory. They applied successfully their model on experimental data from Rothbaum and Rhode[37] and Tobler et al.[46,48]. Initiation of the silica polymerization in those studies was performed via pre-established initial supersaturation, via neutralization of a high pH solution of silica and via fast cooling. It turned out that the properties of the particle population strongly depend on the experimental conditions. Further on Noguera et al.[47] postulated that the plateaus in silica concentration denoted as induction period in previous publications have to be rather attributed to a stage in which nucleation, growth and dissolution compete with and compensate each other. An induction period related to a non-stationary nucleation theory according to Kashiev[49,50] was excluded by Noguera et al.[47] because experimental results lack the corresponding dependency of the induction time on the initial supersaturation.

1.1.2. Aggregation and Gel Formation

Aggregation and gelling of the amorphous silica particles formed from supersaturated solutions via condensation reactions following the mechanism described in Chapter 1.1.1 depend on the concentration of the silica particles and on their surface charges. Uncharged amorphous silica particles aggregate to branched chains and further to a three-dimensional network and finally to a gel. This is also the case if negative charges on the surface of the particles are screened by counter ions. The general effect of the pH on the relative gel time is schematically given by Figure 1.4. The maximum stability of a sol is at pH 1.5-3 and the minimum stability is at pH 5-6. In the absence of salts above pH 7 no gel is formed, since the particles are highly charged and repel each other. The salt effect is dominating at high pH as under these conditions the silica particles are charged, counter ions can screen the charges and induce gelling. At low pH the addition of salt has only a minor effect.[22] The curve in the presence of sodium salts corresponds to a salt concentration higher than 0.2 –0.3 N.

The formation of branched chains and a three-dimensional network is only possible if the depolymerization or hydrolysis of silica is unfavoured and the condensation is irreversible. Otherwise rearrangement would be possible and the polymers would have

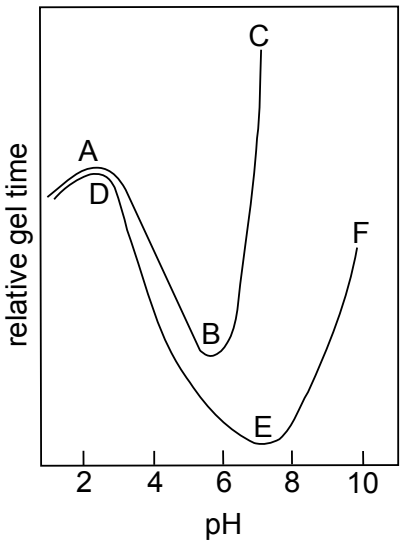

Figure 1.4.: Relative gel time of a silica sol in the absence of sodium salt (A-C) and in the presence of sodium salt (D-F).[22]

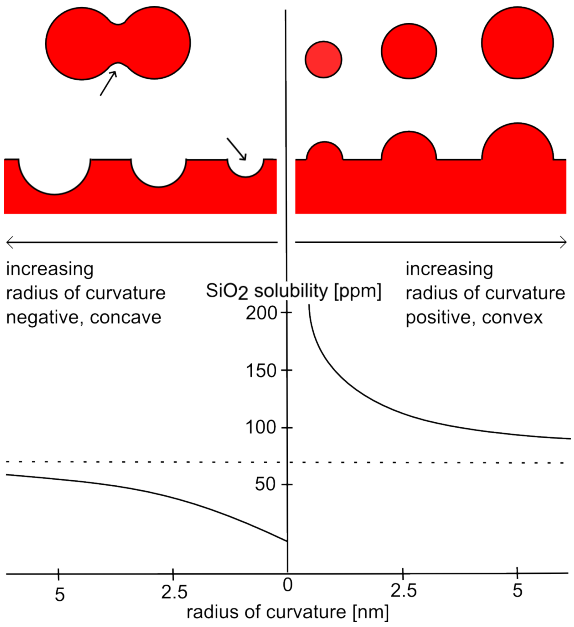

Figure 1.5.: Solubility of amorphous silica with radius of curvature. Silica solutions can contain positive curvatures (convex), shown as cross-section of the particles and as bulges on a silica surface as well as negative curvatures (concave), shown as holes on the silica surface and as the crevice between two particles. The dashed line indicates the solubility of anhydrous, non-porous SiO_2.

the opportunity to form again spherical structures. It has been experienced that the same factors which promote condensation of monomers also promote the aggregation of silica particles. Therefore it is assumed that the linkage between the primary particles in the chains is based on Si-O-Si bonds and not only on adhesion. It was already mentioned in Chapter 1.1.1 that the solubility of amorphous silica depends on the surface curvature of the particles. Figure 1.5 illustrates the general dependency of the solubility of amorphous silica on the radius of curvature. Small silica particles with a small convex curvature have a higher solubility than larger particles. In the limiting case of a very small concave curvature the solubility approaches zero. This case is fulfilled at the contact point of two silica particles sticking together. As a result, monomers are instantly deposited around that contact point of the two particles.

1.2. Objective

Based on his extensive review of the silica chemistry a comprehensive mechanism for the silica polymerization in aqueous solution has been already postulated by Iler[22]in 1979. Investigations at that time focused mainly on the determination of the monomer consumption as a function of time in order to evaluate rate constants and the reaction order under different reaction conditions. Determination of the particle size has been performed only indirectly via the size dependent solubility of amorphous silica.

All studies on silica polymerization in the last decades provided a considerable amount of experimental indications for some essential features of the mechanism of silica particle formation. However, direct evidence of particle growth is still poor as the work rarely provided direct data on the nature of the growing particles and on how they grow. Only a few recent studies mainly those by Tobler[46,48] made use of modern scattering techniques, in order to follow simultaneously the growth of the particles and the depletion of the monomeric silica. Although the 3-step mechanism postulated by Iler[22] could be confirmed, some open questions remain. What is the origin of the lag-time? How is the lag-time affected by a change in the pH value or the presence of counter ions? What is the nature of the particles growing after nucleation? Do those particles grow according to a monomer addition step, denoted as chain growth in polymer science or do they grow according to a particle-particle aggregation denoted as step-growth process in polymer science? Once, it does occur, under which conditions does a particle-particle aggregation take place? What is the fractal dimension of those late stage polymers? Under which conditions does Ostwald-ripening occur?

The present study tries to answer some of these questions by applying the in-situ technique of time-resolved combined static and dynamic light scattering and the molybdenum blue method in order to get direct access to the particle formation in terms of the weight-averaged molar mass and the particle size as well as to the monomer consumption. For this purpose the silica polymerization is studied in the concentration regime of 350-3000 ppm SiO_2 in aqueous solution. At the onset of our study the process of particle formation is followed at pH 7 in pure water, defining the reference system. The results of these experiments are summarized in Chapter 3.1.1. In Chapter 3.1.2 the behaviour

observed at neutral pH is compared with results obtained at pH 8. The influence of the presence of metal cations as counter ions on the silica particle formation is discussed in Chapter 3.2. For this purpose we investigate the effect of a mixture of calcium chloride and magnesium chloride at a ratio of 4 : 1 with a total concentration of metal ions of 5 mM in water as solvent. This mixture is used to simulate the conditions of hard water, often present in the water-treatment industry. Furthermore the effect of sodium chloride as an inert salt in addition to the amount of NaCl formed during the neutralization is investigated by using an aqueous solution of 10 mM NaCl as medium and compared to the results collected in pure water and in the presence of Ca^{2+}+Mg^{2+}-ions.

In Chapter 3.4 the experimental data obtained via light scattering and molybdenum blue method is interpreted in more detail concerning the mechanistic features of the silica particle formation. Experimental data describing the aggregation of silica particles to larger clusters are discussed in more detail regarding a possible diffusion-controlled or reaction-controlled particle-particle aggregation mechanism (see Chapter 3.4). In Chapters 3.5.1 - 3.5.3 two different kinetic models are applied, describing a particle growth via monomer-addition on the experimental data obtained by light scattering and the molybdenum blue method. The kinetic studies are expected to clarify important characteristic features of the growth process.

Chapter 3.7 summarizes experiments which have been performed in order to verify the influence of three different model polymers on the silica particle formation. The following polymers have been chosen: (i) poly(ethylene oxide) as neutral polymer, (ii) poly(acrylic acid) as anionic polyelectrolyte and (iii) poly(acrylic acid)-2-acrylamido-2-methylpropane sulfonic acid (AA-AMPS) as anionic and highly acidic polyelectrolyte. Two silica contents are investigated 500 ppm and 750 ppm at pH 7 in pure water as well as in the presence of a mixture of Ca^{2+}+Mg^{2+}. The experimental data are interpreted regarding a possible application as antiscalants in desalination plants in order to inhibit silica fouling and silica scaling on RO membranes.

1.3. Theory of Particle Growth

1.3.1. Classical Nucleation Theory

The origin of new phases is always a nucleation process, thus it is a phenomenon occurring in all fields, in nature as well as in technology. Crystallization, evaporation, condensation and deposition of thin films are prominent examples where nucleation plays an important role. Crystallization and particularly its control in terms of number, size, perfection, polymorphism and other characteristics of crystallites, has an outstanding relevance in chemical industry and also in a lot of physiological and pathological phenomena.[51] Nucleation is defined as the process by which atoms or molecules of a reactant phase rearrange into a cluster of the new phase, which is large enough to grow irreversibly to a macroscopically large size. This cluster is named as nucleus or critical nucleus.[52] J. W. Gibbs developed the thermodynamics of the nucleation in the seventies of the nineteenth century.[53,53] Volmer and Weber[54] published 1926 the first paper on kinetics of nucleation.

Together with the paper of Becker and Döring[55] they provided the basis for the classical nucleation theory (CNT). Excellent summaries of the theoretical background of the CNT can be found in ref. 50, 51, 56.

Nucleation initiates a first-order phase transition and its driving force is the supersaturation. Considering the case that the solution phase consists of dissolved molecules and the solid phase is the condensate of these dissolved molecules the chemical potential of the solute is given by

$$\mu_{sol}(a) = \mu_{eq} + kTln\frac{a}{a_{eq}} \tag{1.2}$$

here it is μ_{sol} the Gibbs energy of a solute molecule in solution, a the actual activity of the solute and a_{eq} the equilibrium activity, where the solute and the condensate state are at equilibrium. Since the chemical potential of the condensate μ_{crys} in the bulk is independent on the activity a it is equal to the chemical potential of solute at $a = a_{eq}$ where solute is in equilibrium with its solid phase.

$$\mu_{crys} = \mu_{sol}(a_{eq}) \tag{1.3}$$

In a supersaturated solution the formation of a n-sized cluster is connected with a loss of free energy of $-n\Delta\mu$ as the chemical potential of the solute μ_{sol} is higher than the chemical potential of the crystal μ_{crys} in the bulk phase. It is $\Delta\mu = \mu_{sol} - \mu_{crys}$ with μ_{sol} and μ_{crys} expressed as Gibbs free energy per atom or molecule. The loss in free energy G per molecule by passing from the energy state in the solution phase to the state in the solid phase corresponds to the difference of the chemical potentials. As a result $\Delta\mu$ can be expressed as

$$\Delta\mu(a) = kTln\frac{a}{a_{eq}} \cong kTln\frac{c}{c_{eq}} \tag{1.4}$$

Under the assumption of very dilute solutions the activities a and a_{eq} can be replaced by the concentration of the solute in the solvent c and the equilibrium concentration c_{eq}, resulting in the right side of Equation 1.4.

Beside the loss of energy from the supersaturated state of the solution, the system has to overcome an energy barrier by creating the solid phase. One way to describe the change from the density of the supersaturated phase to the density of the solid phase is the cluster approach. A small part of the new phase is described as a cluster consisting of n molecules or atoms. The cluster is considered as separated from the supersaturated phase by a phase boundary. This makes it possible to distinguish between molecules which belong to the supersaturated phase and molecules which belong to the solid phase. An illustration of such a cluster separated by a phase boundary is given in Figure 1.6a. Considering an isobaric and isothermal system, the overall work for the formation of an n-sized cluster is given by the change in the Gibbs free energy ΔG.

$$\Delta G(n) = -n\Delta\mu + G_{ex}(n) \qquad \text{with } n = 1, 2, 3... \tag{1.5}$$

The cluster excess free energy $G_{ex}(n)$ is a function of the cluster size n. With the assumption that all clusters, independent on n have the same shape, the cluster excess free energy

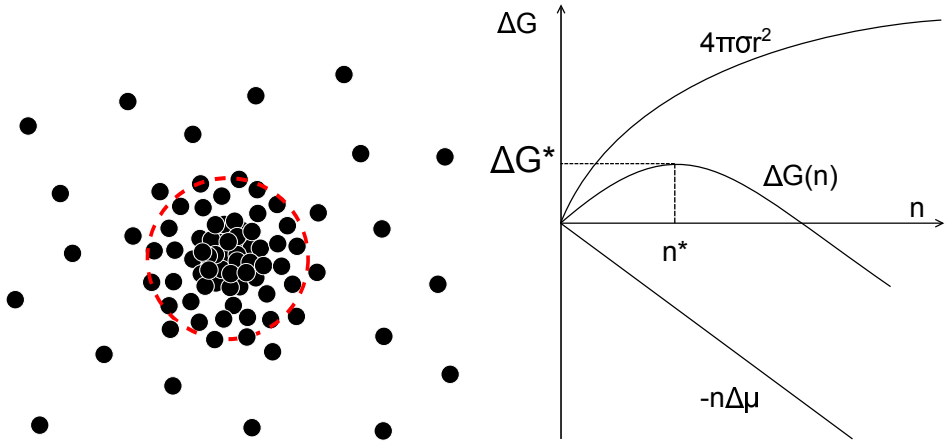

(a) Nanoscopical formation of the solid phase, the red dashed line denotes the phase boundary of the cluster. It defines which monomer molecules belong to the cluster and which molecules belong to the solution phase.

(b) Trend of ΔG as a function of the number n molecules in a cluster. $\Delta\mu$ is the supersaturation, σ the free surface energy and the star denotes the state of the critical cluster.

Figure 1.6.

is proportional to the surface area A of the smallest cluster ($n = 1$), the surface tension σ and the scaling factor $n^{2/3}$.

$$G_{ex}(n) = An^{2/3}\sigma \quad \text{for spherical clusters} \quad A = 4\pi a^2 \tag{1.6}$$

Considering spherical clusters the surface area of the smallest cluster is given by $4\pi a^2$, with a the effective radius of the monomer unit. The radius of the n-sized cluster can then given by $an^{1/3}$. These assumptions lead to the following expression for the Gibbs free energy.

$$\Delta G(n) = -n\Delta\mu + 4\pi a^2 n^{2/3}\sigma \tag{1.7}$$

Figure 1.6b illustrates the thermodynamics of the formation of a condensed cluster. The size of the critical cluster $n = n^*$ is defined by the maximum of ΔG, where the two contributions belonging to the supersaturation and to the formation of the phase boundary are equal. Based on spherical clusters the critical nucleus size and the Gibbs free energy of this nucleus is given by

$$n^* = \left(\frac{8\pi a^2\sigma}{3\Delta\mu}\right)^3 \qquad \Delta G^* = n^*\frac{5}{2}\Delta\mu. \tag{1.8}$$

ΔG^* is the limiting energy barrier which must be overcome to generate a cluster from solute monomers. Cluster with different sizes will occur in the solution via fluctuations. If a cluster greater than n^* will appear, it will grow spontaneously as this is connected with

a decrease in free energy. However, clusters with sizes smaller than n^*, often denoted as embryos, may redissolve as an addition of monomers in this case is connected with an increase in free energy. A critical cluster of size n^* has the same probability for growing and dissolving. The formation of the solid phase is based on these critical clusters, they represent the nuclei. According to Equation 1.8 the greater the degree of supersaturation becomes, the smaller the critical cluster size n^* gets. That means that during formation of a solid phase the critical cluster size will increase as the supersaturation is decreasing due to an uptake of monomers by the nucleation process as well as by the growth process. The rate of nucleation is decreasing with decreasing supersaturation and the growth process will play an increasingly dominating role until the monomers are consumed or an equilibrium concentration of the monomers is reached. Based on the assumptions of the classical nucleation theory the rate of nucleation can be expressed in analogy to the Arrhenius-approach via the actual concentration of critical clusters $c(t)$ in untis of m^{-3}. J describes the number of critical nuclei being generated per unit solution volume and per unit time.

$$J = A \cdot exp\left(\frac{-\Delta G(n^*, c(t))}{kT}\right) \tag{1.9}$$

The pre-exponential factor A [$m^{-3}s^{-1}$] is defined as

$$A = Zf^*c(t) \tag{1.10}$$

with the Zeldovich factor Z describing the probability for a critical cluster to grow to a stable cluster. Typical values lie in the range of $0.01 < Z < 1$. The rate of attachment of monomers to the nucleus is given by f^* lying in the range of $1\text{-}10^{12}$ s^{-1} and $c(t)$ the actual monomer concentration in [m^{-3}].

The Equations 1.9 and 1.10 include the concentration of critical nuclei n^* expressed as thermal distribution defined by the Gibbs free energy ΔG and the actual monomer concentration $c(t)$ in [m^{-3}].[56] Based on this the concentration of embryos with $n \leq n^*$ is given by

$$P(n,t) = c(t)exp\left[\frac{-\Delta G(n, c(t))}{kT}\right] \tag{1.11}$$

A second approximation for the rate of nucleation is then given by the concentration of the critical nuclei the concentration of monomers and the rate constant of nucleation.

$$J = k_n \cdot c(t)P(n^*, t) \tag{1.12}$$

with k_n in [m^3s^{-1}] describing via the Smoluchowski[57,58] approach the rate of attachment of diffusing monomers to diffusing spherical particles.

$$k_n = 4\pi(a + an^{1/3})(D + Dn^{-1/3}) \approx 4\pi an^{1/3}D \tag{1.13}$$

D is the diffusion coefficient of monomers and $an^{1/3}$ is the radius of an n-sized cluster.

2. Methods and Instruments

2.1. Chemicals

Sodium metasilicate $Na_2H_2SiO_4 \cdot 8H_2O$ (assay, ≥ 98%), calcium chloride hexahydrate $CaCl_2 \cdot 6H_2O$ (assay, ≥ 98%), magnesium chloride hexahydrate $MgCl_2 \cdot 6H_2O$ (assay, ≥ 99%) and sodium chloride (assay, ≥ 99%) was purchased from *Sigma Aldrich*. Millipore water (conductivity 0.055 $\mu S/m$) was used for all samples as a solvent. pH adjustment was carried out by using 2 M HCl. For the determination of monomeric silica ammonium molybdate tetrahydrate $(NH_4)_6Mo_7O_{24} \cdot 4H_2O$ (assay, ≥ 99%) and 1-amino-2-naphthol-4-sulfonic-acid $C_{10}H_9NO_4S$ (assay, ≥ 95%) were purchased from *Fluka*. Dry sodium pyrosulfit $Na_2S_2O_5$ (assay, ≥ 98%) from *Riedel de Haen AG*, sodium sulfit Na_2SO_3 from *BASF SE* and oxalic acid $C_2H_2O_4 \cdot H_2O$ from Sigma Aldrich was used. Poly(ethylene)glycol with a weight-averaged molar mass M_w = 6550 g/mol, purchased by *Polymer Standard Services Mainz*, was used as a representative neutral model polymer. Poly(acrylic acid) (PA) and acrylic acid-2-acrylamido-2-methylpropanesulfonic acid (AA-AMPS-copolymer) were provided by *BASF SE*.

2.2. Light Scattering

Light scattering is based on the interaction of an electromagnetic wave with the electrons of the atomic shell. Thereby, a dipole moment is induced which in turn emits a secondary electromagnetic wave (secondary wave) with the same wavelength and frequency as the impinging wave. Scattered waves are influenced by the mass, size and form of the particles and the interactions among the particles in the investigated sample. Detailed information about the theory of light scattering and the application on polymeric and colloidal systems can be found in the textbooks from Chu[59], Kratochvil[60] and Huglin[61]. Only the most important equations shall be introduced in Chapter 2.2.1 and 2.2.2.

2.2.1. Static Light Scattering

A static light scattering experiment measures the averaged scattering intensity as a function of the scattering angle θ. This scattering intensity of a solute in solution is expressed as Rayleigh ratio ΔR_θ

$$\Delta R_\theta = R_{\theta,std} \frac{r_{\theta,sol} - r_{\theta,solv}}{r_{\theta,std}}, \tag{2.1}$$

with $R_{\theta,std}$ the absolute scattering intensity of the tabulated standard toluene in units of reciprocal length, $r_{\theta,std}$ the measured scattering intensity of the standard toluene, $r_{\theta,sol}$ the measured scattering intensity of the solution and $r_{\theta,solv}$ the scattering intensity of the solvent. Intensities are usually represented as a function of the absolute value of the scattering vector $\vec{q}$ in arbitrary units, which is defined as the difference between the wave vector of the primary beam $\vec{k_i}$ and the wave vector of the scattered beam $\vec{k_s}$:

$$|\vec{k_i} - \vec{k_s}| = |\vec{q}| = \frac{4\pi n_{solv}}{\lambda_0} \sin\frac{\theta}{2}, \tag{2.2}$$

with n_{solv} the refractive index of the solvent, λ_0 the wavelength of the primary beam in vacuum and θ the scattering angle.

Two routines have been used during this work in order to evaluate the particle size and the particle mass from angular dependent scattering intensities, the Zimm[62] method and the Guinier[63] approximation. From a Zimm-plot the molar mass M_w, the radius of gyration R_g and the second virial coefficient A_2 from dilute solutions of scattering particles is determined as follows:

$$\frac{Kc}{\Delta R_\theta} = \frac{1}{M_w} + \frac{R_g^2}{3M_w}q^2 + 2A_2c \tag{2.3}$$

It is c the concentration of the dissolved particles (solute) in g/l and K the contrast factor which combines the parameters Avogadro's number N_A, laser wavelength λ_0, refractive index of the standard toluene n_{tol} and the refractive index increment $\frac{\partial n}{\partial c}$ of the solute in the solvent via

$$K = \frac{4\pi^2}{N_A\lambda_0^4}(n_{tol}\cdot\frac{\partial n}{\partial c})^2. \tag{2.4}$$

The refractive index of the standard toluene is used, as the Hermans and Levinson[64] correction of the scattering volume for cylindrical glass cuvettes is applied. The Zimm method for the evaluation of the scattering intensities enables the extrapolation to infinite dilution ($c \to 0$) and to $q^2 \to 0$ in order to determine M_w and R_g. All light scattering experiments shown in this work investigate particle growth processes and are performed in a time-resolved manner. In the beginning of the growth process the scattering intensity is comparable to the scattering intensity of the solution, as the initial silica species is a weak scatterer. With proceeding growth the mass fraction, incorporated into growing particles, which causes an increasing scattering intensity, is increasing whereas the mass fraction of the initial silica species is decreasing. An extrapolation of scattering intensities recorded in a time-resolved experiment to infinite dilution and with it the determination of the second virial coefficient is not possible. An extrapolation to $q^2 \to 0$ is meaningful as long as the solution is very dilute. For the investigated silica solution this condition is satisfied because the concentrations lie between 0.3 g/l and 3 g/l.

If the scattering curve exhibits a distinct bending a quadratic Guinier approximation is applied yielding the weight-averaged molar mass and the radius of gyration

according to eq 2.5.

$$\ln \frac{Kc}{\Delta R_\theta} = \ln \frac{1}{M_w} - \frac{R_g^2}{3} q^2 \tag{2.5}$$

where the virial coefficient was neglected.

As the intensities scattered by a particle are influenced by intraparticular interferences, the scattering intensities provide information about the particle structure. The angular dependent scattering intensity can be described by the formfactor $P(q)$, which is the ratio of the Rayleigh ratio at θ (ΔR_θ) and at $\theta = 0$ ($\Delta R_{\theta \to 0}$).[60]

$$P(q) = \frac{\Delta R_\theta}{\Delta R_{\theta \to 0}} \tag{2.6}$$

$P(q)$ adopts a value of one for particles small in comparison to the applied wavelength. For static light scattering a particle size of at least 100 nm is necessary to discriminate significantly among different particle shapes.

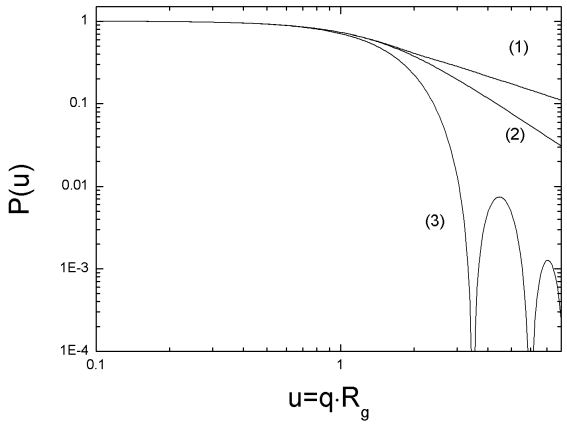

Figure 2.1.: Formfactors as $P(u = qR_g)$ for (1) a stiff rod[65], (2) a Gaussian coil[66] and (3) a compact sphere[67].

2.2.2. Dynamic Light Scattering

Dynamic light scattering probes the temporal intensity fluctuations. The detector at a certain scattering angle records a superposition of the electric fields emitted from all scatterers in the illuminated volume. As the scatterers are translating, rotating and vibrating due to the Brownian motion the detected intensity will fluctuate in time.

As a mathematical description of these intensity fluctuations a time-dependent autocorrelation-function $g_I(\tau)$ is introduced. For that purpose the measurement time T is divided into time intervals Δt. The scattering intensity measured at any time t is multiplied with the intensity measured after a certain lag-time $\tau = n \cdot \Delta t$. This procedure is repeated along T including a statistically sufficient number at Δt and averaged. The same procedure

is applied for different values of n. The variable n adopts natural numbers. The correlation of the intensities will decrease with increasing lag-time.

$$\langle I(t) \cdot I(t+\tau) \rangle = \frac{1}{T} \int_0^T I(t) \cdot I(t+\tau) dt \tag{2.7}$$

Division by $\langle I(t) \rangle^2$, which is the limit value for large lag-times τ, gives the normalized intensity-time-autocorrelation function $g_I(\tau)$.

$$g_I(\tau) = \frac{\langle I(t) \cdot I(t+\tau) \rangle}{\langle I(t) \rangle^2} \tag{2.8}$$

It has to be stressed that the averaged value of the scattering intensity $\langle I(t) \rangle$ corresponds to ΔR_θ in static light scattering. The decrease of $g_I(\tau)$ depends on the particle velocities. In more detail, the faster the particles move, the faster the correlation will decrease. The time dependent correlation function is given as the sum of all intensity products divided by the total number of all products. As the total measurement time T is very large in comparison to the time interval Δt the sum can be described by the integral.

Evaluation of dynamic light scattering requires the knowledge of the field-time-autocorrelation function $g_E(\tau)$, which can be derived from the intensity-time-autocorrelation function via the Siegert-relation[68,69]:

$$g_I(\tau) = 1 + \beta \cdot [g_E(\tau)]^2 \tag{2.9}$$

with β a spatial coherence factor which depends on the number of coherence areas viewed. Usually this quantity is determined by a fit to the experimental data. The field-time-autocorrelation function $g_E(\tau)$ is given by

$$g_E(\tau) = \frac{\langle E(0) E(q,\tau) \rangle}{\langle E(\tau)^2 \rangle} \tag{2.10}$$

where E denotes the strength at the electric field of the scattered waves. In case of monodispers scatterers the field-time-autocorrelation function can be described by a single exponential decay according to

$$g_E(\tau) = e^{-\Gamma \tau} \tag{2.11}$$

where the time constant Γ describes the inverse time required by the scatterer to cover a mean squared displacement of q^{-2}. The decay constant is connected to the translational diffusion coefficient via

$$\Gamma = D q^2. \tag{2.12}$$

Systems of polydispers particles yield a superposition of exponential decays and can thus be described by a sum of exponential functions

$$g_E(\tau) = \sum_{i=1}^{n} \gamma_i e^{-\Gamma_i \tau} \tag{2.13}$$

where Γ_i is the time constant and γ_i the weighting factor of species i within the respective total ensemble. Evaluation of the correlation functions has been carried out with the cumulant method by Koppel[70]. The logarithm of the field-time-autocorrelation function is rewritten as a series

$$ln[g_E(\tau)] = K_0 - K_1\tau + \frac{1}{2!}K_2\tau^2 - \frac{1}{3!}K_3\tau^3 + ... \tag{2.14}$$

where K_0 is a constant describing the signal-to-noise-ratio and the coefficient K_1 is the z-averaged time constant $\langle\Gamma\rangle$, which correlates with the z-averaged diffusion coefficient according to

$$K_1 = \langle\Gamma\rangle = \langle D_z \cdot q^2\rangle. \tag{2.15}$$

The coefficient K_2 expresses the variance of the time constant being a measure for the polydispersity.

$$K_2 = \langle(\Gamma - \langle\Gamma\rangle)^2\rangle \tag{2.16}$$

The diffusion coefficient D_z obtained in this way is still an apparent value and has to be extrapolated to zero concentration $c \to 0$ and zero angle $q^2 \to 0$ according to

$$D_z = D_0(1 + q^2R_g^2C + k_dc) \tag{2.17}$$

where C is a dimensionless parameter which depends on the shape of the particles and k_D is a parameter accounting for the concentration dependence of D_z. From the extrapolated diffusion coefficient the hydrodynamic radius can be obtained by the Stokes-Einstein equation

$$R_h = \frac{kT}{6\pi\eta}\frac{1}{D_0} \tag{2.18}$$

with k the Boltzmann constant, T the temperature and η the viscosity of the solvent. A concentration dependence has been neglected in all experiments for the same reasons as in case of Equations 2.3 and 2.5.

$$\rho = \frac{R_g}{R_h} \tag{2.19}$$

The ratio of the radius of gyration and the hydrodynamic radius provides also structure information in addition to that from the formfactor based on static light scattering. This shape-sensitive factor is named ρ-factor and adopts smaller values as the particle becomes more compact. For monodisperse linear polymer chains under θ-conditions denoted as unperturbed chains, a value of 1.504 is predicted by theory,[71,72] which turned out to be 17.5% larger than values revealed by experiment.[73] The fractal dimensions of such unperturbed linear chains is 2. In the case of compact spheres ρ decreases drastically to 0.77.[71] For rod-like structures a value of $\rho \geq 2.0$ is expected.[74,75] Therefore, a distinction between spheres, rods, and fractal structures similar to unperturbed polymer coils by means of the ρ-parameter is possible.

2.2.3. Scaling laws

A correlation of the radius of gyration or the hydrodynamic radius with the weight-averaged molar mass provides important information about the shape of the growing particles. For self-similiar structures the correlation yields power laws with a shape-sensitive exponent which in case of self-similar structures exhibits the same value for R_g and R_h.

$$R_g \propto R_h \propto {M_w}^{\alpha} \tag{2.20}$$

In case of compact, spherical particles α assumes a value of $1/3$ and for polymer coils under ideal conditions the power law goes with $\alpha = 1/2$.

If the growth of the particles is followed by light scattering two limiting cases have to be distinguished. In case of a monomer-addition process the weight-averaged molar mass obtained via light scattering refers to all solute species comprising non-consumed monomers and particles, which leads to an exponent smaller by a factor of 1/2 than the value of the exponent of Equation 2.20 given by the respective topology.[76,77] Knowledge of the time-dependent monomer concentration can be used to re-evaluate the scattering intensities with the mass concentration of the growing particles only, yielding a mass-size correlation going with the original topology based exponent. In case of a particle-particle agglomeration where any particle can agglomerate with any other, the exponent satisfies the topology based values.

2.3. Determination of the Refractive Index Increment

A differential refractometer provided by *SLS-Systemtechnik* was used for the dn/dc-measurements. The instrument is based on deflection via an oblique partition wall. A He-Ne laser with a wavelength of 635 nm serves as a light source. The laser beam is guided through a two-chamber cuvette, which contains in one chamber the solvent and in the second chamber the solution. These two chambers are diagonally divided at 45° by a thin glass plate. Advantage of this optical design in comparison to other types of refractometers is that only the difference of the refractive indices influences the deflection. The detection units of other refractometers have to cover a broader angle regime, as already the refractive index of the solvent leads to a basic deflection. As a consequence the detection unit of the common refractometers achieve a lower resolution.

The measurement requires a precise temperature control of the cuvette, as small differences in the temperature between the sample solution and the reference solution have a high impact on the refractive indices. Beside the measurements of the different concentrated samples two reference measurements are possible, but not mandatory for the determination of the refractive index increment. The first reference measurement denoted as zero-measurement is a measurement of the free beam path, without cuvette and determines an absolute reference point for the linear Δn. As it is highly reproducible, it can be used to check the measured data for a possible signal shift. The second reference measurement denoted as ref-measurement is a measurement for which the cuvette is inserted into the beam path, with both chambers filled with solvent. This measurement is

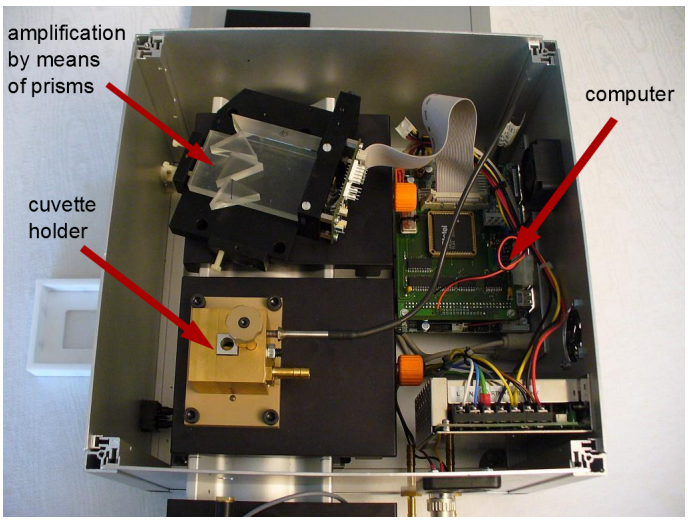

Figure 2.2.: View inside of the differential refractometer of *SLS-Systemtechnik*.[78]

needed if the offset of the applied set-up is required like for instance if the concentration of a solution should be determined based on a known dn/dc and if different curves should be compared quantitatively. Furthermore it is needed for both the regular and the inverse set-up if rotation of the cuvette by 180° (inverse set-up) is used for the generation of additional data points, as the offset of the cuvette can be different for the two different cuvette orientations. In order to align the positive and the negative deflections both offset-values are used.

Figure 2.2 shows a view on the interior of the differential refractometer, which is composed of three main units, the cuvette holder bottom left, the detection unit top left and the computer on the right.

The deflected laser beam is at first amplified by means of three prisms, which achieve an amplification by a factor of 50-70. The usage of such prisms enable a very compact architecture of the instrument. Then the beam is incident on a cuboid beam splitter which generates partial beams and which further amplifies the angular deflection. The partial beams are reproduced as peaks on the CCD-sensor. The distance between two of the peaks is depends only on the incident angle on the beam splitter and the constant set-up and hence is directly connected to the angle of deflection. Therefore the measurement is an absolute method. The distance between the peaks with position P_1, P_2 and P_3, is calculated as an average of all three possible distances, according to

$$\Delta P = \frac{1}{3} \cdot \left((P_2 - P_1) + (P_3 - P_2) + (\frac{P_3 - P_1}{2}) \right). \tag{2.21}$$

In this way possible fuzziness of a single peak can be minimized or compensated. The resolution limit of the instrument amounts to 0.0001°. Figure 2.3 represents a schematic overview of the beam path through the three prisms and the cuboid beam splitter.

The total displacement of the laser beam by passing the cuvette for a given solution is described by

$$\Delta d = d_1 - d_{01} \tag{2.22}$$

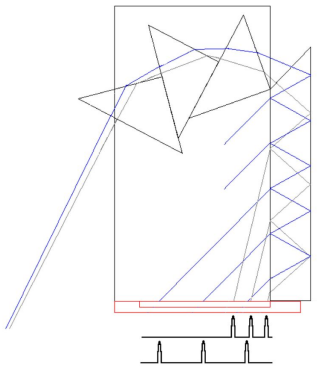

Figure 2.3.: Schematic overview of the beam path in the detection unit. The blue beam is deflected at n_0 and corresponds to d_{01} (ref-measurement in Equation 2.22) and the grey beam is deflected at n and corresponds to d_1 (solution measurement in Equation 2.22). The deflection between the blue and the grey beam amounts to ~1.5° and gives Δd. The beam passes the three prisms and impinges on the cuboid beam splitter on the right hand site. The CCD-Sensor is positioned on the bottom and is schematically indicated as red lines. The three peaks resulting on the CCD-sensor for the blue and grey beam are drawn.[78]

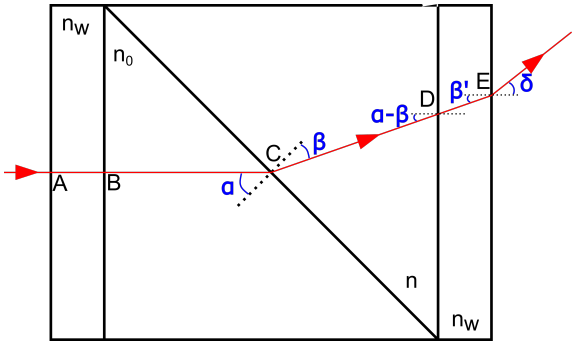

Figure 2.4.: Path of the laser beam through the two-chamber cuvette of the differential refractometer. From left to right the beam at first enters the glass window at A, the chamber of the solvent at B, the thin glass partition at C at an angle of α, then it enters the chamber of the solution with and angle of β, enters the second glass wall at D and finally enters air at E with an angle of δ.

with d_{01} describing the deflection of the ref-measurement and d_1 of the solution measurement. Δd is directly proportional to the difference in the refractive index:

$$\Delta n = k\Delta d \tag{2.23}$$

where k is a coefficient which can be evaluated from the geometry of the cuvette and the instrument.

If the rotation of the cuvette is used in order to generate additional data points, the total displacement of the laser beam can be expressed as

$$\Delta d = (d_1 - d_2) - (d_{01} - d_{02}) \tag{2.24}$$

where the index 1 describes the measured deflection with the regular set-up and the index 2 the deflection measured with the inverse set-up. The prefix 0 in the index denotes the corresponding ref-measurement.

Figure 2.4 shows a schematic overview of the two-chamber cuvette together with the light path. The beam passes the cuvette window with a refractive index of n_w and the solvent chamber (n_0), it is incident at angle α on the thin partition and is deflected on passing into the solution chamber (n). After passing the second glass window at D it enters air at E with a final angle of deflection δ. The refractions at C, D and E can be described with Snell's law

$$\begin{aligned} n_0 \cdot sin(\alpha) &= n \cdot sin(\beta) \\ n \cdot sin(\alpha - \beta) &= n_w \cdot sin(\beta') = sin(\delta) \end{aligned} \tag{2.25}$$

As the angles $\alpha - \beta$ and δ are very small one can use the approximation:

$$n(\alpha - \beta) = \delta. \tag{2.26}$$

From this it follows that $\beta = (\alpha - \delta)/n$ and we get an expression according to Snell's law depending on the refractive indices of the solvent n_0 and the solution n.

$$n_0 \cdot sin(\alpha) = n \cdot sin(\frac{(\alpha - \delta)}{n}) \tag{2.27}$$

Equation 2.27 leads to

$$n - n_0 = \delta \cdot cot(\alpha) + \frac{\delta^2}{2n} \tag{2.28}$$

The principle of the two-chamber cuvette allows to record two data points per solution concentration. The cuvette can be rotated by an angle of 180°, which leads to a deflection in the opposite direction and with it to negative values for the difference in the refractive indices. In analogy to Equation 2.28 $n - n_0$ for the inverse set-up can be expressed as

$$n - n_0 = \delta' \cdot cot(\alpha) - \frac{\delta'^2}{2n_0}. \tag{2.29}$$

An addition of Equations 2.28 and 2.29 and neglect of the sum of the quadratic term leads to

$$n - n_0 = \frac{1}{2}(\delta + \delta') \cdot cot(\alpha). \tag{2.30}$$

From the geometry of the cuvette and the instrument an expression for $\delta + \delta'$

$$(\delta + \delta') = (d_1 - d_2) \cdot \frac{1}{m_0(a + \frac{b}{2n_0} + \frac{t}{n_w})} \tag{2.31}$$

can be found. The value m_0 accounts for an optical amplification, this is depending on the instrument design. In Equation 2.31 a is the distance from the slit to the first glass wall of the cuvette, b the inner thickness of the cuvette, n_0 the refractive index of the solvent, t the thickness of the glass wall of the cuvette and n_w the refractive index of the glass wall. Inserting Equation 2.31 into Equation 2.30 gives[79]:

$$n - n_0 = (d_1 - d_2) \cdot \frac{cot(\alpha)}{2m_0(a + \frac{b}{2n_0} + \frac{t}{n_w})} \tag{2.32}$$

Comparison with Equation 2.22 gives for the coefficient k

$$k = \frac{cot(\alpha)}{2m_0(a + \frac{b}{2n_0} + \frac{t}{n_w})}. \tag{2.33}$$

2.3.1. Refractive index increment of $Na_2H_2SiO_4 \cdot 8H_2O$ in water

The dn/dc for a solution of $Na_2H_2SiO_3 \cdot 8H_2O$ at 37° has been determined to 0.454 cm^3/g. This value is based on concentrations of SiO_2 as solid and was translated from concentrations of $Na_2H_2SiO_4 \cdot 8H_2O$ as solid via the factor M ($Na_2H_2SiO_4 \cdot 8H_2O$) / M (SiO_2).

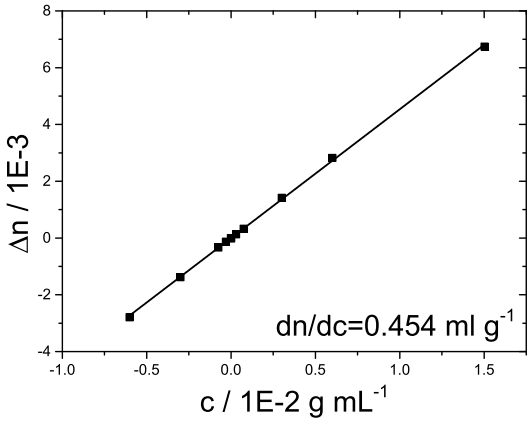

Figure 2.5.: Refraction of the silica solutions as a function of the concentration. The silica concentration c refers to SiO_2 = 60.1 g/mol.

2.3.2. Refractive index increment of poly(acrylic acid) in water

The dn/dc for a solution of poly(acrylic acid) in distilled water at 37° has been determined to 0.158 cm^3/g. Figure 2.5 shows the measured differences in the refractive indices Δn as a function of the mass concentration of silica.

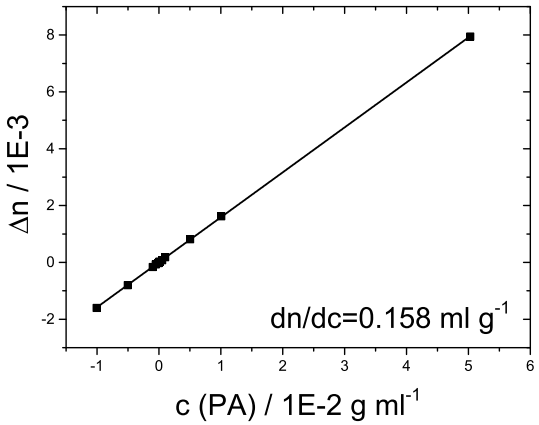

Figure 2.6.: Refraction of the PA solutions as a function of the mass concentration of poly(acrylic acid) c(PA).

2.4. Light Scattering Instruments

2.4.1. Home Build TR-SLS Instrument

Time-resolved static light scattering (TR-SLS) was performed with a home build instrument equipped with 38 light guides at 2 times 19 angles embedded into the goniometer. A schematic overview of the instrument set-up is shown in Figure 2.7. A Helium-Neon-Laser with a wavelength of 632.8 nm and a power of 35 mW serves as a light source. After passing the first shutter the beam is guided by two silver mirrors to two apertures and a lens. The lens, with a transmission of > 95% and a focal distance of f = 300 mm focuses the beam into the centre of the goniometer, where the scattering cell is located. In order to avoid significant scattering effects from the interface between glass and air, the scattering cell is positioned in a temperature controlled bath with toluene. The signal recorded by the 38 light guides is converted into an intensity dependent electric current by means of photo-diodes (Siemens BPW 32). A pre-amplifier changes the electric current into a potential. An additional amplification together with an improvement of the signal to noise ratio is achieved via a lock-in-amplifier.

The lock-in amplifier uses the phase-sensitive detection to single out a component of a signal at a specific reference frequency and phase fixed by the reference. Noise signals at frequencies other than the reference frequency are rejected and do not affect the measurement. The lock-in amplifier works like a very narrow-edged bandpassfilter and requires as an input the measurement signal and a reference signal phase-locked to

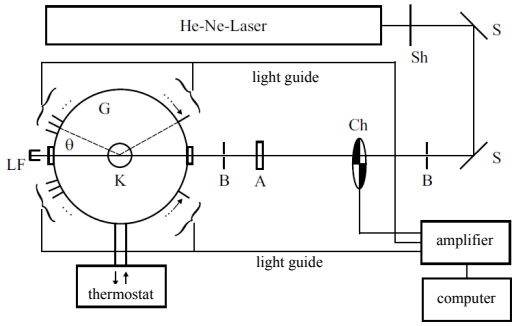

Figure 2.7.: Set-up of the home built TR-SLS instrument. The abbreviation indicates the following components: Shutter (Sh), silver mirror (S), aperture (B), chopper (Ch), lens (A), cuvette (K), goniometer (G), beam stop (LF) and the scattering angle (θ).[80]

Table 2.1.: Amplification steps and the corresponding amplification factor of the home build TR-SLS instrument.

amplification stage	factor
1	1
2	5
3	10
4	50
5	100
6	500
7	1000

the frequency of the measurement signal. The reference signal is provided by chopping the signal, which is done with a mechanical chopper rotating with a frequency of 481 Hz. Modulation of the measurement signal U_{sig} (Figure 2.8a) is performed by multiplying it with the reference signal U_{ref} (Figure 2.8b) in a mixer leading to signal c in Figure 2.8. Integration of the signal over several periods of the modulation frequency by a low pass filter gives as output an AC voltage proportional to the measurement signal (Figure 2.8d). With this process even interfering signals, which have the same frequency but which of course are not in phase with the measurement signal can be filtered out.

The lock-in technique enables the amplification of the signal in seven different stages, up to an amplification with a factor of 1000. This gives an easy opportunity to adjust the scattering signal individually for every sample. Table 2.1 gives an overview on the seven amplification stages.

The scattering signal is passed to the computer as $r_{\theta,sol}$, $r_{\theta,solv}$ and $r_{\theta,std}$. Each single angular dependent measurement requires at least 2 ms. The time-resolution applied for the system analysed in the present work is an average over 1000 single q-dependent measurements. This corresponds to an actual measurement time of 2 s but requires ~ 6 s

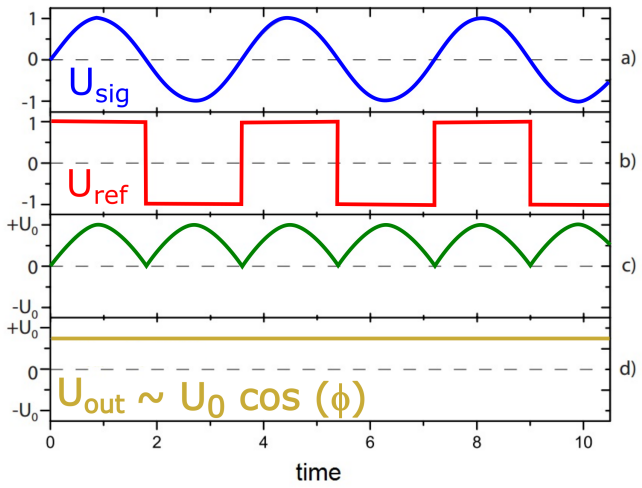

Figure 2.8.: Signals at the lock-in amplifier: a) Measurement signal U_{sig}, b) the reference signal U_{ref}, c) the product of measurement and reference signal, d) the output signal U_{out} which corresponds to an integration of the curve in c).

in addition for data processing. For stable samples and also for the measurements of the solvent it is suitable to average up to 4000 single measurements to improve statistics. As the time for data processing increases with increasing number of single measurements, the total recording time for 4000 single measurements is at least 30 s.

Further details about the instrument and the data processing are given in the publication of Becker and Schmidt[81] and in the PhD-thesis of T. Witte[80]. The solvent measurements has been usually performed with an amplifying stage of 7 recording 4000 measurements in 30 s. The parameters of the measurement of the silica solutions have been varied individually for every sample, depending on the silica concentration and the velocity of the particle growth.

2.4.2. ALV 5000E Compact Goniometer System (1-angle detection)

Combined measurements of static (SLS) and dynamic (DLS) light scattering are performed with the 5000E Compact Goniometer of the *ALV-Laservertriebsgesellschaft* (Langen). Figure 2.9 shows a scheme of the instrument. A neodymium-yttrium-aluminium-garnet laser with a wavelength of 532 nm and a power of 100 mW is used as a light source. The laser beam is deflected by two mirrors and guided to the attenuator. This enables variable attenuation of the primary beam, if the scattering intensity of the sample is too high for the detector. A lens is focusing the beam into the goniometer to the scattering cell. The scattering cell is temperature controlled by an index matching toluene bath. The detector is placed on an arm, which can address every angle in between 12° and 155° with respect to the primary laser beam. The scattered light is coupled into a wave-guide via apertures. The signal detected by the photomultiplier is guided to the correlator and to the computer.

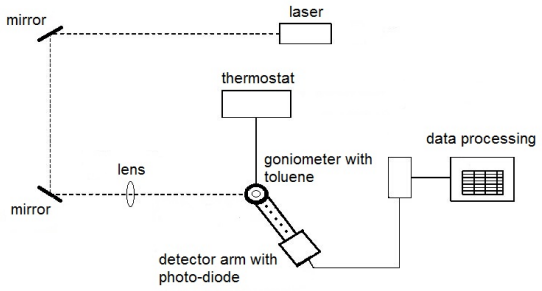

Figure 2.9.: Schematic overview of the ALV 5000E Compact Goniometer System (1-angle detection).

2.4.3. ALV/CGS3/MD-8 Multidetection Laser Light Scattering System

The ALV/CGS-3/MD-8 Multidetection Laser Light Scattering System from the *ALV-Laservertriebsgesellschaft* (Langen) is designed to measure static and dynamic light scattering at eight angles simultaneously. It is equipped with eight detectors, which are positioned in increments of 8°. With this set-up an angular regime of $20° \leq t \leq 136°$ can be covered corresponding to a q-range (depending on the solvent) of $5 \cdot 10^{-3}$-$2.7 \cdot 10^{-2}$ nm^{-1}. A He-Ne Laser with a wavelength of 632.8 nm and a power of 35 mW is used as a light source. The laser beam is deflected with two mirrors by 180°. It passes the beam attenuator, which provides seven stages of attenuation of the primary beam. A schematic overview of the instrument set-up is shown in Figure 2.10. The beam attenuator is a wheel on which seven filters are positioned circularly, so that a certain attenuation can be adjusted by rotation of the wheel. The attenuator is controlled by the general control unit (LSE) and can thus be operated automatically. In order to do so, the instrument goes through every attenuation stage from high attenuation to full laser intensity and checks the scattering intensity recorded at the detector with the smallest scattering angle θ for a user-defined limit of intensity. The process of going through the attenuation stages automatically, takes a few seconds $(\sim 8\ s)$ and reduces the time-resolution for time-resolved scattering experiments. Furthermore it is also possible to define manually a certain attenuation for the whole run of measurements. In this case the loss of time in a time–resolved experiment is minimized, but it is necessary to know the temporal evolution of the scattering intensity of the investigated sample.

After the attenuator the beam is guided via a beam splitter through a lens to the monitor diode, where the primary intensity of the laser beam is detected and measured. The other part of the beam is focussed by a second lens into the scattering cell. The scattering cell is located inside the index matching bath, which is a high precision, polished quartz container with two plane-parallel anti–reflection coated windows. It is filled with toluene, as it matches the refractive index of glass, in order to eliminate significant scattering effects from the interface glass-air. The temperature of the toluene bath inside the goniometer can be controlled via an external thermostat, which has to be connected to the goniometer. The goniometer is located on top of the rotation unit, which drives the

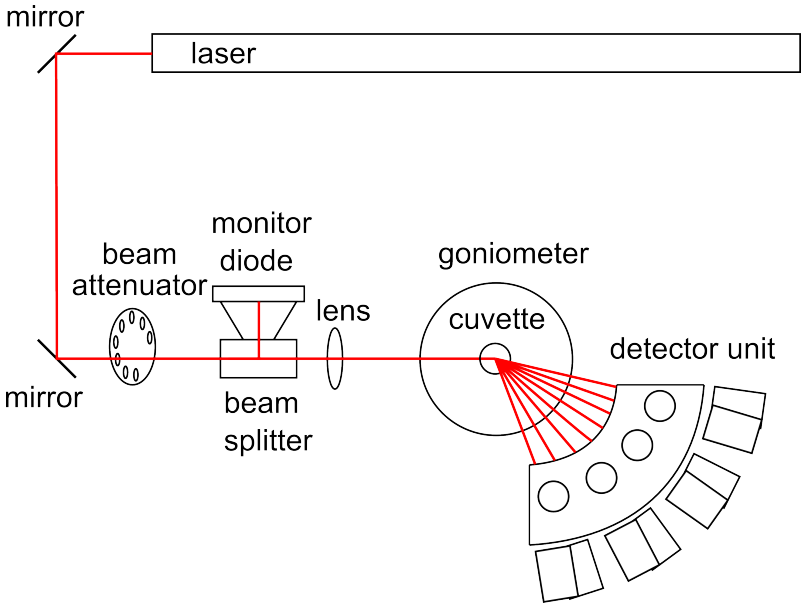

Figure 2.10.: Set-up of the ALV/CGS-3/MD-8 Multidetection Laser Light Scattering System: The laser beam is deflected via two mirrors by 180°, is guided through the attenuator wheel and focussed by a lens into the cuvette inside the goniometer. The primary intensity is detected by the monitor diode and the scattering intensity is injected into the eight wave-guides of the detector system.

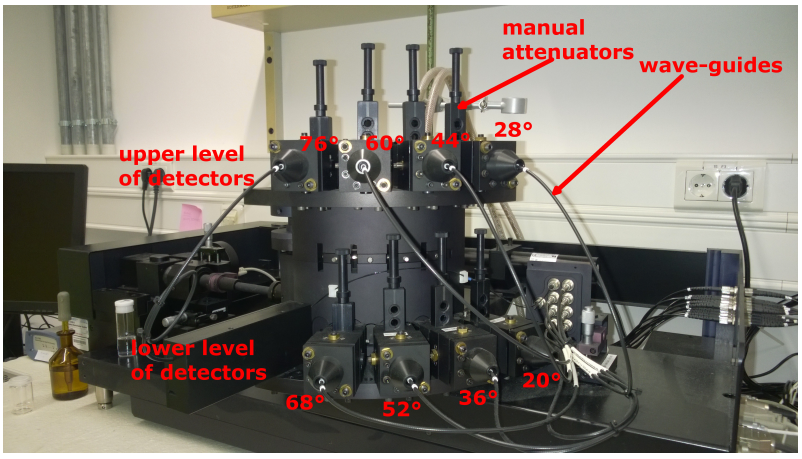

Figure 2.11.: Photography of the detector unit. The indicated scattering angles correspond to one selected position of the detector unit. In this case the reference needle, which is used for the beam adjustment is positioned at 0° to the beam, that corresponds to a scattering angle of the first detector of 20°. The manual attenuators have three different positions for attenuation of the scattering signal and one additional for shutting the scattering beam. For the two detectors corresponding to the highest scattering angles it is only possible to shut the scattering beam.

Table 2.2.: Possible transmission stages of the manual attenuation unit of the filters built in the instrument for all eight detectors and the corresponding measured transmission values. The most right column lists the respective measured detector sensitivities.

detector from low to high angle	transmission stages 100%	30%	10%	3%	1%	detector sensitivity
1	without filter	x	9.11	4.60	1.29	1.000
2	without filter	x	10.96	4.28	1.39	1.108
3	without filter	29.70	10.81	4.35	x	0.980
4	without filter	30.57	9.07	4.47	x	1.075
5	without filter	30.97	10.83	4.29	x	1.000
6	without filter	30.84	10.55	4.29	x	1.021
7	without filter	x	x	x	x	0.980
8	without filter	x	x	x	x	1.055

x: not possible

detector arm around the goniometer. On the detector arm eight combinations of lenses and apertures, one for each angle, guide the scattered light into wave-guides, which are connected with Avalanche diodes. The signal from each Avalanche diode is correlated as a function of time.

A second way to adjust the scattering intensity to the sensitivity of the detectors is to attenuate the scattering intensity arriving at the respective scattering angle by inserting three different filters into the light path before the laser light is guided into the wave-guide. The filters for the manual attenuation can be seen in Figure 2.11. This manual attenuation is possible for the detectors corresponding to the six smallest scattering angles. The two detectors corresponding to the two highest angles provide only the possibility to shut the beam completely. Table 2.2 gives an overview on the manual attenuation unit. For each detector three out of five different transmission stages 100%, 30%, 10%, 3% and 1% are possible. The detected scattering data has to be corrected for the proper attenuation, as in this case only the scattered intensity is attenuated but not the primary intensity. Therefore the precise transmission of the respective filter which is used has to be measured. These measured values for the transmission of the filters are additionally listed in Table 2.2.

A further correction factor which has to be taken into account is the detector sensitivity. Analogous to the attenuation by the dector filters, the detector sensitivities have to be measured in an experiment with high statistics. The sensitivity of one detector has to be defined as 1 and the detected scattering intensity of the other detectors has to be set in relation to the intensity of the reference detector by using an angular independent signal e.g. toluene. In our case the first detector is chosen as the reference detector. The detector sensitivities shown in Table 2.2 have been obtained with a measurement performed by the *ALV-Laservertriebsgesellschaft*. The sensitivity values have to be checked periodically

by a measurement.

The simultaneous detection of dynamic and static light scattering at eight scattering angles is a suitable technique for the investigation of particle growth. Although the time-resolution is smaller in comparison to static light scattering as it is limited by the correlation time, time-resolved dynamic light scattering provides in addition a diffusion coefficient, the shape-sensitive factor ρ and a possible particle distribution (correlation function) which is very important for a deeper insight into the process. The striking advantage of the ALV/CGS-3/MD-8 Multidetection Laser Light Scattering System comes with the detection of a whole scattering curve with eight different scattering angles at once. In this way fast growth processes can be captured by DLS and SLS. But one has to keep in mind, that an increasing number of scattering detectors may cause a decreasing quality of the instrument alignment, as it is more difficult to achieve the same degree of alignment for all detectors than it is for one detector. A standard deviation of ±1% for the scattering intensity over the whole angle regime, which is the guideline for a one-detector instrument, could not be achieved for the eight-detector instrument. The standard deviation of the eight-detector instrument lies in the worst case around ±5%, if the whole angle-regime is considered.

Furthermore we observe a shift in the scattering curve depending on the beam attenuation. Usage of the beam attenuation filters only has an influence on the intercept of the scattering curve and not on the slope of the scattering curve. The shift is more pronounced, if different attenuation filters are used for the measurement of the solvent and the sample. This is generally the case if the sample has a very high scattering intensity, which has to be reduced for the detector. The solvent is measured at 100% transmission, as the scattering intensity of solvents is normally very small. We found out that the shift of a scattering curve could be considerably reduced if the solvent measurement, which is used for the correction of the sample has been performed at the same attenuation stage as the sample measurement. Figure 2.12 depicts five scattering curves exemplarily in terms of Rayleigh ratio ΔR of polystyrene in toluene which have been performed at different attenuation stages and have been corrected with solvent measurements performed at different attenuation stages. If the measurement without attenuation for the sample and the solvent is considered as the reference measurement, an attenuation to 10%, corrected with a solvent measurement without attenuation, gives the largest deviations, followed by the scattering curve corresponding to an attenuation of the sample to 31%, corrected with a solvent measurement without attenuation. The best results can be achieved if the attenuation is the same for the sample and the solvent, although still a slight shift can be observed from 100% to 10%. As the reason for the effect of the attenuation filters on the scattering intensity is still unknown we tried to reduce the effect by using the same attenuation for the solvent and the sample where ever possible without using a correction factor or by application of a correction factor for the solution measurement in order to shift the values for weight-averaged molar mass. This correction factor has been determined with a measurement of toluene with high statistics for different attenuation stages. Usage of the correction factor became necessary as we are not able to measure the scattering intensity of a certain solvent with every attenuation stage. For example the scattering intensity of water is generally so low ($\approx$ 5 kHz), that a measurement with an attenuation stage smaller

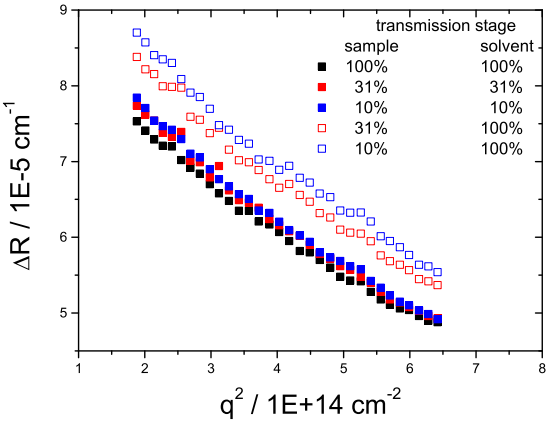

Figure 2.12.: Rayleigh ratio ΔR versus the squared value of the scattering vector q^2 from polystyrene in toluene performed with the ALV/CGS-3/MD-8 Multidetection Laser Light Scattering System. The scattering curves of the sample have been detected at different attenuation stages and have been corrected with solvent data measured at different attenuation stages.

than 31% is not possible. The deviations in the scattering curves caused by the attenuation of the primary beam should be controlled periodically.

Another issue, which has to be checked regularly, is the uniform focussing of the laser beam on the monitor diode. To this end, the monitor diode is divided into four quadrants. Every quadrant should detect on average the same intensity. This can be checked via the measurement software. In case of an irregular distribution it is possible that the monitor diode captures only a part of the primary intensity. The measured scattering intensity would then be referenced to a wrong primary intensity and the resulting Rayleigh ratio would be erroneous. The distribution of the laser beam intensity on the four quadrants of the monitor diode should serve as a control tool, because a shift in the distribution could indicate a misalignment of the laser beam for the whole instrument. However, the present instrument showed very often a shift of the laser distribution on the monitor diode without an obvious misalignment of the instrument. If the focus of the laser beam on the monitor diode was significantly misaligned, this deviation has been corrected by adjusting the lens, which focuses the laser beam on the monitor diode. This procedure was only followed after proper alignment of the instrument has been proved by a test measurement over the whole angular regime.

The silica samples investigated with this instrument have to be measured depending on the sample over a long time regime up to ≈120 h. In general the correlation time of one measurement amounts to 20 – 30 s, depending on the scattering intensity. Every 300 s one single measurement was performed. In between the measurements the laser beam was shut. For one kinetic run typically a number of 500 single measurements has been chosen. For the investigation of a few samples more than one run of 500 single measurements were required.

2.5. Preparation of Light Scattering Samples

All solutions for the light scattering experiments are prepared from a stock solution of sodium metasilicate with a concentration of 0.2 mol/l $Na_2H_2SiO_4 \cdot 8H_2O$ by dilution with water to a volume of 195 ml (in case of experiments with metal cations) or to a volume of 200 ml (in case of experiments in pure water). The concentrations investigated covered a concentration regime between 350 ppm and 3000 ppm. Successively, the pH value of the sample is adjusted to pH 7 or pH 8 by addition of 2 M HCl. The pH is measured by a Seven Easy pH meter from *Mettler Toledo*, which is calibrated before each measurement via three buffer solutions. The pH adjustment of the sample set the starting point of the experiment. For the experiments in the presence of calcium and magnesium ions 5 ml of a salt stock solution with a concentration of $[Ca^{2+}]+[Mg^{2+}] = 0.2$ mol/l at a ratio of $Ca^{2+} : Mg^{2+} = 4 : 1$ are added. In this way the resulting concentration of 4 mM Ca^{2+} and 1 mM Mg^{2+} corresponds to conditions typical for hard water. In case of the measurements in the presence of sodium chloride a salt stock solution of 0.4 mol/l NaCl were used. Here an addition of 5 ml of this solution results in a concentration of 10 mM Na^+ in the sample. Thus all solutions measured in the presence of metal cations were 0.01 N with respect to the added $(Mg_{1/5}Ca_{4/5})Cl_2$ or NaCl in addition to the NaCl inevitably formed during the initiation of the process by neutralization. The contribution of NaCl from the neutralization amounted to 0.012 N at 350 ppm, 0.013 N at 400 ppm, 0.016 N at 500 ppm, and 0.025 N at 750 ppm. Concentrations of silica denoted as c in evaluation of data from light scattering experiments are given in units of g/l where the concentration of solid $Na_2H_2SiO_4 \cdot 8H_2O$ is translated into a concentration of solid SiO_2 with a factor of 0.215. Alternatively, concentrations of silica are expressed as ppm of solid SiO_2.

For experiments in presence of polymers the aqueous polymer solution is added 1 min after the addition of the salt solution or right after the pH adjustment. The dilution effect, which is caused by the addition of the salt solution and/or the polymer solution was taken into account for the calculation of the used volume of the stock solution of sodium metasilicate yielding the desired total initial silica content for the respective experiment.

After the optional addition of the salt stock solution and/or the polymer stock solution the preparation of the sample is completed and the solution is filtered through a syringe filter with a pore size of 0.22 µm into a dust free scattering cell (Hellma, diameter: 20 mm, suprasil). Removal of possible dust from the scattering cells is achieved by flushing the scattering cell upside down with distilled acetone for several minutes. In order to avoid the silica formation by the silicate solution at the inner cell wall, the scattering cells are treated with a solution of 5 % chlorotrimethylsilane (98 %, *Janssen Chimica*) in toluene. Successful hydrophobization of the glass surface is noticeable by the changed surface energy, since the glass surface repels water after the treatment. In order to accelerate the growth process, all measurements with sodium silicate solutions are performed at 37 °C. The time regime analysed by light scattering measurements depends on the sample and varies from 2 h to 120 h. The measurement time of the single scattering experiments depends on the intensity of the sample and on whether dynamic and static light scattering is detected simultaneously or just static light scattering is performed.

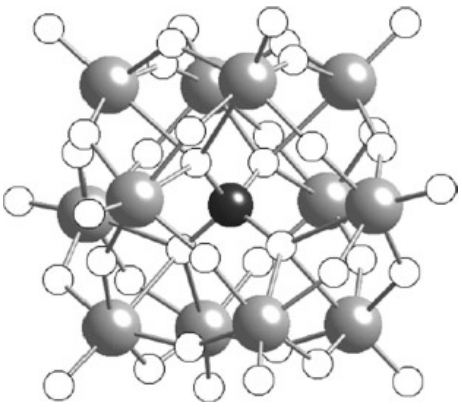

Figure 2.13.: Structure of Keggin-ion $[PW_{12}O_{40}]^{3-}$ (black spheres: P, grey spheres: W, white spheres: O), which is the analogous to the silico-12-molybdic acid cluster $[SiMo_{12}O_{40}]^{4-}$. The silicon atom is encaged by twelve MoO_6 octahedra. The molecular structure is reproduced from Ref.[84].

2.6. Determination of Monomeric Silica

2.6.1. Molybdenum Yellow and Molybdenum Blue Method

Consumption of the monomeric silicic acid during the silica polymerization is determined by means of the molybdenum blue method according to the *Standard methods for the examination of water and waste water*[82]. The method is based on the reaction of monomeric $Si(OH)_4$ with acidified ammonium heptamolybdate to the yellow heteropoly-acid silico-12-molybdic acid, which can be analysed by UV spectroscopy. The benefit of this procedure is the possibility to determine the concentration of monomeric silica in the presence of silica polymers, as the rate of the formation of silico-12-molybdic acid is much faster than the depolymerization of polysilicic acid in solutions at a very low pH. Silico-12-molybdic acid is formed according to

$$7Si(OH)_4 + 12H_6Mo_7O_{24} \cdot 4H_2O + 119H_2O \rightleftharpoons 7H_4SiMo_{12}O_{40} \cdot 29H_2O \qquad (2.34)$$

It is a yellow compound with an absorption maximum at $\lambda = 400 \pm 10$ nm. The pH value of the solution is the crucial parameter do distinguish between the α- and the β-form of silico-12-molybdic acid. The α-form is present at pH 3.8-4.8 and between pH 1.0 and pH 1.8 the β-form is more stable[83]. Both forms are yellow and can be used for absorption measurements in order to determine the concentration of monomeric silica. Silicomolybdic acid is a cage-like structure (Keggin-ion) where the silicon atom is in a tetrahedral cavity of the oxygen atoms belonging to four of the twelve surrounding MoO_6 octahedra (Figure 2.13). Therefore a reaction yielding silicomolybdic acid is only possible with monomeric silica.

The molar extinction coefficient at the maximum extinction at $\lambda = 400$ nm amounts to $\epsilon = 1500 \pm 201$ mol^{-1}cm^{-1}, which corresponds to a detection limit of 10^{-4} mol/l.[85] The lowest silica concentrations investigated in the present work are close to 170 ppm

corresponding to $3 \cdot 10^{-3}$ mol/l. As only very small volumes (~150 µl - 230 µl) are taken from the reaction mixture which additionally have to be diluted for the measurement, the silica concentration always lies below the sensitivity limit and hence does not provide sufficient accuracy for the analysis. This deficiency can be overcome by reducing the yellow species. This reaction stage can be described in a simplified way according to Equation 2.35

$$H_4SiMo_{12}O_{40} + \text{reducing agent} \rightarrow [H_4SiMo(VI)_8Mo(V)_4O_{40}]^{4-}. \tag{2.35}$$

Reduction yields molybdenum blue, with an absorption maximum at $\lambda = 810$ nm and a molar extinction coefficient $\epsilon = 44700 \pm 1501$ mol^{-1}cm^{-1}.[85] Accurate measurements in this case are possible to concentrations as low as to $5 \cdot 10^{-6}$mol/l.[85]

For all results presented in this work the molybdenum blue method was applied, which proceeds as follows.[82,22] A sample with a volume between 150 µl and 230 µl is removed from the reaction mixture with the actual amount depending on the expected silica content. The sample is diluted with water to a volume of 50 ml. After the addition of 1 ml of 50% (vol%) hydrochloric acid in water and 2 ml of an ammonium molybdate solution with a concentration of 100 g/l the sample is mixed and is allowed to stand for seven minutes. Subsequently 2 ml oxalic acid are added with a concentration of 75 g/l, followed by a second storage time of two minutes. Finally, 2 ml of the reducing agent are added. The reducing agent is prepared by mixing a solution of 23.05 g $Na_2S_2O_5$ in 150 ml water with a solution of 500 mg 1-amino-2-naphthol-4-sulfonic acid and 1 g Na_2SO_3 in 50 ml water. The UV-vis spectrum of the sample can be recorded five minutes after the addition of the reducing agent. As silicomolybdic acid is not stable, light absorption has to be measured at the latest 15 minutes after the addition of the reducing agent. The measurement is taken at a wavelength of 815 nm.

2.6.2. UV-vis spectrometry

Ultraviolet-visible spectroscopy is based on the Bohr-Einstein relationship, which describes the dependence of the discrete atomic or molecular energy states E_i on the frequency ν of the electromagnetic radiation.[86]

$$\Delta E = E_2 - E_1 = h\nu \tag{2.36}$$

If a electromagnetic beam impinges on a homogeneous sample, the beam can be attenuated beside scattering and reflection effects due to absorption by the sample. The molecules are raised to a higher energy state. According to the Lambert-Beer law the absorption A is given by the logarithmic ratio of the incident intensity I_0 and the transmitted intensity I. This ratio depends on the molar extinction coefficient in units of [l/(mol·cm)], the concentration c [mol/l] and the thickness of the sample in [cm].

$$A = log\frac{I_0}{I} = \epsilon cd \tag{2.37}$$

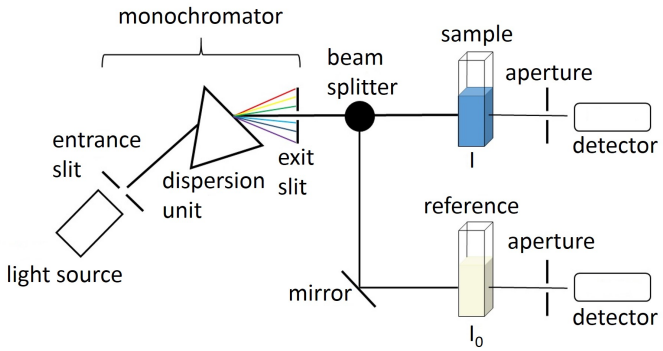

Figure 2.14.: Scheme of the double beam UV-vis spectrophotometer

A typical UV-vis spectroscopy measurement determines the intensity before and after passing through a sample. A schematic overview of a double beam UV-vis-spectrophotometer is given in Figure 2.14. The absorption spectra have been taken with a Lambda 19 (Perkin Elmer) spectrophotometer in the range between λ = 650 – 860 nm. As a light source serves a tungsten-halogen-lamp for the visible range of wavelengths and a deuterium-lamp for the UV-spectrum. Comparison of the absorbance at the maximum at λ = 815 nm of the sample with the absorbance of standard solutions of monomeric silica gives the concentration of monomeric silica in the sample. The determination of the calibration curve obtained via the measurement of silica standard solutions have been performed regularly. One example of such a calibration curve is shown in Figure 2.15. For the UV/VIS-measurements the solutions were filled into disposable PMMA cuvettes from VWR (Leuven, Belgium) with a volume of 3 ml and a path length of 10 mm. Each measurement was corrected with the absorbance of distilled water. The absorbance data were recorded by the program PerkinElmer WinLab.

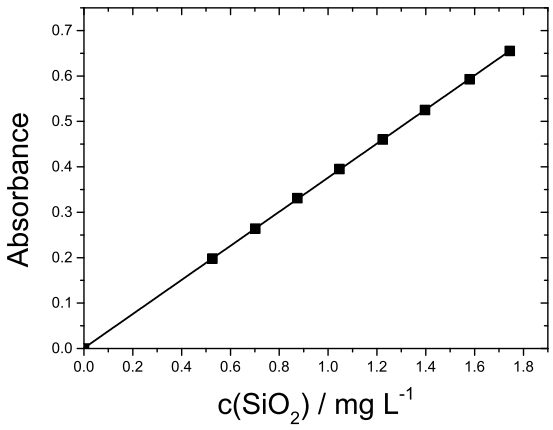

Figure 2.15.: Typical calibration curve obtained via UV/VIS-spectroscopy of silica standard solutions after application of the molybdenum blue method. The absorbance is detected at λ = 815 nm. A cuvette filled with pure water served as reference. The quality of the linear approximation is characterized by a coefficient of determination of R^2 = 0.999.

2.7. Dialysis of Polyelectrolytes

For the dialysis a small batch of ~2 g of PA and AA-AMPS-copolymer, solved in water, is adjusted to pH 9 with 1 M NaOH. After dilution to a volume of 100 ml the polymer solution is filled into a 50303 dialysis tube from *Reichelt*, which provides a separation limit of 1000 g/mol. The dialysis tube is placed into a dialysis container with a storage capacity of 10 l. The dialysis water in the container is also adjusted to pH 9 and is changed every 12 h. After 48 h the dialysis water is changed to pure water with a pH of 7. 96 h after starting the dialysis the volume of the polymer solution is reduced with the rotatory evaporator and is freeze dried.

2.8. Scanning electron microscopy (SEM)

A scanning electron microscope generates images of a sample by scanning it with a focused electron beam. The interaction of the electrons with the specimen produces several signals which can be analysed. Figure 2.16A shows the interaction volume of the electron beam with the specimen and lists the resulting signals. Three of these signals are used to generate images in scanning electron microscopy. Those are the secondary electrons (SE), the back-scattered electrons (BSE) and the characteristic x-rays. Secondary electrons are the result of the inelastic collision and scattering of incident electrons with specimen electrons. They are generally characterized by possessing energies of less than 50 eV and are used to reveal the surface structure of a material with a resolution in the nanometer range. Backscattered electrons are a result of elastic collisions and scattering events between incident electrons and specimen nuclei or electrons. Backscattered elec-

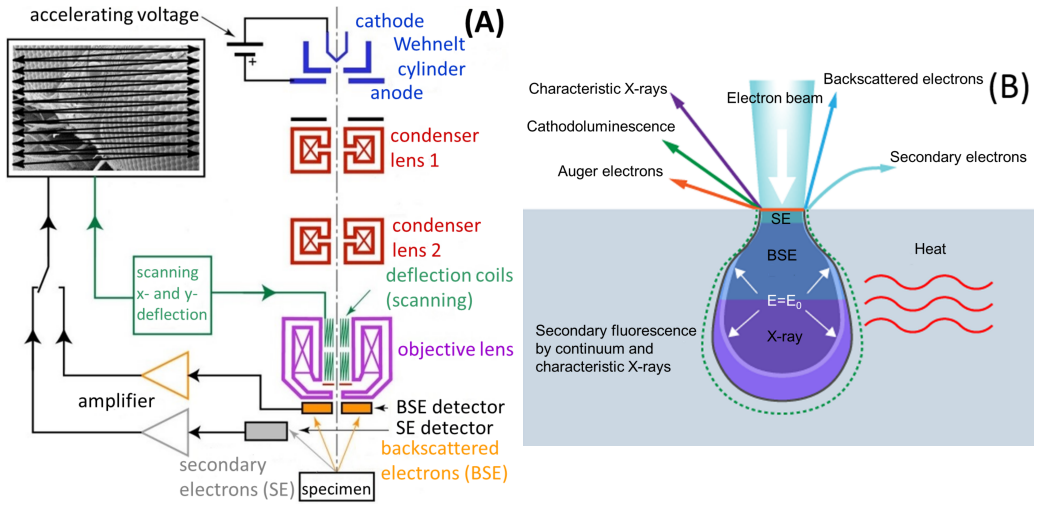

Figure 2.16.: (A) Principle of a scanning electron microscope;[87] (B) Schematic overview of the signals emitted from different parts of the interaction volume.[88]

trons are generated deeper in the material than the secondary electrons and help to resolve topographical contrast and atomic number contrast with a resolution of ~ 1 µm, this value is strongly depending on the accelerating voltage of the electron beam. The x-ray signal is a result of recombination interactions between free electrons and positive electron holes that are generated within the material. The x-ray signal is originated in zones of the specimen below those where secondary electrons come from and allows for determination of elemental composition through EDX (energy dispersive x-ray spectroscopy) analysis of characteristic x-ray signals.

Figure 2.16A shows a simplified set-up of a scanning electron microscope. The electron beam is emitted by an electron gun. Typical cathodes as guns are of tungsten or LaB_6. The electrons are accelerated by the applied voltage between the cathode and the anode. Focussing of the electron beam is performed by means of a Wehnelt cylinder and two condenser lenses. Deflection coils deflect the beam in x and y direction, in this way it scans in a raster fashion over a rectangular area of the sample surface. With the objective lens the electron beam is focused on the specimen. The detector for the back-scattered electrons is positioned above the specimen, the secondary electrons are detected with a detector positioned on one site of the specimen. The monitored signal of the secondary electrons and/or the back-scattered electrons is transformed into a digital image.

For the characterization of the silica particles formed in the presence of PA and the copolymer AA-AMPS the focused ion beam scanning electron microscope NEON 40 (Zeiss) was used. It has a resolution of 1 nm at a voltage level of 20 kV and a resolution of 2.5 nm at a voltage level of 1 kV. The SEM micrographs shown in this work have been generated by the signal of the detector for secondary-electrons. The samples were prepared by placing a few drops of the solution on a cleaned aluminium stub and by gentle evaporation of the solvent under ambient conditions.

3. Results and Discussions

3.1. Silica Polymerization - Experiments in Water

3.1.1. Variation of the Silica Content at pH 7

The concentration dependence of the silica polymerization at a pH = 7 was investigated by means of a concentration series of six samples having SiO_2 contents of 350 ppm, 400 ppm, 500 ppm, 750 ppm, 2000 ppm and 3000 ppm. Figure 3.1A summarizes the evolution of the weight-averaged molar mass for the concentration series up to a silica content of 750 ppm. The corresponding monomer consumption is depicted in Figure 3.1B. The silica polymerization shows a distinct lag-time depending on the initial silica content. During this lag-time the scattering of the sample remains close to the scattering of the pure solvent. The onset of monomer consumption nicely correlates with the end of this lag-time. As can be extracted from Table 3.1 the lag-time is reduced with increasing initial silica concentration, which is in line with the results of Rothbaum and Rohde et al.[37]. The sample with the highest silica content out of the four lower concentrations exhibits no lag-time and shows a fast decay of the monomer concentration. All four samples approach a plateau value in mass and size (Figure 3.1 and Figure 3.2). Noteworthy, the monomer concentration shown in Figure 3.1B decreases while the weight-averaged particle mass is increasing toward the plateau value and the time where this plateau value is reached correlates with the time at which the monomer concentration reaches the solubility limit (170 ppm SiO_2). This strongly suggests that particle growth occurs by an addition of monomers. As will be demonstrated in the following paragraphs, a detailed analysis of the data confirms this mechanism. However, the exact nature of the "monomer" has to remain unknown.

As it can be inferred from the very small hydrodynamic radii of the silica particles

Table 3.1.: Lag-time, final hydrodynamic radius and final weight-averaged molar mass observed at variable SiO_2 content measured at pH = 7.

	SiO_2 [ppm]	lag-time [h]	final R_h [nm]	final M_w [g mol^{-1}]
pH 7	350	57.4	17	1.69E5
	400	19.4	14	9.55E4
	500	2.12	5.7	7.53E3
	750	0	4.6	4.42E3

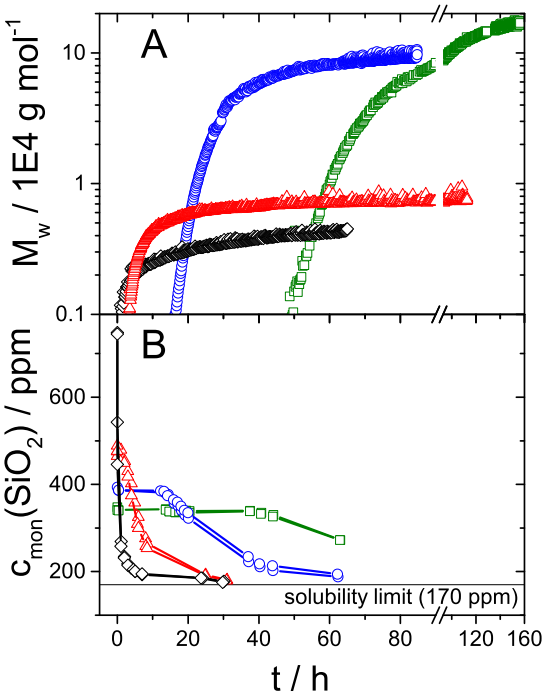

Figure 3.1.: Formation of silica particles as a function of time in water at pH 7 at variable silica concentration: 350 ppm (□), 400 ppm (○), 500 ppm (△), 750 ppm (◇). (A) Weight-averaged molar mass from SLS; (B) consumption of the monomeric silica measured with the molybdenum blue method.

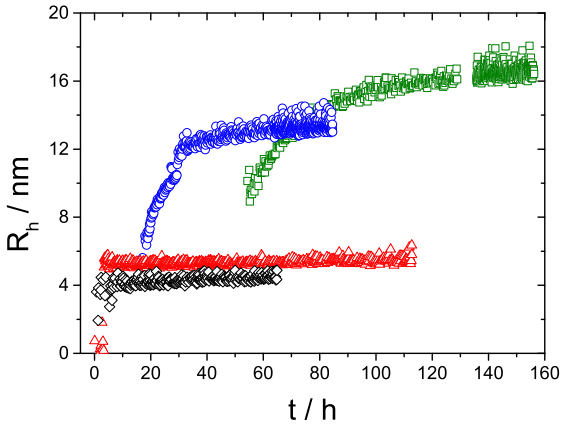

Figure 3.2.: Hydrodynamic radius of silica particles as a function of time in water at pH 7 at variable silica contents from DLS: 350 ppm (□), 400 ppm (○), 500 ppm (△), 750 ppm (◇).

a formfactor of the particles is not accessible via angular dependent SLS. In order to still get structure information on the particles we use the correlation of the particle size with the weight-averaged molar mass of the ensemble. The correlation follows a power law with a shape sensitive exponent α for self-similar structures. Compact spherical structures lead to an exponent of $\alpha = 1/3$ and polymer coils under ideal conditions give a value of $\alpha = 1/2$.[89] Such an exponent would in fact be observed if particle growth proceeds via a step-growth, i.e. any particle reacts with any other particle in solution corresponding to a monomodal size distribution. Once particles are formed via a monomer-addition process, the weight-averaged molar particle mass, given by $M_w = \Delta R_{\theta=0}/Kc$, describes an average of a bimodal ensemble of monomers and growing particles if the entire silica concentration c_0 corresponding to the concentration at t = 0 is used for the calculation only. Knowledge of the monomer concentration of silica $c_{mon}(t)$ would enable us to also calculate the concentration of growing particles $c_{part}(t)$ according to Equation 3.1

$$c_{part}(t) = c_0 - c_{mon}(t) \tag{3.1}$$

and along with it to calculate an additional weight-averaged mass for the particles only with $c_{part}(t)$ used in Equation 2.3. However, if the mass values of an ensemble of growing particles and small monomers for a monomer-addition process are based on c_0 the topology based exponent is decreased by a factor of 1/2. Accordingly, compact spherical structures formed in a monomer-addition process follow an exponent of $\alpha = 1/6$.

The molar mass values from the time-resolved data in Figure 3.3 were calculated with a constant initial silica concentration thereby at any time representing the weight-average of monomers and particles. The samples with a silica content of 350 ppm and 400 ppm show a good agreement with $\alpha = 1/6$. The smallest possible exponent based on the topology of the particle is $\alpha = 1/3$, indicating homogeneous spherical structures. An even lower value of $\alpha = 1/6$, observed here is only explainable by the formation of spherical particles via a monomer-addition process. Unlike to the two lowest silica contents, the samples with a silica content of 500 ppm and 750 ppm do not show a distinct power law because no significant regime of an increasing hydrodynamic radius could be detected anymore.

In order to still prove consistency of data interpretation, we consider in addition the correlation of the final hydrodynamic radius and mass for all four silica contents, whereas the mass has been calculated with the concentration of growing particles $c_{part}(t)$ based on Equation 3.1. In cases where particle formation is still going on, an estimation of $c_{mon}(t)$ can be given from the monomer consumption recorded by the molybdenum blue method. In cases where final plateau values for the averaged particle mass M_w are reached, the extent of consumption of monomers can be assumed to correspond to $c_0 - c_{mon}(t = t_{max})$ with $c_{mon}(t = t_{max}) \approx 170$ ppm SiO_2 corresponding to the equilibrium concentration. Since plateau values are reached for all four silica contents, final M_w values were calculated by using the concentration $c_{part}(t = t_{max})$ according to Equation 3.1, which does not include the non-consumed (soluble) monomers anymore. The resulting correlation is plotted in Figure 3.3, and reveals an exponent of $\alpha = 1/3$. This is the value expected for compact structures based on topological considerations. The behaviour of the exponent based on

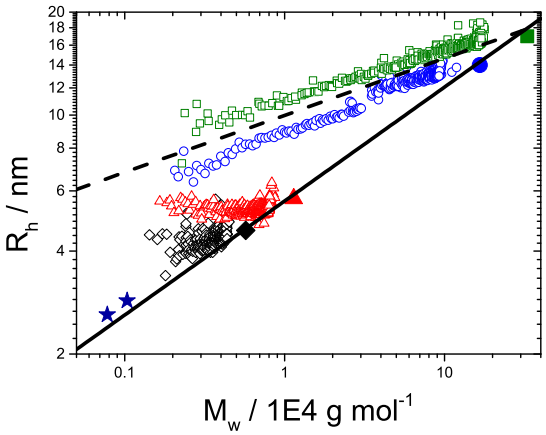

Figure 3.3.: Correlation of the hydrodynamic radius with the weight-averaged molar mass at variable silica contents: 350 ppm (□), 400 ppm (○), 500 ppm (△), 750 ppm (◇). Full symbols show the corresponding correlation of $R_h(t = t_{max})$ with the final values of $M_w = \Delta R_{\theta=0}/Kc_{part}(t = t_{max})$. The dashed line indicates a slope of $1/6$ and the straight line a slope of $1/3$. The blue stars indicate the two first measurement points of the experiment with a silica content of 2000 ppm.

mass values including and excluding the monomer concentration is a clear hint for the consistency of our data treatment based on a binary system with monomers and polymers only and of a monomer-addition mechanism of the silica polymerization under the present conditions.

The silica polymerization at considerably higher silica contents of 2000 ppm and 3000 ppm obeys a mechanism different from the one observed in the regime of low silica contents at pH 7. Noticeably, the particle growth predominantly occurs in a time regime in which no further change of the monomer concentration is observed. As it is nicely demonstrated in Figure 3.4, monomers have been used up to the solubility limit at $t < 0.2$ h, whereas the main increase in the molar mass occurs after this solubility limit has been reached. This indicates that the particles grow via aggregation of constituent particles formed at $t < 0.2$ h, thereby exhibiting much higher values in mass and in particle size than those observed at the lower silica contents of 350 ppm-750 ppm.

The large values of the particle size enable the determination of the radius of gyration R_g in addition to R_h. The trend of the hydrodynamic radius as well as of the radius of gyration together with the resulting structure-sensitive factor ρ as a function of time is given in Figure 3.5. Similar to the trend of the weight-averaged molar mass a faster increase of the particle size is observed with increasing initial silica content. None of the experiments at very high silica concentrations (2000 ppm and 3000 ppm) reaches a plateau value in mass and size during the investigated time regime. For a silica content of 2000 ppm we observe an almost linear increase of the particle size until $t = 12.5$ h. Thereafter the slope of the curve decreases only slightly. This coincides with the time at

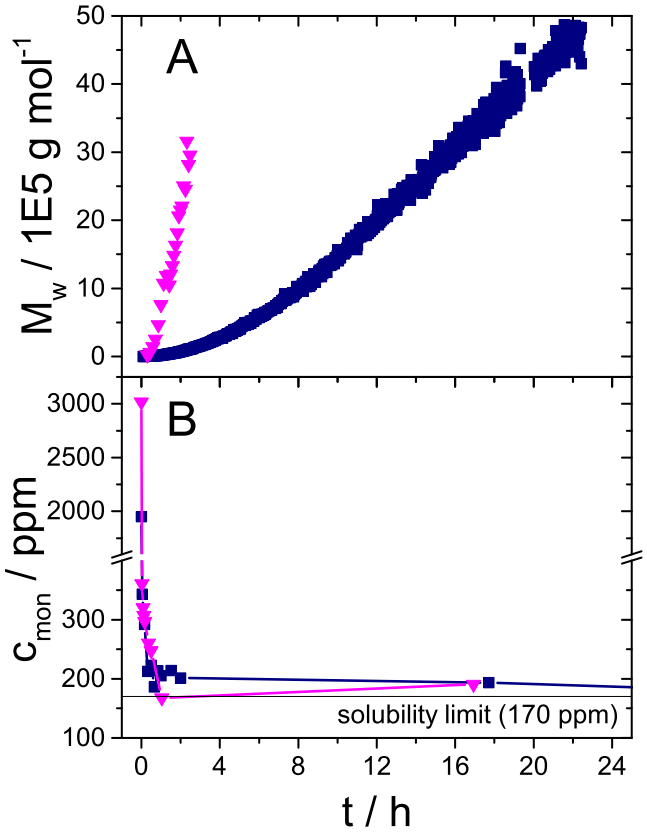

Figure 3.4.: Evolution of the silica particle growth at pH 7 for the two silica concentrations 2000 ppm (■) and 3000 ppm (▼). (A) Time dependence of the weight-averaged molar mass; (B) consumption of the monomeric silica versus time.

which the ρ-value crosses the value of one. The structure-sensitive parameter according to a silica content of 2000 ppm shows a decreasing trend from $\rho \approx 1.3$ to 0.9. One could interpret this trend as an increasing compactness of the particles, although the experiment with a silica content of 3000 ppm does not show such a clear hint. In this case the ρ-value fluctuates between $\rho = 1.5$ and 0.9. This interpretation has to be considered with care due to following aspect. A decrease of R_g below the value of R_h could occur due to a lowering quality of the applied Guinier approximation. The light scattering data is based on a fixed q-range, but with increasing particle size, the Guinier regime is shifted toward lower q. Thereby the Guinier regime may gradually leave the q-range accessible by the instrument. As a rule of thumb this shift begins to have an influence once R_g gets close to 200 nm.

A consideration of the size-mass correlation (Figure 3.6) shall complement our view on the structures formed from highly supersaturated silica solutions (2000 ppm and 3000 ppm). For the determination of the mass values shown in Figure 3.6 the total silica

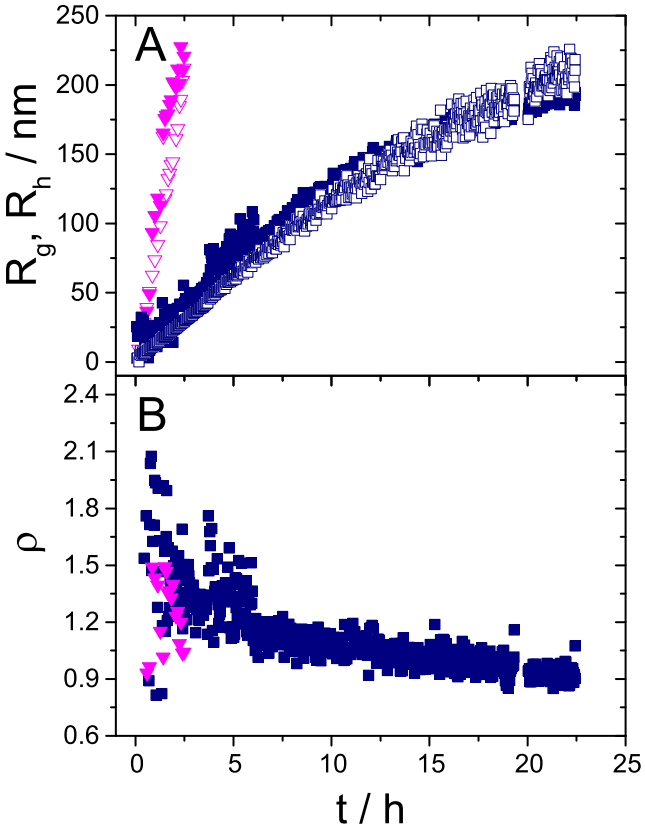

Figure 3.5.: Evolution of the radius of gyration R_g, the hydrodynamic radius R_h (A) and the corresponding ρ-ratio (B) according to Equation 2.19 at pH 7 for the silica contents of 2000 ppm (R_g (■), R_h (□), ρ (■)) and 3000 ppm (R_g (▼), R_h (▽), ρ (▼)).

concentration was used according to $M_w = \Delta R_{\theta=0}/Kc_0$. The radius of gyration as well as the hydrodynamic radius exhibit a power law of $1/2$ over a wide regime of mass M_w. Only for very high molar masses the correlation of the radius of gyration decreases slightly in line with a small change in ρ, which might indicate that the sequence of growing intermediates may not be entirely self-similar. However, the onset of this slight deviation, may be due to the already mentioned gradual shift of the Guinier regime toward lower q, as the particles are growing. If we now assume, based on the previous observations of the size-mass correlation, a monomer-addition mechanism, we can expect a reduced exponent by a factor of 1/2, as the total silica concentration c_0 has been used for the data evaluation. Therefore an exponent of $1/2$ leads to a topological exponent of 1, which corresponds to a rod-like structure. However, in the context of general knowledge about structure formation of colloidal silica, a rod-like structure seems to be very unusual. This view is further

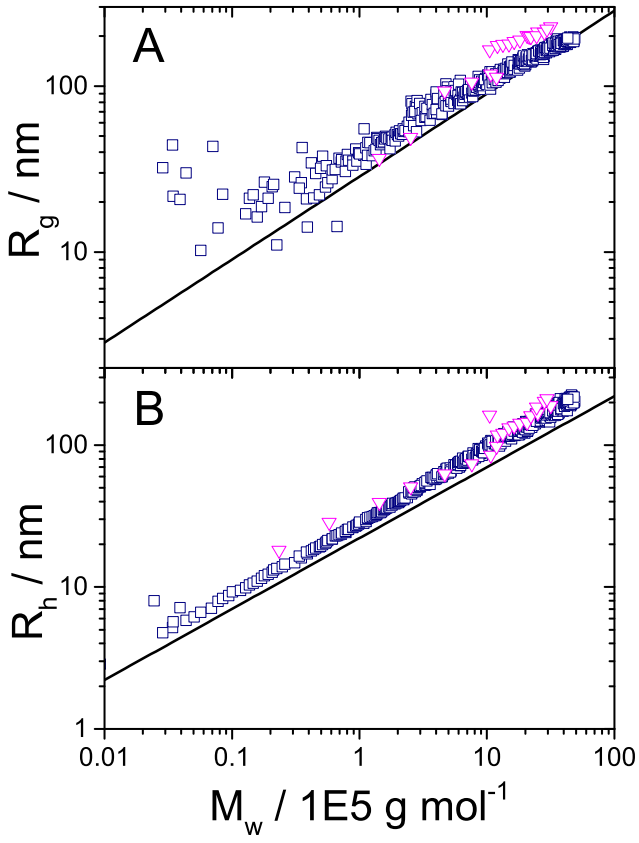

Figure 3.6.: Particle size for the silica polymerization at pH 7 at the two highest silica contents used: 2000 ppm (□) and 3000 ppm (▽). (A) Correlation of R_g with M_w; (B) correlation of R_h with M_w. The lines indicate a slope of $1/2$.

supported by the ρ-values which are lower than expected for rod-like particles[90]. Under the assumption that no monomer-addition mechanism takes place, but an aggregation of smaller particles to clusters, an exponent of $1/2$ would suggest a fractal dimension similar to that of polymer coils. Therefore the size-mass correlation provides the second hint for an aggregation process in case of highly supersaturated silica solutions (2000 ppm and 3000 ppm). An aggregation process has been already indicated by an increasing weight-averaged molar mass during a time regime in which the monomer concentration equals its equilibrium concentration.

A consideration of a formfactor (Figure 3.7) of the particles, which was taken at $t \sim 19$ h after initiation of the reaction confirms the mechanism of a particle-particle aggregation. It shows good agreement with the formfactor of a Gaussian coil[66] even at the latest stages of the growth process, which further verifies a fractal dimension close to the one of polymer coils obtained already by the mass-size correlation.

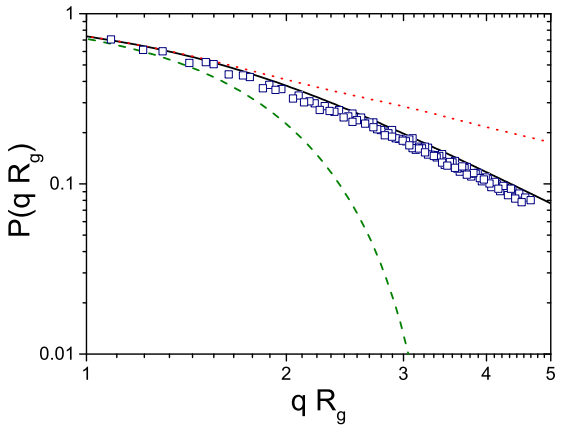

Figure 3.7.: Formfactor of the sample with a silica concentration of 2000 ppm (□) at $t \sim$ 19 h compared with a formfactor of a monodisperse, hard sphere[67] (– – –), a monodisperse coil[66] (—) and a stiff rod[65] (···).

To conclude, we summarize the following results. At low silica concentrations (350 ppm-750 ppm) compact structures are formed via monomer-addition. At higher silica concentrations (2000 ppm, 3000 ppm) the particles agglomerate to fractal-like clusters. It is this switch in morphology, setting in with the aggregation, which excludes Ostwald ripening as the main process driving the growth at silica contents higher than 1000 ppm. However, we suggest that the trend of an increase in nucleation rate accompanied by a decrease in size of the spherical particles, formed during monomer-addition growth extends as well into the regime of higher silica contents (2000 ppm and 3000 ppm). Hence, a short time after initiation an even higher number of small spherical particles is formed at silica contents of 2000 ppm and 3000 ppm. This is nicely supported by the first two data points recorded for the experiment with a silica content of 2000 ppm at t = 4.8 min (M_w = 7.7E + 3 g/mol, R_h = 2.6 nm) and at t = 6.7 min (M_w = 1.0E + 3 g/mol, R_h = 2.9 nm) which satisfactorily fit into the trend of Figure 3.3 (indicated as blue stars). For this comparison, the mass values have been evaluated based on the mass concentration c_{part} of the growing particles according to Equation 3.1. The corresponding monomer concentrations ($c_{mon}(t)$) have been approximated from the results of the monomer consumption (Figure 3.4B).

Obviously, the particle number concentration at contents of 2000 ppm or larger is high enough to overcome the stabilization effect caused by surface charges and particle-particle aggregation sets in. It is known from the literature that silica sols begin to gel above pH 6, if the salt concentration amounts to 0.1 – 0.2 mol/l and the silica concentration is at least 1-2%.[22] In case of a SiO_2 content of 2000 ppm, which is equal to a silica concentration of 0.2%, the corresponding sodium ion concentration amounts to 0.07 mol/l. Based on the presented measurements we could show that an aggregation of spherical sol particles already starts if only the counter ions of sodium metasilicate, which serves as the silica source, are present. Furthermore the light scattering results

clearly show the existence of fractal-like structures. These structures are probably formed by the collision of spherical particles and fractal-like particles, which are then connected via siloxane bonds from surface to surface.

3.1.2. Variation of the Silica Content at pH 8

The silica polymerization in pure water introduced in Chapter 3.1.1 has been also studied at pH 8. At this pH, the initial silica concentration has been varied between 350 ppm and 2000 ppm. Figure 3.8 compares the weight-averaged molar mass and the monomer consumption at pH 8 with that observed at pH 7. In general, a decreasing final weight-averaged molar mass with increasing silica content can be observed for both pH values between 350 ppm and 750 ppm. The absolute values are lower for pH 8. The monomer consumption is faster at pH 8 than that at pH 7. This trend is accompanied by a reduced lag-time. Hence, the nucleation is accelerated by an increase of the pH value from 7 to 8, which is confirmed by the decreased mass and size of the particles at pH 8 in comparison to pH 7, as a faster nucleation leads to a higher number of nuclei and therefore to smaller particles at a given amount of monomer.

The observed hydrodynamic radii are at the limit of detection and exhibit higher uncertainties than at pH 7. Therefore only the final values of R_h are accessible. The general trend of the final M_w- and R_h-values as a function of the initial silica content is summarized for both pH values in Figure 3.9. Whereas data recorded at pH 7 are restricted to silica contents up to 750 ppm, data from all silica contents analysed at pH 8 are included. Since equilibrium states have been reached in all these cases, all final values for M_w are based on $c_{part}(t = t_{max})$ established with Equation 3.1. For the value $t = t_{max}$ it is assumed that the monomer consumption is completed and accordingly $c_{mon}(t = t_{max} =$ 170 ppm

For higher silica contents ($c_0 > 750$ ppm) the results recorded at pH 8 deviate from those at pH 7. Whereas at pH 7 for very high silica contents (2000 ppm and 3000 ppm) an aggregation process sets in, at pH 8 the particles keep a small size (4 – 5 nm) with similar weight-averaged molar mass as observed with 750 ppm SiO_2, hence excluding an aggregation of particles. From this, we can conclude that the concentration threshold for the onset of an aggregation process is shifted to higher silica contents as the pH increases. A reason could be a better stabilization of the particles in a solution with higher pH due to a higher number of charged groups on the particle surface.

A correlation according to Equation 2.20 is shown by Figure 3.10. It allows us to state, that the correlation of the final size and mass values at pH 8 is similar to the power law observed at pH 7 for the silica contents 350 ppm, 400 ppm, 1500 ppm and 2000 ppm, only a shift toward lower M_w-values can be determined. This indicates a lower mass density of the formed particles. The strongest deviation from the slope of compact structures ($\alpha = 1/3$) is shown by the values of 500 ppm and 750 ppm initial silica. For these two concentrations a rather low and stable molar mass and size is observed. Two reasons for the deviation of these two samples from the general trend can be offered: (i) The sensitivity limit of light scattering is reached, which is also obvious by the higher statistical errors of these data points. (ii) At 750 ppm SiO_2 nucleation is most extensive

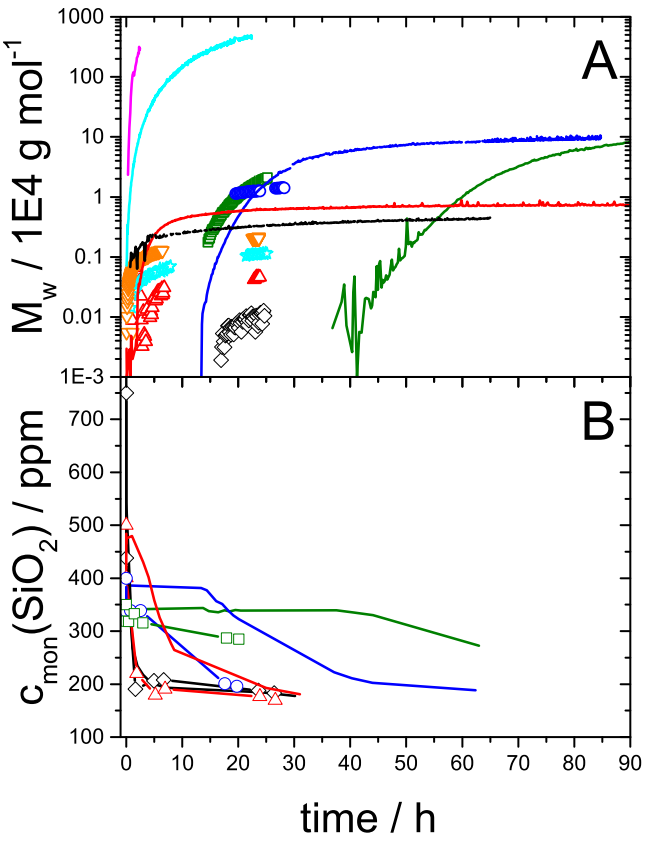

Figure 3.8.: Comparison of the evolution of the weight-averaged molar mass (A) and the monomer consumption (B) for various silica contents at pH 7: 350 ppm (—), 400 ppm (—), 500 ppm (—), 750 ppm (—), 2000 ppm (—), 3000 ppm (—) and pH 8: 350 ppm (□), 400 ppm (○), 500 ppm (△), 750 ppm (◇), 1500 ppm (☆), 2000 ppm (▽).

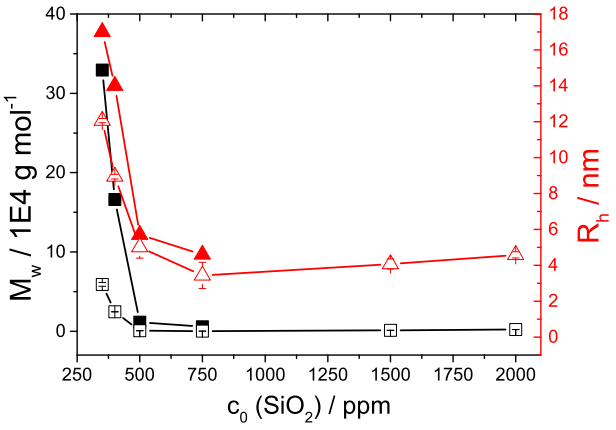

Figure 3.9.: Final weight-averaged molar mass corresponding to $M_w = \Delta R_{\theta=0}/Kc_{part}(t = t_{max})$ at pH 7 (■) and pH 8 (□) and final hydrodynamic radius $R_h(t = t_{max})$ at pH 7 (▲) and pH 8 (△) as a function of the initial silica content.

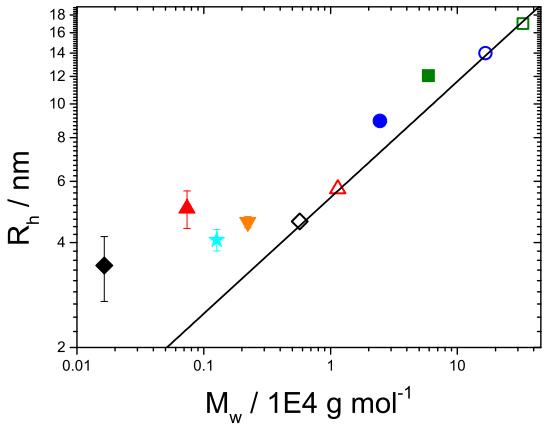

Figure 3.10.: Correlation of the weight-averaged molar mass $M_w = \Delta R/Kc_{part}(t = t_{max})$ with the hydrodynamic radius $R_h(t = t_{max})$ at variable silica contents at pH 8: 350 ppm (■), 400 ppm (●), 500 ppm (▲), 750 ppm (◆), 1500 ppm (★), 2000 ppm (▼). The line and the empty symbols indicate the trend of the correlation for the final size and mass values at pH 7 (α = 1/3, see also Figure 3.3): 350 ppm (□), 400 ppm (○), 500 ppm (△), 750 ppm (◇).

and a minimum in mass and size is reached, the resulting nuclei / small particles are not able to grow further, because most of the monomers may have been consumed by the formation of nuclei. The nuclei / small particles which consist of just a few monomer units, may not further belong to the regime of the self-similarity of the particles. As a result they do not fit to the size versus mass correlation. Increasing the concentration to 1500 ppm and 2000 ppm at pH 8 has two effects: The drastically enlarged concentration leads to a further increased number of nuclei and also to a growth of the nuclei by the addition of monomers. Both effects increase the scattering signal and therefore decrease the statistical error of the measurement. Hence the final size and mass values may again approach the scaling law of compact, spherical particles, as observed in Figure 3.3.

3.2. Silica Polymerization - Experiments in the Presence of Metal Cations

Silica polymerization in industrial plants leads to undesirable silica scaling and fouling on different components of these facilities like membranes in desalination devices, water treatment systems, cooling and heating cycles. Typical conditions prevailing in industrial plants could be an elevated temperature, different pH regimes and the presence of other low concentrated ions, as usually supply water or sea water and not ultrapure water is used. In order to get a broad overview on the influence of metal cations on the kinetics of the silica polymerization additional experiments in the presence of monovalent sodium ions and a mixture of divalent calcium and magnesium ions on the silica polymerization have been performed. A concentration series of four samples with silica contents of 350 ppm, 400 ppm, 500 ppm and 750 ppm has been investigated, respectively. A salt concentration of $[M^{2+}]$ = 5 mM and a ratio of Ca : Mg = 4 : 1 has been selected in order to generate conditions typical for hard water. Investigation of the influence of sodium ions has been performed in order to enable comparison with the impact of the most simple and inert type of salt. The samples already content a certain amount of NaCl which is formed during the initiation of the reaction by neutralization. The additional Na^+ concentration, which is introduced by the addition of the NaCl stock solution amounts to 10 mM.

The left column of Figure 3.11 represents experiments at pH = 7 in the presence of Ca^{2+}+Mg^{2+}-ions at variable silica contents. The growth rate as well as the finally reached molar mass strongly depends on the initial silica content. The trends of the molar mass determined by SLS of all four samples correlate nicely with the consumption of the silica monomers determined by means of the molybdenum blue method (left column Figure 3.11B). For all samples the equilibrium concentration of 170 ppm SiO_2 was reached at the end of the growth of silica particles. The three lowest concentrations (350 ppm - 500 ppm) exhibit a distinct lag-time which decreases with increasing initial silica content. During the lag-time the scattering contribution is comparable to the scattering signal of the solvent and the monomer concentration keeps close to the initial silica concentration. After this characteristic lag-time the decrease of the monomer concentration coincides by the increase of the molar mass and both values reach an equilibrium value.

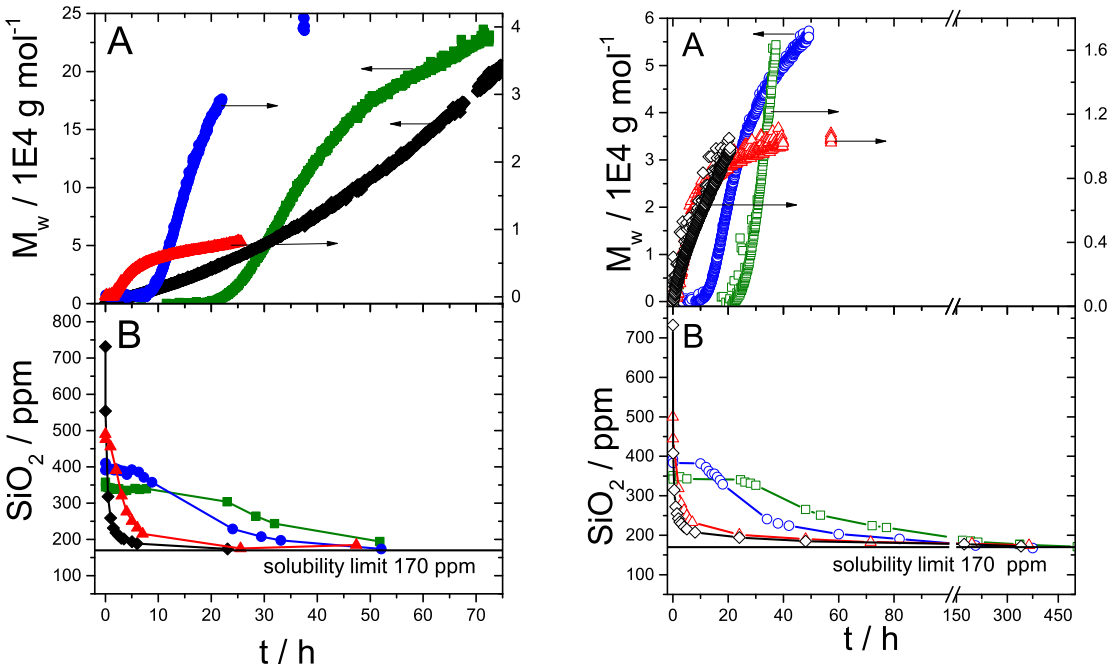

Figure 3.11.: Formation of silica particles in water as a function of time at pH 7 at variable silica content. (A) Weight-averaged molar mass from SLS, the experimental mass values refer to two different scales with arrows pointing to the corresponding axis; (B) consumption of the monomeric silica from the molybdenum blue method. **Left**: Experiments with Ca^{2+}+Mg^{2+}: 350 ppm (■), 400 ppm (●), 500 ppm (▲), 750 ppm (◆). **Right**: Experiments with Na^{+}: 350 ppm (□), 400 ppm (○), 500 ppm (△), 750 ppm (◇).

Only the highest silica content (750 ppm) shows a different behaviour. In this case no lag-time is observed. The consumption of the monomers up to the equilibrium limit of 170 ppm is completed within $t < 10$ h, while the molar mass keeps increasing beyond this time without reaching a plateau value. It is highly probable that particle formation at the silica content of 750 ppm during the first hours proceeds via monomer-addition in very much the same way as in case of the lower silica contents. However, this process is completed during the first 10 hours and smoothly followed by another growth step whereby the particles resulting from monomer-addition establish the smallest units in this next growth step. As analysis of the joint SLS and DLS data will show, fractal-like aggregates are formed in this third step.

Similar trends for the evolution of the particle mass and the consumption of monomers are observed for the silica polymerization in the presence of Na^{+}-ions, which is shown by the right column of Figure 3.11. A good correlation between the loss of monomers and the increase of mass is observed for all four silica contents. In analogy to

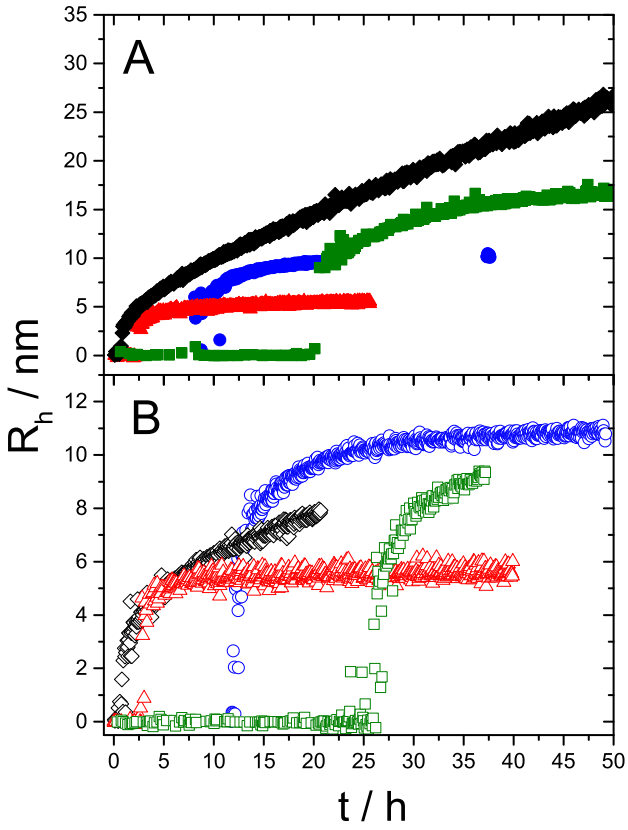

Figure 3.12.: Hydrodynamic radius from DLS of silica particles as a function of time in water at pH 7 at variable silica contents: (A) in the presence of Ca^{2+}+Mg^{2+}-ions at 350 ppm (■), 400 ppm (●), 500 ppm (▲), 750 ppm (◆); (B) in the presence of Na^{+}-ions at 350 ppm (□), 400 ppm (○), 500 ppm (△), 750 ppm (◇).

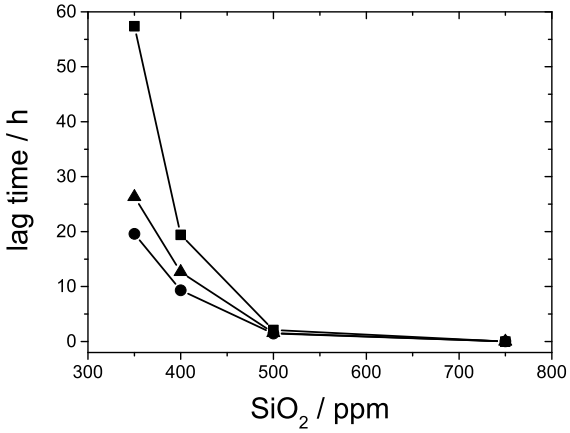

Figure 3.13.: Lag-time versus initial silica content for the measurement series without further salt addition (■), in the presence of Na^+-ions (▲) and in the presence of Ca^{2+}+Mg^{2+}-ions (●). The data recorded in salt-free solution are taken from Chapter 3.1.1.

the measurements in the presence of Ca^{2+}+Mg^{2+}-ions the silica contents 350 and 400 ppm exhibit a significant lag-time during which no monomer is consumed and scattering intensity is comparable with the scattering intensity of the solvent. After this lag-time which decreases with increasing silica content a fast increase of the particle mass and simultaneously a decrease of the monomers is observed until the monomers reach the equilibrium concentration of 170 ppm SiO_2.

Figure 3.12 compares the temporal evolution of the hydrodynamic radius of the samples in the presence of Ca^{2+}+Mg^{2+}-ions (Figure 3.12A) with the respective results collected for the samples in the presence of additional Na^+-ions (Figure 3.12B). As expected from the evolution of the particle mass in the presence of Ca^{2+}+Mg^{2+} a distinct lag-time is followed by a short period of an increasing particle size, which approaches a constant value for low silica contents (350 ppm – 500 ppm). At 750 ppm R_h increases almost linearly with t without approaching a plateau. Similar trends can be observed in the presence of Na^+-ions, only the absolute lag-times at the silica contents between 350 ppm and 500 ppm are slightly longer than in the presence of Ca^{2+}+Mg^{2+}-ions. Final sizes of the particles formed in the presence of Ca^{2+}+Mg^{2+}-ions and in the presence of additional Na^+-ions are comparable. The evolution of R_h at 750 ppm SiO_2 in the presence of Na^+ shows the same linear increase with t as in the presence of Ca^{2+}+Mg^{2+}.

In close analogy to the growth in pure water the final particle size decreases with increasing initial silica content in the presence of metal cations (Figure 3.13). This indicates that the nucleation rate increases with increasing silica content. A faster nucleation generates a larger number of nuclei, which have to share the respective amount of monomers available. Hence, a lower number of nuclei, resulting from a slower nucleation, leads to larger particles. As inferred from the lag-times (Figure 3.13), monovalent and divalent cations accelerate the silica polymerization. The lag-time τ obeys the following

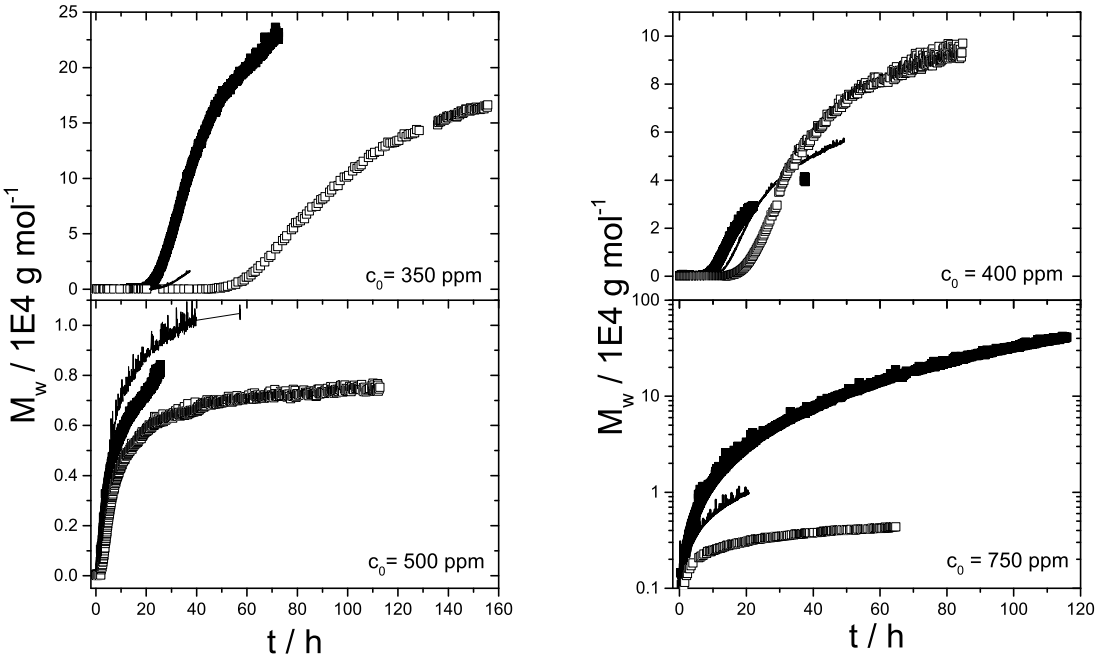

Figure 3.14.: Evolution of M_w from SLS at pH 7: Experiments in pure water (□), in aqueous solution of Na^+-ions ([Na^+] = 10 mM) (—) and in aqueous solution of Ca^{2+}+Mg^{2+}-ions ([Ca^{2+}]/[Mg^{2+}] = 4/1) at [Ca^{2+}]+[Mg^{2+}] = 5 mM (■). The respective initial silica content is indicated in the graph.

trend: τ (salt free) > τ (Na^+) > τ(Ca^{2+}+Mg^{2+}). The lower the initial silica concentration the larger the reduction of the lag-time gets upon the addition of metal cations.

The trends discussed are nicely supported by a comparative discussion of the evolution of M_w with time done separately at each silica content for the three investigated conditions (Figure 3.14). At silica contents of 350 ppm, 400 ppm and 750 ppm the increase of M_w is accelerated in the same series already observed for the lag-time: (reference) < Na^+ < Ca^{2+}+Mg^{2+}. Just in case of 500 ppm the mass of particles formed in the presence of Na^+ increases faster than the mass of the particles formed in the presence of Ca^{2+}+Mg^{2+}. Accordingly, the lag-time is reduced considering the three silica contents 350 ppm, 400 ppm and 500 ppm. At these three concentrations addition of any cations does not affect the mechanism of the growth. Only in case of a silica content of 750 ppm the addition of cations leads to a particle-particle agglomeration and therefore to higher values of M_w. Clearly, the threshold concentration at which the step-growth like particle-particle agglomeration sets in is decreased in the presence of metal cations.

As the observed particle size is very small for all measured samples no information about the particle shape can be extracted directly from the scattering curves in terms of a

formfactor. However, the correlation of the hydrodynamic radius or the radius of gyration with the weight-averaged molar mass according to Equation 2.20 gives indirect information about the particle structure. Like it was already mentioned in Chapter 3.1.1 the size-mass correlation follows a power-law for self-similar structures. Fractal-like structures are indicated by $\alpha = 1/2$ and spherical homogeneous structures are indicated by an exponent of $1/3$[89]. These are the topology based exponents which can be observed if the particles are formed via a step-growth mechanism where every particle can react with any other particle. In case of a monomer-addition growth the weight-averaged molar particle mass would describe an ensemble of monomers and growing particles if the entire silica content c_0 is used for the calculation. This would lead to a decreased exponent by a factor of 1/2.

The correlation of R_h versus M_w are shown in Figure 3.15, the measurement series in the presence of Ca^{2+}+Mg^{2+}-ions is given in the upper graph (Figure 3.15A) and the measurement series in the presence of Na^+-ions is given in the lower graph (Figure 3.15B). The mass values have been calculated based on the initial silica concentration c_0. The trends of the correlations for the two types of salts are comparable. In both types of salts two different shape sensitive exponents are observed. Silica contents of 350 −500 ppm result in a slope of 1/6 and experiments with 750 ppm SiO_2 show a slope according to an exponent $\alpha = 1/2$. As the smallest possible exponent based on the topology is 1/3 corresponding to compact spherical structures, the lower exponent of 1/6 observed below 750 ppm is only explainable by the formation of compact spherical particles with homogeneous density (most likely of spherical shape) via a monomer-addition process. The particle growth process at 750 ppm in the presence of metal cations exhibits no lag-time. Consumption of the monomers is fast and the weight-averaged molar mass is increasing beyond the time when the equilibrium concentration of the monomers is reached. No plateau value is reached for the particle size. The correlation of R_h with M_w gives an exponent of 1/2. The same exponent holds true for the correlation of R_g with M_w, which is only accessible for the experiment in the presence of Ca^{2+}+Mg^{2+} as in this case the particles have reached a sufficiently large size to detect a radius of gyration. This correlation is shown in Figure 3.16.

For the exponent of 1/2 observed at 750 ppm two explanations are possible. (i) A particle formation via monomer-addition is assumed, where we would have to multiply the observed exponent by a factor of two to get the topology based exponent.[76,77] The resulting exponent of 1 would suggest rod-like structures. However, given the state of knowledge on the formation of colloidal silica under the present conditions,[5,22] a rod-like structure seems to be very unlikely. A further argument against a rod-like structure is provided by the shape-sensitive factor $\rho = R_g/R_h$, which is represented for the experiment at 750 ppm in the presence of Ca^{2+}+Mg^{2+} in Figure 3.17A. For rod-like structures a value of $\rho \geq 2$ would be expected.[74,75] Values in Figure 3.17A are close to $\rho \sim 1.3$ which is in agreement with the value observed for unperturbed polymer chains[73] but significantly smaller than $\rho \geq 2$ expected for rod-like coils. Evaluation of D_z (and along with it of R_h) was carried out with Equation 2.17 of the manuscript. A selection of angular dependencies from the analysis at a silica content of 750 ppm is shown in Figure 3.18. All trends are linear with small slopes excluding bimodal size distributions. Aside from providing D_0,

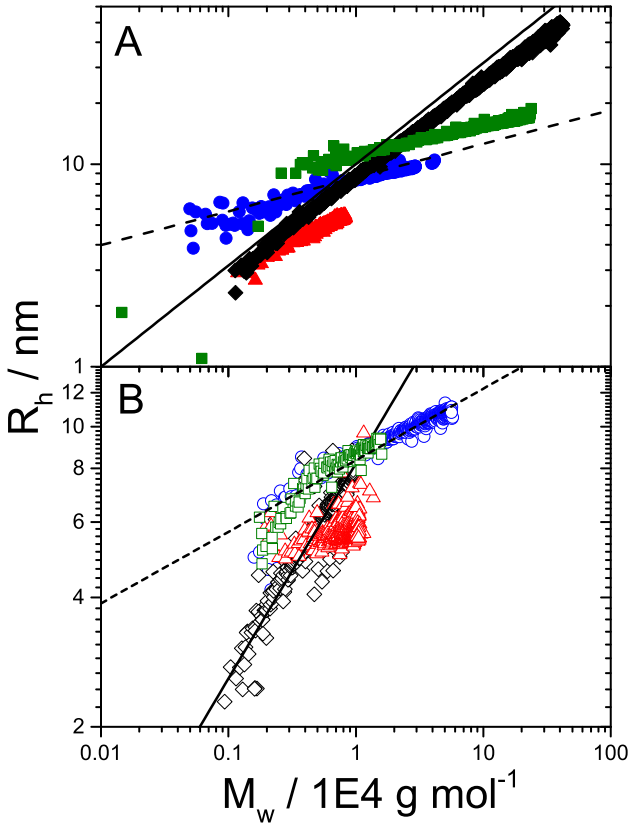

Figure 3.15.: Correlation of the hydrodynamic radius R_h and the weight-averaged molar mass M_w at pH 7 at variable silica contents: (A) in the presence of Ca^{2+}+Mg^{2+}-ions at 350 ppm (■), 400 ppm (●), 500 ppm (▲), 750 ppm (◆); (B) in the presence of Na^{+}-ions at 350 ppm (□), 400 ppm (○), 500 ppm (△), 750 ppm (◇). The solid black line indicates a slope of $1/2$ and the dashed black line represents a slope of $1/6$.

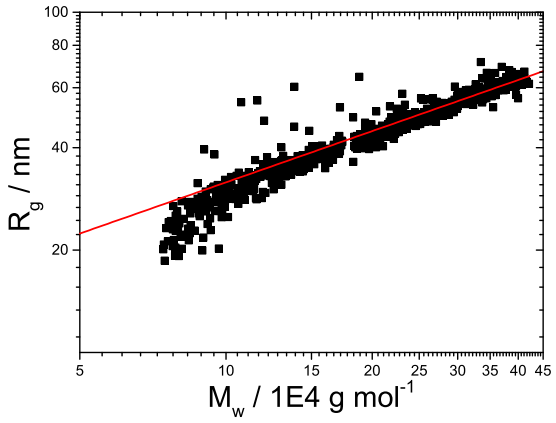

Figure 3.16.: Correlation of R_g versus M_w for the silica polymerization in the presence of Ca^{2+}+Mg^{2+} at a silica content of 750 ppm SiO_2. The red line indicates a slope of 1/2.

data evaluation according to Equation 2.17 reveals the parameter C. This dimensionless parameter shown in Figure 3.17B approaches 0.18, which is close to 0.173 predicted for unperturbed Gaussian polymer chains[71] and significantly larger than $0.033 < C < 0.044$ anticipated for rod-like structures.[91] (ii) A growth based on a particle-particle agglomeration also denoted as step-growth in polymer science is assumed, where the observed exponent can be related directly to the topology of the particles.[76,77] Hence, an exponent of 1/2 indicates fractal-like[66,89] structures, with a fractal dimension of 2. In fact a comparison with Gaussian polymer coils[66], which also have a fractal dimension of 2 and $\rho \sim 1.3$ and $C \sim 0.173$ teaches us that the explanation (ii) is appropriate. Most likely such structures are formed with the homogeneous particles generated via monomer-addition, which succeedingly react via step-growth polymerization.

These results together with the perfect correlation of the evolution of the particle mass with consumption of monomers, enable us to discriminate two concentration regimes with two mechanisms of particle growth. The particle growth at 350 ppm–500 ppm SiO_2 is characterized by a distinct lag-time during which monomers are not consumed followed by particle growth via monomer-addition. Above a concentration of 500 ppm the particles aggregate to fractal-like structures according to a step-growth process. These results are consistent with the findings for the silica polymerization in pure water, which have been already presented in Chapter 3.1.1.

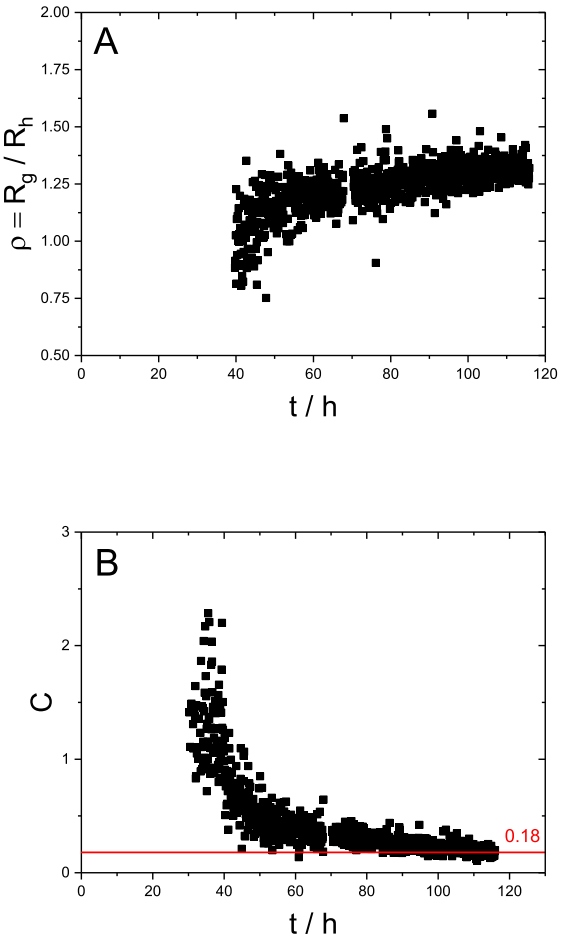

Figure 3.17.: Characteristic parameters for the sample with a silica content of 750 ppm in the presence of Ca^{2+}+Mg^{2+}. (A): Evolution of the parameter $\rho = R_g/R_h$ with time. Data correspond to those shown in the right column of Figure 3.12 and in Figure 3.16. (B): Coefficient C as a function of time calculated from the slope $m = D_0 R_g^2 C$ of the linear fits to D_z versus q^2 illustrated in Figure 3.18 for 9 examples.

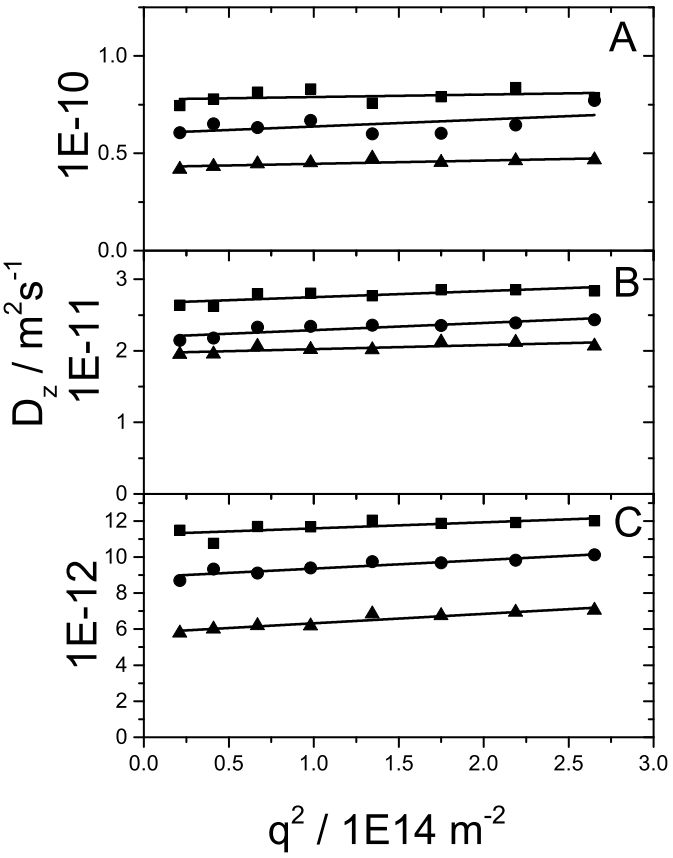

Figure 3.18.: Apparent diffusion coefficient D_z as a function of the scattering vector q^2 at different times taken from the experiment with a silica content of 750 ppm in the presence of Ca^{2+}+Mg^{2+}. Graph A: (■) t = 1.5 h, (●) t = 2.4 h, (▲) t = 5.2 h; Graph B: (■) t = 13 h, (●) t = 18 h, (▲) t = 22 h; Graph C: (■) t = 52 h, (●) t = 71 h, (▲) t = 116 h. The straight lines represent the linear fits according to Equation 2.17. A concentration dependence of D_z has been neglected.

At this point, we would like to stress a comparative representation of the evolution of the hydrodynamic radius with molecular weight for the growth processes which obey a step-growth process under all three conditions. To this end values of the molecular weight of the fractals have been calculated according to $M_w = \Delta R/K \cdot c_{part}(t)$ with $c_{part} = c_0 - c_{mon}(t)$ and $c_{mon}(t) \approx 170$ ppm the (constant) equilibrium concentration of the non-consumed monomers. Justification for this calculation of M_w is that the scattering contribution of the non-consumed monomers is negligible which implies use of the (constant) concentration of growing fractals c_0 – 170 ppm. As is demonstrated in Figure 3.19, the corresponding correlations do not only follow a power law with an exponent of 0.5 but also overlay perfectly. Such an overlay can be nicely reconciled with the fact that independent on the actual conditions, i.e. independent on whether additional salt is absent or present as Na^+ or as Ca^{2+}+Mg^{2+}, always the same fractals are formed and the same constituent building units are incorporated with the building units corresponding to the homogeneous particles formed respectively via the monomer-addition process. A variation of the size of the constituent particles when changing the conditions does not affect the resulting exponent of the power law in Equation 2.20, but it would generate a parallel shift in the log-log plot as a result of a variation of the prefactor. The coincidence of all curves is particularly interesting as this implies, that the step-growth like agglomeration sets in always with constituent particles having a size in the order of 1-3 nm.

Further support for the suggested mechanisms and morphologies is provided by the correlation of the finally measured hydrodynamic radii with the corresponding mass values, as it is done in Figure 3.20. Here, the mass values of the particles have been calculated according to Equation 2.3 with the mass concentration of the growing particles $c_{part}(t = t_{max})$ from Equation 3.1 instead of using c_0. In cases where the growth process was still going on while the final measurement was done $c_{mon}(t)$ was interpolated from the respective trend determined by the molybdenum blue method. In cases where the growth process was completed $c_{mon}(t)$ is equal to the equilibrium concentration of 170 ppm SiO_2. Figure 3.20 is a comparison of data from three measurement series: silica polymerization (i) in pure water from Chapter 3.1.1, (ii) in the presence of Ca^{2+}+Mg^{2+} and (iii) in the presence of additional Na^+. At all conditions the final values measured for silica contents below 750 ppm follow a unique trend with a slope of 1/3. Noteworthy, these are the conditions where no aggregation of particles takes place. This result confirms the existence of homogeneous particles with a uniform characteristic density like for instance cubes or spheres.

As expected, the situation is different at the later stages of the experiments with 750 ppm of silica in the presence of metal cations (black cross and black diamond in Figure 3.20). As no equilibrium values for R_h and M_w is reached under those conditions, we choose data at a later time, when the monomer consumption has reached its equilibrium value since long. At t = 50 h in the presence of Ca^{2+}+Mg^{2+} the hydrodynamic radius amounts to R_h = 26 nm and the weight-averaged molar mass is $M_w = 1.4 \cdot 10^5$ g/mol and at t = 20.7 h in the presence of additional Na_+ R_h =7.9 nm and the weight-averaged molar is $M_w = 1.29 \cdot 10^4$ g/mol to give but two examples. These data points lie far off the trend of the correlation with the exponent α = 1/3 (Figure 3.20). This can be nicely reconciled with the growth of fractal-like particles. However, if we consider the first data point of

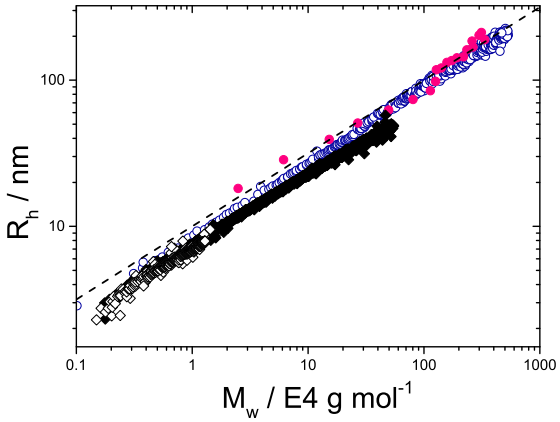

Figure 3.19.: Correlation of the hydrodynamic radius R_h with the weight-averaged molar mass $M_w = \Delta R/Kc_{part}(t)$ at the silica contents 2000 ppm in pure water (○), 3000 ppm in pure water (●), 750 ppm in the presence of Ca^{2+}+Mg^{2+} (◆) and 750 ppm in the presence of Na^+(◇). Experimental data corresponding to silica polymerization in pure water correspond to those already presented in Chapter 3.1.1 (Figure 3.1 and 3.4). The dashed line represents a slope of 1/2.

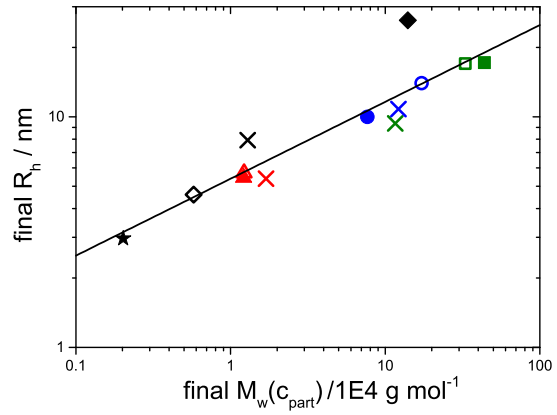

Figure 3.20.: Correlation of $R_h(t = t_{max})$ with the final values of $M_w=\Delta R/Kc_{part}(t = t_{max})$ at variable silica contents: 350 ppm (□, ■, ×), 400 ppm (○, ●, ×), 500 ppm (△, ▲, ×), 750 ppm (◇, ◆, ×), empty symbols indicate the experiments in the absence of metal cations, full symbols the experiments in the presence of Ca^{2+}+Mg^{2+} and crosses indicate the experiments in the presence of additional Na^+. The straight line represents a slope of 1/3. For the sample 750 ppm in the presence of Ca^{2+}+Mg^{2+} two data points are shown. (◆) Final size and mass value, where the aggregation has been already started. (★) Data of one of the very early measurements, where the aggregation process of this sample has not yet started.

this TR-SLS/DLS experiment the value of the hydrodynamic radius (R_h = 3 nm) and the weight-averaged molar mass ($M_w = 2.0 \cdot 10^3$ g/mol) fits perfectly to the trend based on the exponent $\alpha = 1/3$ (black star in Figure 3.20). The mass value $M_w = 2.0 \cdot 10^3$ g/mol has been calculated under the assumption that monomer concentration has already reached its equilibrium value. This is a hint that the early intermediate still refer to spherical particles formed by a monomer-addition process and thus nicely confirms that monomer-addition, which is observed for all lower silica concentrations, also takes place at the initial period of the process at a silica content of 750 ppm in the presence of metal cations. Only the rate of nucleation and growth is so fast that it is already accomplished soon after the initiation. Due to an insufficient stabilization of the spherical particles, particle-particle aggregation starts immediately and is dominating the growth process monitored by light scattering measurements. The trend in ρ presented in Figure 3.17A further confirms this aspect.

Although the final particle size as well as the lag-time slightly depend on the solution condition the general trends of the evolution of the size are comparable for all conditions under consideration i.e. in the presence of Ca^{2+}+Mg^{2+}-ions, in the presence of additional Na^+-ions and in the absence of any added salt. We thus can state that the presence of metal cations has no significant effect on the general mechanism of the silica polymerization. For all three conditions, a change from a monomer-addition mechanism generating compact particles with a homogeneous density to a particle-particle aggregation leading to fractal-like particles with the homogeneous particles as building units is observed once a certain silica content is reached. Independent on when this change of the growth mechanism takes place, homogeneous particles corresponding to building units have reached a size of $R_h \approx$ 1-3 nm. Only the concentration threshold at which the aggregation of the particles becomes dominant is shifted to lower silica concentrations, if metal cations are present. Whereas in the presence of metal cations this threshold is smaller than 750 ppm, the threshold concentration lies between 750 ppm and 2000 ppm SiO_2 in salt-free solutions.

3.3. Characteristics of the Silica Polymerization

Investigation of the silica polymerization from supersaturated aqueous solution at near neutral pH (pH 7 and pH 8) and under different salt conditions verified for the first time with direct in-situ techniques that the silica polymerization proceeds according to a 3-step process which has been inferred from indirect hints in preceding work[22,46]. The steps are (1) nucleation/initiation, (2) particle growth by addition of monomers and (3) agglomeration of the particles generated in step 2. The application of time-resolved combined dynamic and static light scattering as in-situ technique complemented by the time-resolved monitoring of the monomeric silica via the molybdenum blue method turned out to be a powerful tool to follow silica particle growth.

The phase of nucleation and/or initiation is characterized by a silica concentration dependent lag-time, which is identified by a constant scattering signal close to the scattering of the solvent and by the lack of a detectable decrease of the molybdate-reactive

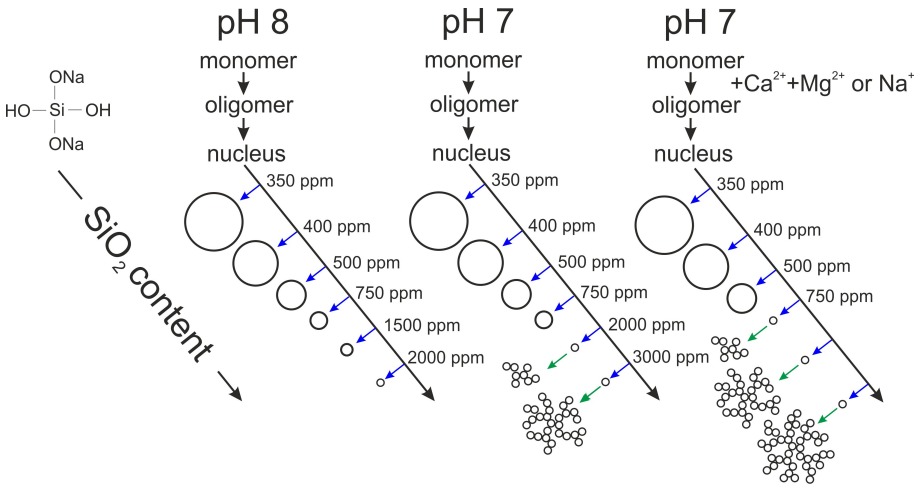

Figure 3.21.: Schematic overview of the mechanistic features of silica polymerization at variable silica contents at pH 7 and 8 and under variable salt conditions. Blue arrows denote the growth of primary particles by monomer-addition, and green arrows indicate particle-particle agglomeration.

silica. The lower the initial supersaturation is, the longer this lag-time gets. It could be observed that the lag-time is decreased in the following trend if additional Ca^{2+}+Mg^{2+} or Na^{+} at a level of 0.01 N is present, respectively τ (salt-free) > τ (Na^{+}) > τ (Ca^{2+}+Mg^{2+}).

The particles nucleated in the first step grow according to a monomer-addition mechanism where the monomers may include monomeric silicic acid and oligomers thereof. These features could unambiguously be inferred from the coincidence of disappearing molybdate-reactive “monomers” with the particle growth and from a correlation of particle size (from DLS) with particle mass (from SLS) resulting in characteristic power laws of $R_h \sim M_w^{1/6}$. Ostwald-ripening can be excluded during step 2 as this would have modified the exponent of 1/6.

Combined time-resolved light scattering enabled us to discriminate this monomer-addition process unambiguously from the third step the agglomeration of particles which sets in once the concentration of silica is large enough. It proceeds via a step-growth like particle-particle aggregation. As extracted from SLS/DLS-data, the resulting agglomerates have a fractal dimension close to 2. The onset of particle agglomeration according to this step-growth process, which in pure water at pH 8 could not be observed up to a silica content of 2000 ppm and at pH 7 was first observed at a silica content of 2000 ppm is shifted to lower values by the addition of salt. Agglomeration takes place already at 750 ppm in the presence of both types of cations Na^{+} and Ca^{2+}+Mg^{2+}. Hence an increase of the pH value stabilizes the particles due to an increase of surface charges and the presence of cations destabilizes particles with respect to particle-particle agglomeration. However, the presence of Ca^{2+}+Mg^{2+} and the presence of additional Na^{+} does not affect the fractal dimension of the growing intermediates. Even more strikingly, the presence of an additional salt does not even affect the nature of the constituting particles. Independent on whether salt is present or absent nucleation succeeded by growth

via monomer-addition leads to particles with the same critical size of a few nanometers which then agglomerate to a unique type of fractal.

The important mechanistic features of the silica polymerization under the investigated conditions are summarized in Figure 3.21 and are related to the mechanistic features given by Iler[22] (see Figure 1.3).

3.4. Verification of the 3-step mechanism - an alternative point of view

The results in Chapter 3.1 and 3.2 have confirmed that silica particles grow according to a three step mechanism characterized by a nucleation step, a monomer-addition growth to homogeneous compact particles and agglomeration of these compact particles to clusters with a fractal dimension of 2 as the third step. The agglomerates are formed above a certain threshold concentration and consists of constituting particles of the same size. The agglomeration has been deduced from the results based on the size-mass correlation and the formfactor. In the following we want to complement the mechanistic discussion of the silica particle formation by a more detailed view on the agglomeration process. Consideration of the trends of the size and the mass depending on time can help to verify an agglomeration process and to discriminate between a diffusion-limited and a reaction-limited aggregation. In addition, this data analysis with the focus on the agglomeration of the particles enables once more the confirmation of the monomer-addition mechanism in cases where no characteristics of an agglomeration can be observed.

It turned out that the concept of fractal geometry[92] provides an adequate theory to describe structures and particles, which have been formed via an aggregation of particles. The first model based on diffusion-limited aggregation (DLA) yielding fractal-like clusters was given by Witten and Sander[93] in 1981. A seed particle at the origin of a two-dimensional lattice is the initial state of their model. A second particle is occurring at some random site at a large distance from the origin. This second particle is moving via a random walk trajectory until it encounters a site adjacent to the seed. If this happens the particle is added irreversibly to the cluster. Then another particle is introduced and starts its random walk at a random distant point. It follows the random walk trajectory until it is also added to the cluster. If the moving particle reaches a boundary of the lattice it is removed and the next particle is introduced.[93] This simulation produces random ramified structures. In an off-lattice simulation, the particle can move with equal probability to any place with in steps of one particle diameter. The resulting cluster has a fractal dimension of $D \approx 1.7$ for the Euclidean dimension $d = 2$ and $D \approx 2.5$ for $d = 3$. The DLA model of Witten and Sander was an important breakthrough and can describe a broad range of phenomena.

Although, the DLA model is not able to describe aggregation processes of colloids, but it was the base of further investigations by Meakin[94] and Kolb, Botet and Jullien[95], who introduced in 1983 a diffusion-limited cluster-cluster aggregation model. Here particles as well as clusters are moving on a lattice via random walk trajectories. Contact

of these particles or clusters with each other yields a larger cluster and this larger cluster continues diffusing via random walk on the lattice.

In general, two different processes can be distinguished for the aggregation of particles (i) the diffusion-limited cluster aggregation (DLCA) and (ii) the reaction-limited cluster aggregation (RLCA). The diffusion-limited cluster aggregation is a fast process. The repulsive energy barrier is much smaller than k_BT. Therefore every collision of two particles leads to a larger cluster. On the other hand a reaction-limited process takes place, if the repulsive energy barrier equates the value of k_BT or is even higher. As many collisions are required for a successful coalescence the reaction-limited cluster aggregation (RLCA) is a slow process. From several computer simulations and also from various experimental data it is ensured, that both regimes (DLCA and RLCA) exhibit a characteristic and distinct behaviour, which yields different fractal dimensions d_f for the respective clusters. In a diffusion-limited particle-particle aggregation a fractal dimension d_f = 1.8 and in a reaction-limited particle-particle aggregation a fractal dimension of d_f = 2.1 can be found.[96]

A possibility to discriminate between these two mechanisms is to analyze the growth of the radius and the weight-averaged molar mass depending on the time. For a diffusion-limited cluster aggregation (DLCA) we should get a power law with time and for the reaction-limited cluster aggregation (RLCA) we should get an exponential growth. Hence a double logarithmic plot of the radius or the mass with time should show a linear behaviour in the diffusion-limited case and a logarithmic plot of the same values versus linear time should show a linear behaviour in the reaction-limited case.[97,98]

Figure 3.22, 3.23, 3.26 and 3.27 show the experimental data for the silica polymerization at pH 7 in the absence of additional salt ions, in the presence of Ca^{2+}+Mg^{2+}-ions and in the presence of additional Na^{+}-ions in terms of the hydrodynamic radius and the weight-averaged molar mass as a function of time in two scaling formats: (i) as a semi-logarithmic plot, testing for the reaction-limited growth and (ii) as a double logarithmic plot, testing for a diffusion-limited growth. In case of the two lowest silica contents 350 and 400 ppm a linear trend of the mass with time in none of the different conditions is observable. Based on the findings in Chapters 3.1 and 3.2 we can state, that for these silica contents a pure monomer-addition mechanism occurs independent on the presence of additional electrolytes. Furthermore it can be stated, that for all investigated conditions a linear trend is only given in double logarithmic scale. Therefore an aggregation of silica particles most likely takes place via a DLCA-mechanism. The hydrodynamic radius and weight-averaged molar mass give in principle the same results. Only in case of a silica content of 750 ppm in pure water a linear trend is observable for the weight-averaged molar mass but not for the hydrodynamic radius.

We observed a particle-particle aggregation in case of silica polymerization in pure water at an initial silica content of 2000 ppm and higher. This fact was mainly deduced from the results of the size-mass correlation and of the formfactor. Additionally the double logarithmic plot of the hydrodynamic radius, the radius of gyration and of the weight-averaged molar mass exhibits a linear dependency with time (right column of Figure 3.22 and Figure 3.23) and corroborates occurrence of a particle-particle aggregation. Furthermore it suggests an aggregation which appears via diffusion-limited growth. The

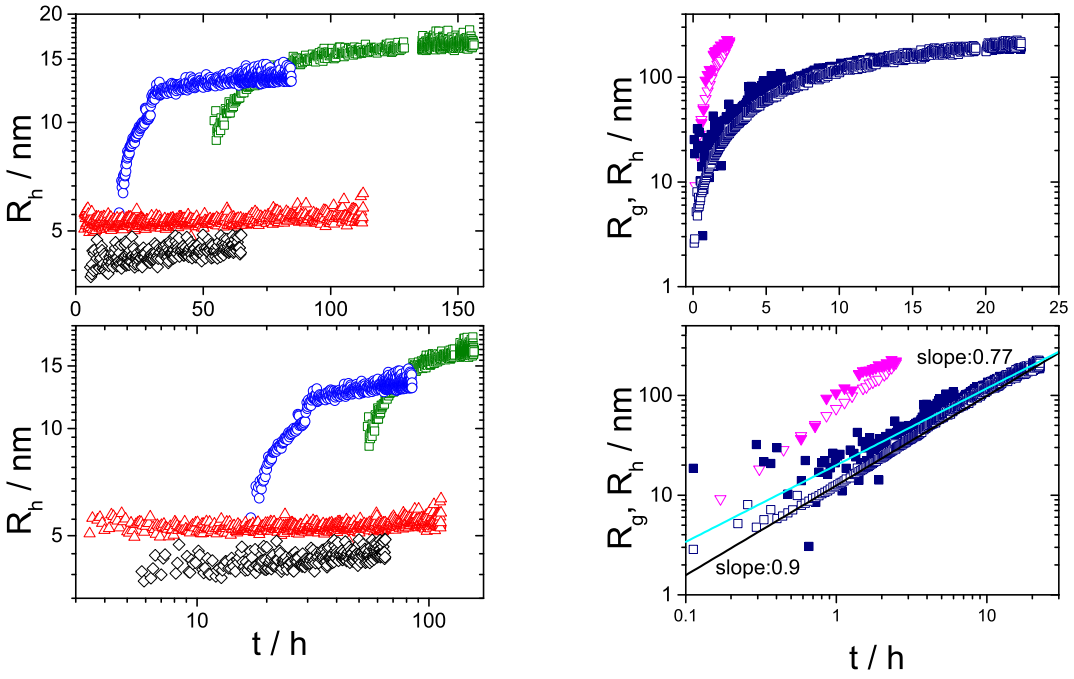

Figure 3.22.: Radius of the silica particles formed in the absence of electrolytes at variable silica content. The upper row shows the semi-logarithmic plot (linear trend would indicate RLCA) and the lower row shows the double logarithmic plot (linear trend would indicate DLCA) of the respective experimental data. **Left**: 350 ppm (□), 400 ppm (○), 500 ppm (△), 750 ppm (◇). **Right**: full symbols indicate the radius of gyration and empty symbols indicate the hydrodynamic radius; 2000 ppm (■, □) and 3000 ppm (▼, ▽). The slopes of the straight lines are indicated in the graphs.

most explicit trend is obvious for the hydrodynamic radius at a silica content of 2000 ppm, as for this concentration experimental data is available over two decades. The hydrodynamic radius follows a slope of 0.9 up to t = 3 h. At this point the curve shows a small bending which yields to a slightly smaller slope of 0.77. In general from the exponent of the particle size the fractal dimension d_f of the particles can be derived corresponding to $R \propto t^{1/d_f}$. The evaluated fractal dimension of d_f = 1.1 – 1.3 is smaller than the expected value for a diffusion-limited process, which is d_f = 1.8, although a direct calculation based on a formfactor at $t \sim$ 19 h (see Figure 3.7) corresponding to $I(q) \propto q^{-d_f}$ gives a value of d_f = 1.87 for high q and is therefore in line with the assumption of a diffusion-limited aggregation. The weight-averaged molar mass at the silica contents 2000 ppm and 3000 ppm also shows linear dependencies on time in a double logarithmic plot, which suggests a DLCA-mechanism. Only the slope is with 1.75 higher than in case

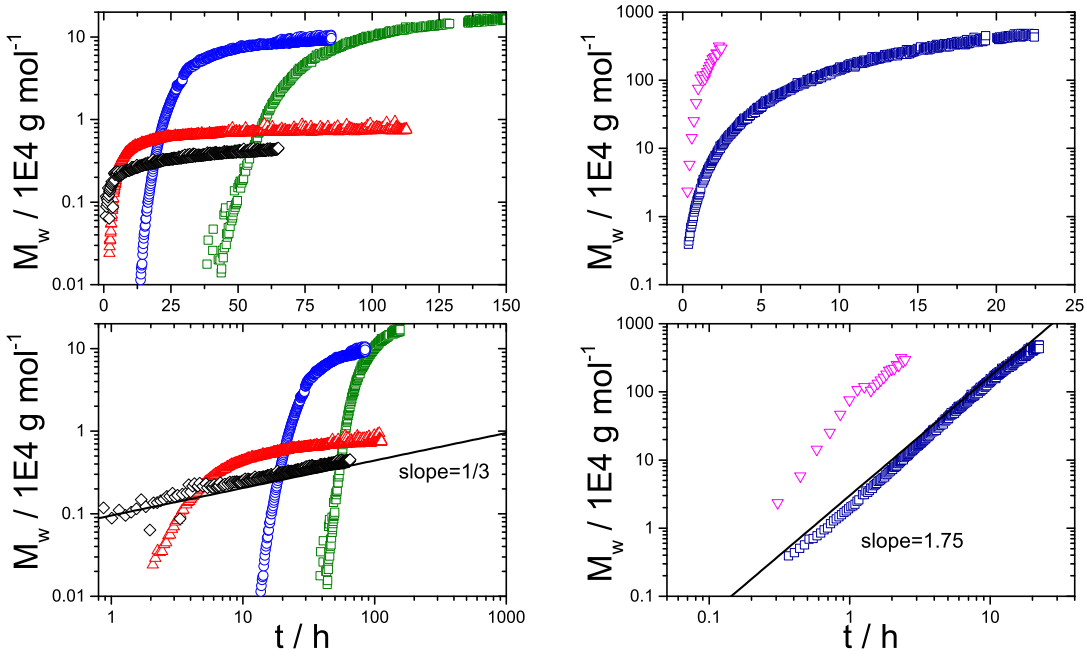

Figure 3.23.: Weight-averaged molar mass of the silica particles formed in the absence of additional electrolytes at variable silica content. The upper row shows the semi-logarithmic plot (linear trend would indicate RLCA) and the lower row shows the double logarithmic plot (linear trend would indicate DLCA) of the respective experimental data. **Left**: 350 ppm (□), 400 ppm (○), 500 ppm (△), 750 ppm (◇). **Right**: 2000 ppm (□) and 3000 ppm (▽). The slopes of the straight lines are indicated in the graphs.

of $R_g \sim t^{1/d_f}$. However, as we are considering the weight-averaged molar mass a value for d_f cannot directly be derived from the slope.

From the results of Chapter 3.1.1 it has been inferred that initial silica concentrations of 350 ppm - 750 ppm in pure water lead to compact spherical particles formed via a monomer-addition mechanism. Hence, probing for an aggregation mechanism by plotting the size or the mass versus the time in a semi-logarithmic and a logarithmic scale should give no linear dependency. At the silica contents of 350 ppm and 400 ppm, no linear trend in size and mass is observed, thereby excluding any particle-particle aggregation process for these samples only at 750 ppm and at 500 ppm SiO_2 the evolution of the mass shows a linear dependency with a slope of 1/3. This may be a hint for an aggregation process. However, the constant radius and also the scaling behaviour of the final size and mass values presented in Figure 3.3 contradicts such an aggregation.

At this point we want to show a more detailed analysis of the samples with a sil-

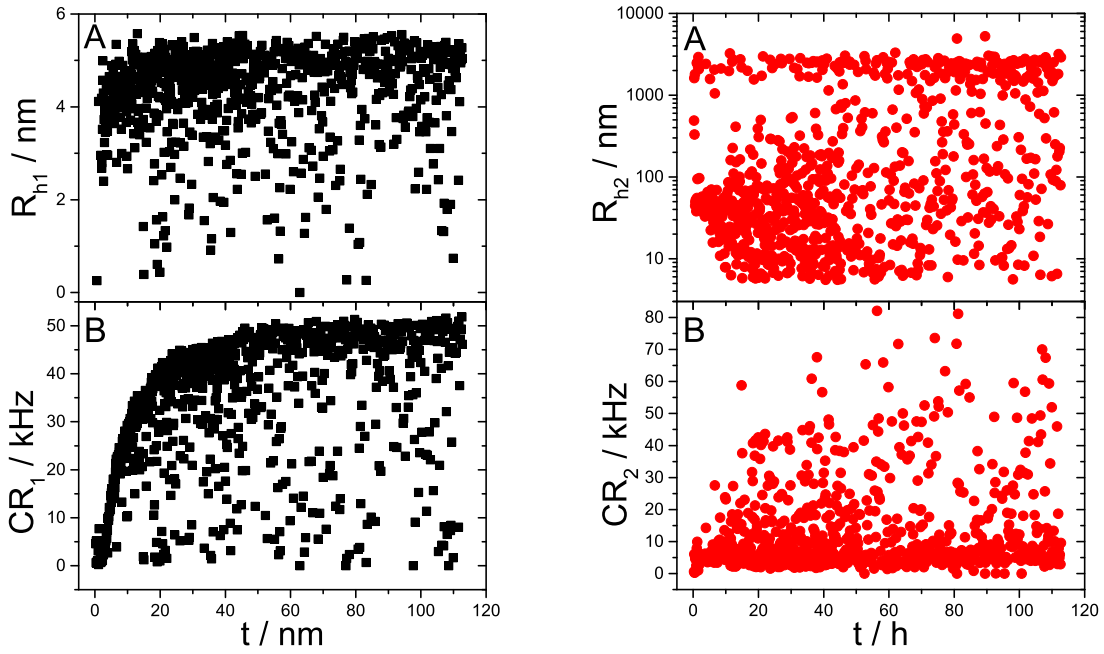

Figure 3.24.: Results of the bi-exponential fit of the correlation-functions at a scattering angle of 20° and at a silica content of 500 ppm in pure water. **Left**: Hydrodynamic radius R_{h1} (A) and the corresponding count rate CR_1 (B) of particle species 1 (■). **Right**: Hydrodynamic radius R_{h2} (A) and the corresponding count rate CR_2 (B) of particle species 2 (●).

ica content of 500 ppm and 750 ppm under salt-free conditions. In these two cases the hydrodynamic radius increases during a short period of time and then remains constant within the experimental uncertainty while the weight-averaged molar mass is still slightly increasing. In order to proof the reliability of the cumulant fit, which has been used to determine the hydrodynamic radius, the corresponding correlation-functions at different times of these two measurements are shown in Figure A.1, in the Appendix. An increasing slope of the correlation-function with proceeding time is not observed, solely the intercept of the correlation-function, which is a magnitude for the signal-to-noise-ratio is clearly increasing. This follows from the increasing scattering intensity with time. Both give a hint for an increasing number of particles with the same size and contradicts an aggregation of particles.

In order to investigate the correlation-functions in more detail, a bi-exponential analysis has been performed. The fits are done with the correlation-functions detected at

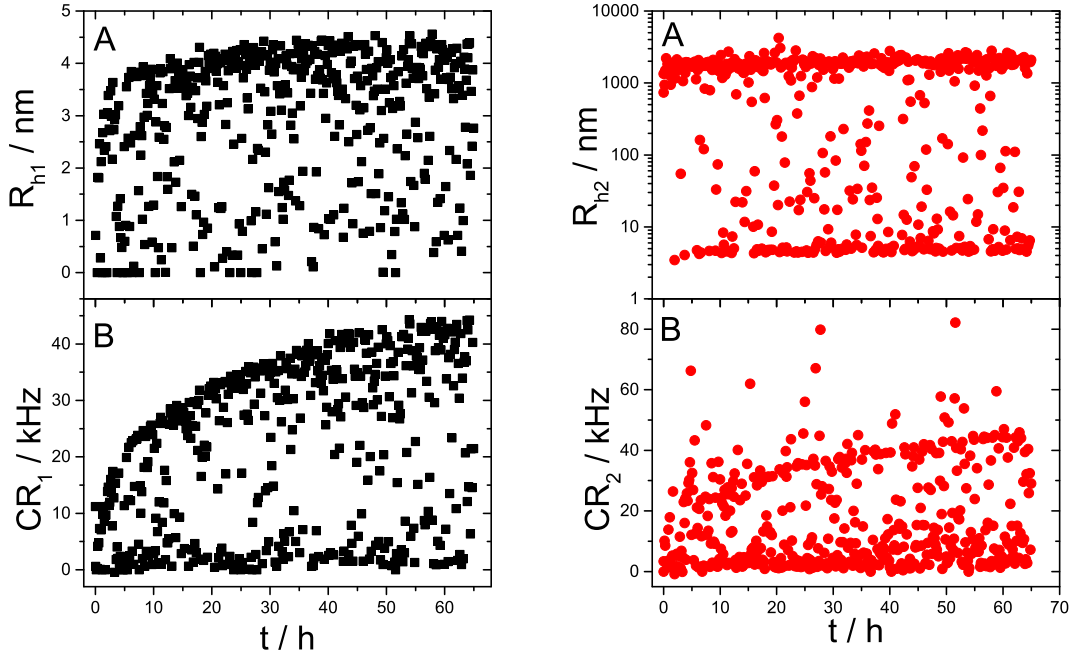

Figure 3.25.: Results of the bi-exponential fit of the correlation-functions at the scattering of 20° and at a silica content of 750 ppm in pure water. **Left**: Hydrodynamic radius R_{h1} (A) and the corresponding count rate CR_1 (B) of particle species 1 (■). **Right**: Hydrodynamic radius R_{h2} (A) and the corresponding count rate CR_2 (B) of particle species 2 (●).

a scattering angle of 20° and the fitting function is given by

$$g_{fit}(\tau) = A + \gamma_1 \cdot exp(-\frac{\tau}{\Gamma_1}) + \gamma_2 \cdot exp(-\frac{\tau}{\Gamma_2}). \tag{3.2}$$

The parameter A describes the intercept of the correlation-function, γ_1 and γ_2 are the weighting factors of the two species. The time-constant Γ_i describes the diffusion of the respective species and is proportional to the inverse diffusion coefficient D_i. The diffusion coefficient D_i of the particle species i is used to calculate the corresponding hydrodynamic radius R_{hi} via the Stokes-Einstein equation (see Equation 2.18). The overall count rate in kHz of the solute measured at an angle of 20° is distributed on the two species i=1 and 2 according to the weighting factors γ_i. This yields two separate count rates CR_i corresponding to the scattering intensity stemming from the respective particle species. Figure 3.24 and Figure 3.25 show the characteristics of the two identified species as a function of time in terms of the hydrodynamic radius R_{hi} and the count rate CR_i for the experiments at 500 and 750 ppm SiO_2 in pure water.

The values of R_h and CR are noisy in general due to the very small particle size and the low concentration. Nevertheless two different particle species can be distinguished. The fits suggest small particles with a size of $R_{h1} = 5 - 5.5$ nm at 500 ppm and $R_{h1} = 4 - 4.5$ nm at 750 ppm with an increase of the particle size only being observed for a very short period of time (up to $t \sim 10$ h in both cases). Beyond these times only a slight increase in the intensity can be observed. The evaluation by means of the bi-exponential fit shows that the small species determined from the bi-exponential fit corresponds to the particles determined via the cumulant fit. Multifolds of the particles of size 4-5 nm corresponding to aggregates are, if at all, buried in a slight increase of R_{hi} of 5% during the final 35 hours. In addition the fits suggest particles with a size fluctuating between 10 and 1000 nm (500 ppm) and around ~ 1000 nm (750 ppm) as a second species. The corresponding intensities of these big particles is quite low and on a constant level. Therefore we conclude that these values correspond to impurities or dust in the sample but not to large agglomerates of silica.

Neglect of this fraction of big particles leads to three different scenarios in order to explain the experimentally observed generation of the particle fraction with the size around 4-5 nm at 500 and 750 ppm SiO_2. The first scenario is characterized by a very large nucleation rate. In this case the amount of monomers available to a growth by monomer-addition would be drastically decreased, as in a short time most of the monomers would be transferred into nuclei. However, this would lead to a constant size and weight-averaged molar mass of the particles soon after nucleation. A second scenario is given by a fast period of nucleation and growth via monomer-addition overlaid and followed by a period of slight particle-particle aggregation which generates small clusters of only two or three particles. In this scenario, we should have observed an increasing size with decreasing number of clusters. Within experimental uncertainty this was not the case. In line with this, aggregates composed of primary particles (with a radius around 4-5 nm) could not be detected by applying a bi-exponential fit to the correlation-functions from DLS. Hence, a significant aggregation process can be excluded for the salt-free experiments at 500 and 750 ppm SiO_2. In light of the fact that the z-average of $1/R_h$ is hardly affected while the signal CR_1 and the mass M_w in Figure 3.1 is slightly increasing we attribute this final increase of CR_1 and M_w and this describes the third scenario rather to an increase of the number of particles during time. Whereas the fraction of monomers which are incorporated into particles by growth is very low, nucleation/initiation extends over the entire experimental time and increases the number of particles in the solution, which leads to increasing weight-averaged mass values. It is this last scenario which agrees best with the experimental data. After a fast nucleation phase, which transfers most of the available monomers to nuclei, the mass keeps increasing as still nucleation and with that the formation of particles with the same size occurs. The particle size in terms of R_h (as z-averaged $1/R_h$) remains constant (or increases only slightly) within experimental uncertainty, but the particle mass keeps increasing as the number of particles is further increasing and slightly growing.

The measurement series in the presence of Ca^{2+}+Mg^{2+}-ions and in the presence of additional Na^+-ions are discussed as follows. For these two measurement series we can find a uniform result for the linear dependence of the size and the mass with time. Silica

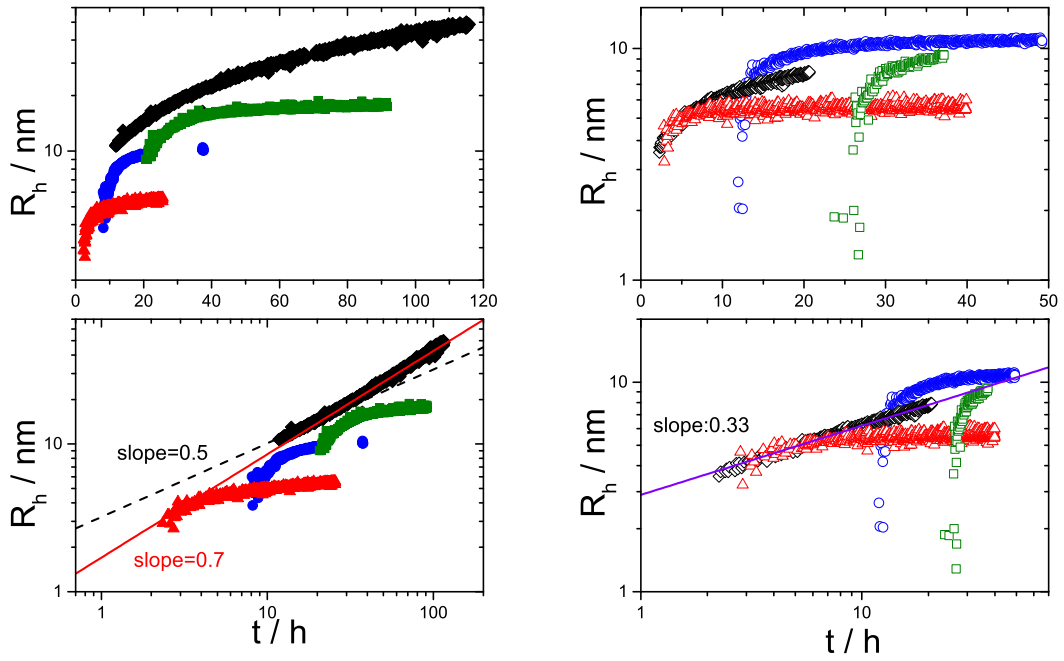

Figure 3.26.: Radius of the silica particles formed in the presence of additional electrolytes at variable initial silica contents. The upper row shows the semi-logarithmic plot (linear trend would indicate RLCA) and the lower row shows the double logarithmic plot (linear trend would indicate DLCA) of the respective experimental data. **Left**: Silica polymerization in the presence of Ca^{2+}+Mg^{2+}-ions: 350 ppm (■), 400 ppm (●), 500 ppm (▲), 750 ppm (◆). **Right**: Silica polymerization in the presence of additional Na^{+}-ions: 350 ppm (□), 400 ppm (○), 500 ppm (△), 750 ppm (◇). The slopes of the straight lines are indicated in the graphs.

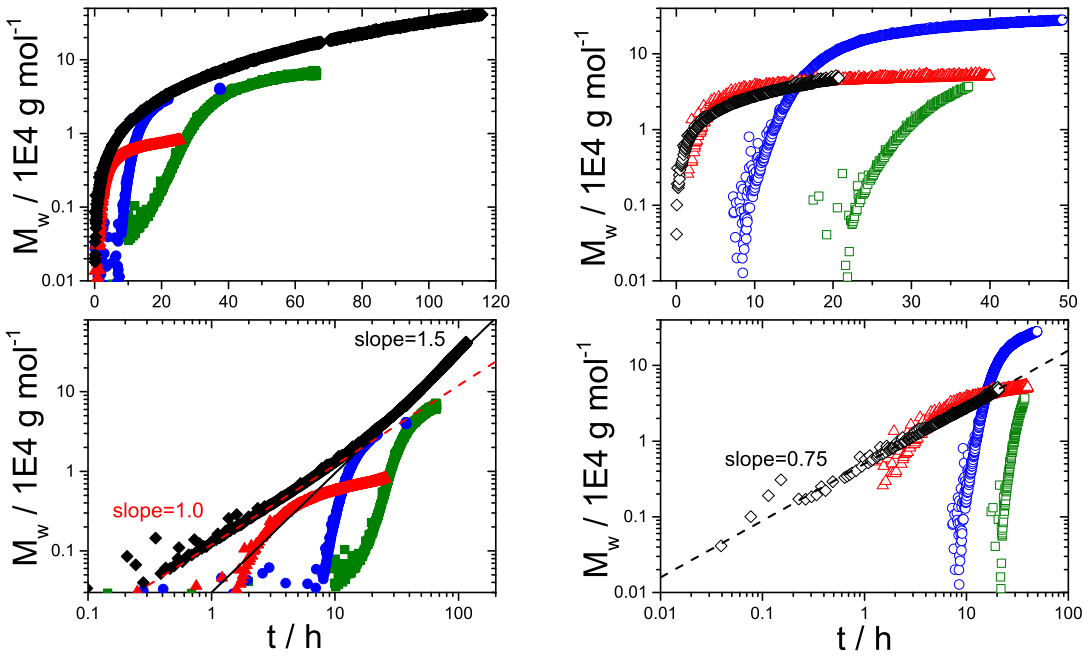

Figure 3.27.: Weight-averaged molar mass of the silica particles formed in the presence of additional electrolytes at variable initial silica contents. The upper row shows the semi-logarithmic plot (linear trend would indicate RLCA) and the lower row shows the double logarithmic plot (linear trend would indicate DLCA) of the respective experimental data. **Left**: Weight-averaged molar mass of the particles formed in the presence of Ca^{2+}+Mg^{2+}-ions: 350 ppm (■), 400 ppm (●), 500 ppm (▲), 750 ppm (◆). **Right**: Weight-averaged molar mass of the particles formed in the presence of additional Na^{+}-ions: 350 ppm (□), 400 ppm (○), 500 ppm (△), 750 ppm (◇). The slopes of the straight lines are indicated in the graphs.

contents of 500 ppm and lower exhibit no linear dependency in size and mass, independent of the type of plot, semi-logarithmic or double logarithmic. However, the sample with a silica content of 750 ppm in the presence of metal cations shows a linear trend in size and mass in a double logarithmic plot, which corresponds to a DLCA-mechanism. From the evaluation of the slope of the linear trend in size with t we determine a fractal dimension of d_f = 1.4 at 750 ppm in the presence of Ca^{2+}+Mg^{2+}. This is lower than the expected one of a cluster formed by DLCA. Unfortunately, a formfactor is not available, as a size of at least $R_g \sim 100$ nm is needed to get a significant formfactor. This holds also for the particles formed at 750 ppm in the presence of additional Na^+. Here, the fractal dimension is with d_f = 3.0 very high and contradicts the assumption of a diffusion-limited aggregation.

We can conclude that in the absence of metal cations and at pH = 7 exclusively compact particles via a monomer-addition mechanism are formed if the initial silica concentration amounts to 400 ppm and lower. At 750 ppm and 500 ppm a constant size and a slightly increasing mass is observed. An evaluation with a bi-exponential fit of the corresponding correlation-functions excluded the existence of any aggregated species. We therefore assume that nucleation occurs over a long period of time and generates more particles of the same size for these two concentrations, which yields an increasing mass, but a constant radius. The growth rate for the addition of monomers to the particles has to be very small, otherwise we would observe an increasing size. Hence, the nucleation forms particles, which have nearly the final particle size. The presence of metal cations does not change the mechanism of particle formation in the lower concentration regime. Only the threshold concentration which marks the start of the aggregation of the particles formed via the monomer-addition mechanism is shifted below 750 ppm SiO_2 (see Chapter 3.2). Compact particles via a monomer-addition mechanism are formed at silica contents of 350 −500 ppm. At 750 ppm in the presence of Ca^{2+}+Mg^{2+}-ions as well as in the presence of additional Na^+ particles are generated via a step-growth like particle-particle aggregation which follows diffusion-limited reaction.

3.5. Kinetic Modelling

3.5.1. Nucleation Growth Model (NG-Model)

Static light scattering provides the temporal evolution of the weight-averaged molar mass M_w, which is proportional to the total intensity of forward scattered light. This weight-averaged molar mass includes always information about all solute species in the solution, including growing particles or clusters as well as the monomer species. Therefore the evolution of the weight-averaged molar mass is suitable to be interpreted by kinetic models.

As the investigations with silica in aqueous solution have revealed as an important step a growth behaviour with characteristics of a monomer-addition growth, the first kinetic model which will be applied to experimental data recorded at pH 7 in the absence of additional electrolytes is a simple nucleation-growth model with 3 fundamental reac-

tions. In the following this model will always be denoted as “NG-model”. It is based on a publication of Tsapatsis et al.[99].

In a first reaction the reactive monomer B is formed from a precursor A.

$$A \xrightarrow{k_p} B \tag{3.3}$$

The second reaction describes the nucleation or initiation, which turns the monomer into a growing particle C. As the nucleation and the size of nuclei depend on the degree of supersaturation this step can only be a crude approximation to reality in case nucleation proceeds according to classical nucleation theory.

$$B \xrightarrow{k_n} C_1 \tag{3.4}$$

Particles C_i with a degree of polymerization i can grow by addition of monomer B.

$$B + C_i \xrightarrow{k_e} C_{i+1} \quad (i = 1, 2, ...) \tag{3.5}$$

The last reaction, like the nucleation step, implies a considerable simplification as the addition of monomers is described by a single reaction constant, which is independent of the degree of polymerization of the growing particles. Hence, does not take into account the increasing number of reaction sites of growing particles.

The change in the concentration of growing particles C_i can be described by the following master equation

$$\frac{dC_i}{dt} = k_n[B]\delta_{i1} - k_e[B][C_i] + k_e[B][C_{i-1}](1 - \delta_{i1}) \tag{3.6}$$

with k_n the rate constant of the nucleation, k_e the rate constant of the monomer-addition, $[B]$ the concentration of the monomers in mol/l , $[C_i]$ the concentration of the growing particles with a degree of polymerization i in mol/l and δ_{i1} the Kronecker delta.

The weight-averaged molar mass is proportional to the second moment of the particle mass distribution, with the kth moment of a distribution in general defined as

$$[C]^{(k)} = \sum_i i^k [C_i] \tag{3.7}$$

In order to get the moments for the particle mass distribution for the NG-model we have to start with the first derivatives of these moments. The first derivatives of the moments in Equation 3.7 can be calculated by using Equation 3.6.

$$\frac{d[C]^{(k)}}{dt} = k_n[B] + k_e[B] \sum_{j=0}^{k-1} \binom{k}{j} [C]^j \tag{3.8}$$

The first three moments are then given respectively as:

$$\frac{d[C]^{(0)}}{dt} = k_n[B] \tag{3.9}$$

$$\frac{d[C]^{(1)}}{dt} = k_n[B] + k_e[B][C]^{(0)} \tag{3.10}$$

$$\frac{d[C]^{(2)}}{dt} = k_n[B] + k_e[B][C]^{(0)} + 2k_e[B][C]^{(1)} \tag{3.11}$$

Conservation of mass is given by the sum of the concentrations of the precursor A, the monomer B and the monomer incorporated into the growing particles C_i. The latter one can be described by the first moment of the particle ensemble.

$$[A]_{t=0} = [A] + [B] + [C]^{(1)} \tag{3.12}$$

As the total amount of solute is equal to $[A]_{t=0}$, which is time-independent, one can write with Equation 3.12 in Equation 3.9

$$\frac{1}{k_n}\frac{d^2[C]^{(0)}}{dt^2} = -\frac{d[A]}{dt} - \frac{d[C]^{(1)}}{dt} \tag{3.13}$$

The reaction of the precursor to a reactive monomer is given by a simple exponential decay.

$$\frac{d[A]}{dt} = -k_p[A] \quad \text{with} \quad [A] = [A]_{t=0}\, \mathrm{e}^{-k_p t} \tag{3.14}$$

By using Equations 3.9, 3.10, 3.13 and 3.14 a general expression for the second time derivative of the zeroth moment is given.

$$\frac{d^2[C]^{(0)}}{dt^2} = [A]_{t=0}\, k_p k_n\, \mathrm{e}^{-k_p t} - k_n\frac{d[C]^{(0)}}{dt} - k_e\frac{[C]^{(0)}}{dt}[C]^{(0)} \tag{3.15}$$

The zeroth moment of the ensemble of all C_i can be obtained by a numerical solution of Equation 3.15. The second moment is now readily available via a numerical integration of Equation 3.11 corresponding to

$$[C]^{(2)}(t) = [C]^{(2)}_{t=0} + \int_0^t [B][k_n + 2k_e[\frac{1}{2}[C]^{(0)}(t) + ([A]_{t=0} - [A](t) - [B](t))]]dt \tag{3.16}$$

where $[C]^{(1)}$ has been replaced by Equation 3.12 and where $[C]^{(0)}$ stems from the numerical solution of Equation 3.15. With the assumption that at time t=0 no growing particles C_i are present in the solution, it is $[C]^{(0)}_{t=0} = [C]^{(1)}_{t=0} = [C]^{(2)}_{t=0} = 0$. Finally, the weight-averaged molar mass is defined as

$$M_w(t) = \frac{M_0}{[A]_{t=0}}([A](t) + [B](t) + [C]^{(2)}(t)), \tag{3.17}$$

getting accessible with $[C]^{(0)}_{t=0} = 0$ in Equation 3.16 and in Equation 3.17. In Equation 3.17 the molar mass of the monomeric unit M_0 has been adopted to the mass of one SiO_2 unit, which amounts to 60.1 g/mol.

Numerical calculations were performed by means of the in Matlab software implemented ordinary differential equation solver ode45. The integration of the second moment was done by the trapezoidal method. For the fitting process of the experimental data the "fminsearch" optimization command was chosen, which uses the simplex search method of Lagarias et al.[100] The NG-model does not take into account a equilibrium concentration of the monomers. In order to fit the model results in the same concentration range as the experimental data, the initial monomer concentration for the fitting process has been chosen as:

$$[A]_{t=0} = \frac{c_0}{M_0} - \frac{c_{mon}(t=\infty)}{M_0} \tag{3.18}$$

where c_0 is the experimentally used monomer concentration and $c_{mon}(t=\infty)$ is the equilibrium concentration.

The fits have been performed in terms of the weight-averaged molar mass as well as in terms of the decay of the monomeric silica. The results are summarized in Figure 3.28 and 3.29. The obtained model parameters are shown in Table 3.2, where k_p, k_n, k_e and χ^2 is the rate constant of the precursor reaction, the rate constant of the nucleation, the rate constant of the monomer addition and the averaged squared residual, respectively. The averaged squared residual describes the deviation of the simulated data from the experimentally obtained trends with N the number of data points, $M_{w,exp}$ the experimentally obtained molar mass and $M_{w,fit}$ the molar mass obtained by the model calculations, it is defined as

$$\chi^2 = \frac{1}{N}\sum_{i=1}^{N}\frac{(M_{w,exp} - M_{w,fit})^2}{M_{w,exp}}. \tag{3.19}$$

The simulated data follow the experimental trends at pH 7 under salt-free conditions in a satisfactory way in case of silica contents 350 ppm and 400 ppm. This is valid for the weight-averaged molar mass and the consumption of the monomeric silica. At silica contents of 500 and 750 ppm, the NG-model performs poorer (see Figure 3.29). Rate constants k_p and k_n had to be drastically increased yet without being able to reach the proper plateau values of M_w. As has been inferred from the data of our kinetic experiments, nucleation plays an increasingly dominating role. This is also reflected by the increasing rate of nucleation with increasing initial silica content. The rate constant of the growth reaction lie in the same order of magnitude for the two lowest silica contents and increases only about two orders for the highest silica concentration. However, the rate constant of the precursor reaction varies over eleven orders of magnitude with increasing silica concentration, this is physically not explainable. Very likely, it is the dominating role of nucleation that makes our NG-model less appropriate with increasing silica content because it cannot describe in adequate detail the induction period, which turns out to be an interplay of the precursor reaction more complicated than that described in Equation 3.3 and of the nucleation being highly complex on its own if appropriately described in a kinetic model.[56]

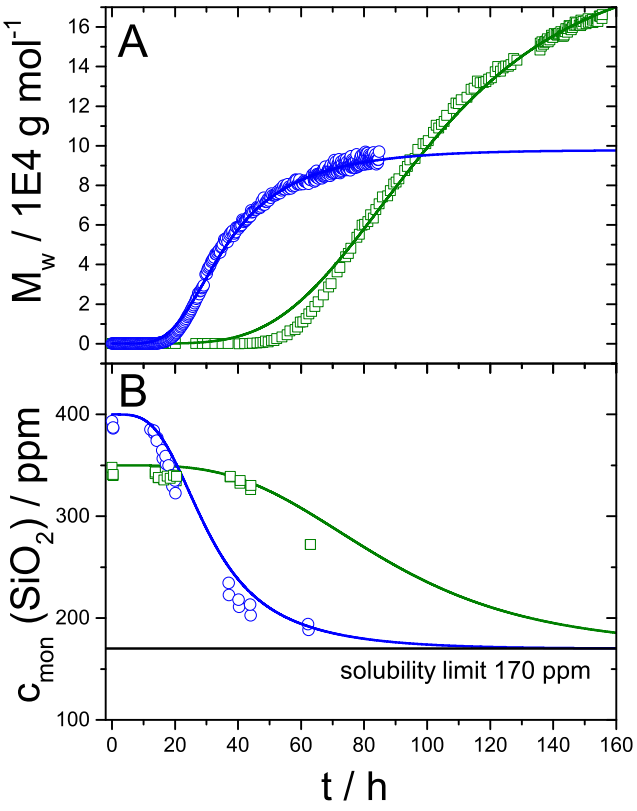

Figure 3.28.: Comparison of the experimental results with the corresponding fits with the NG-model in terms of the weight-averaged molar mass (A) and in terms of the decay of the monomeric silica for silica contents 350 ppm (□) and 400 ppm (○). The corresponding model fits are indicated by the continuous lines.

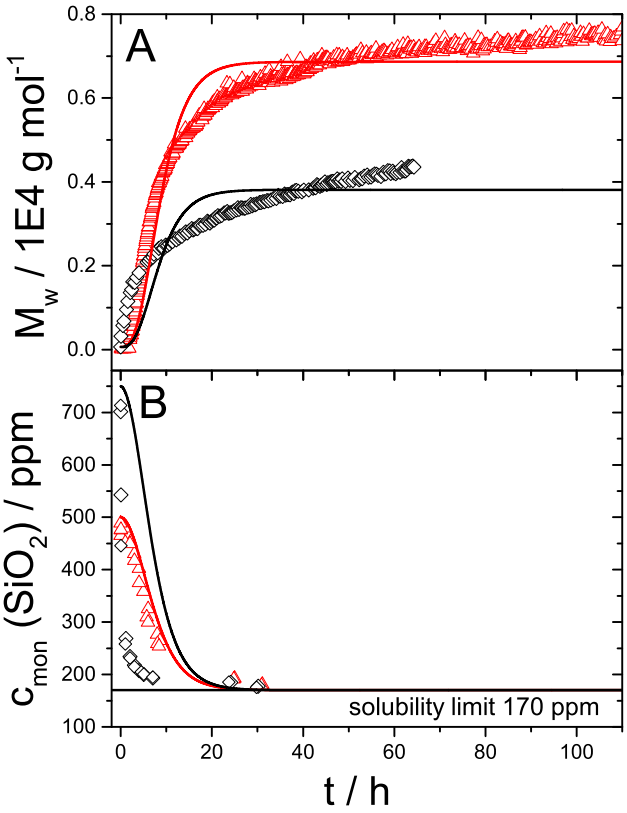

Figure 3.29.: Comparison of the experimental results with the corresponding fits with the NG-model in terms of the weight-averaged molar mass (A) and in terms of the decay of the monomeric silica for silica contents 500 ppm (△) and 750 ppm (◇). The corresponding model fits are indicated by the continuous lines.

Table 3.2.: Model parameters obtained by the fits with the NG-model to data recorded in the absence of additional electrolytes and at pH 7. The value k_p is the rate constant for the precursor reaction, k_n for the nucleation and k_e for the growth reaction in Equations 3.3-3.5. χ^2 denotes the residuals according to Equation 3.19.

	$c_{0,\,exp}$/ [ppm]	$[A]_0$/ [mol L^{-1}]	k_p/ [h^{-1}]	k_n/ [h^{-1}]	k_e/ [L (mol h)$^{-1}$]	χ^2 [g mol^{-1}]
salt-free	350	3.0E-3	2.05E-2	9.04E6	3.56E4	1.29E4
	400	3.8E-3	4.39E-2	6.45E-5	5.00E4	8.96E2
	500	5.5E-3	2.67E8	1.49E-3	3.86E3	6.05E1
	750	9.7E-3	1.35E9	2.83E-3	1.24E3	1.08E2

3.5.2. Variations of the NG-Model

Beside the reaction scheme of the NG-model introduced in Chapter 3.5.1 four additional routes have been applied to fit the experimental trend of M_w versus time. The variations of the NG-model are summarized in Table 3.3. With these alternative routes of the NG-model the influence of the nature of the reactive monomer (A and/or B) and the influence of an equilibrium for the precursor reaction is verified.

Table 3.3.: Overview on the applied variations of the NG-model

monomer	only B **NG**	only A **NG-A**	A and B **NG-A+B**
irreversible precursor formation	$A \xrightarrow{k_p} B$ $B \xrightarrow{k_n} C_i$ $B + C_i \xrightarrow{k_e} C_{i+1}$	$A \xrightarrow{k_p} B$ $B \xrightarrow{k_n} C_i$ $A + C_i \xrightarrow{k_e} C_{i+1}$	$A \xrightarrow{k_p} B$ $B \xrightarrow{k_n} C_i$ $A + C_i \xrightarrow{k_e} C_{i+1}$ $B + C_i \xrightarrow{k_e} C_{i+1}$
monomer	only B **NG-equ-B**	only A **NG-equ-A**	
precursor equilibrium	$A \underset{k_{-p}}{\overset{k_p}{\rightleftharpoons}} B$ $B \xrightarrow{k_n} C_i$ $B + C_i \xrightarrow{k_e} C_{i+1}$	$A \underset{k_{-p}}{\overset{k_p}{\rightleftharpoons}} B$ $B \xrightarrow{k_n} C_i$ $A + C_i \xrightarrow{k_e} C_{i+1}$	

As an example the experiment at pH = 7 in the absence of additional salt with an

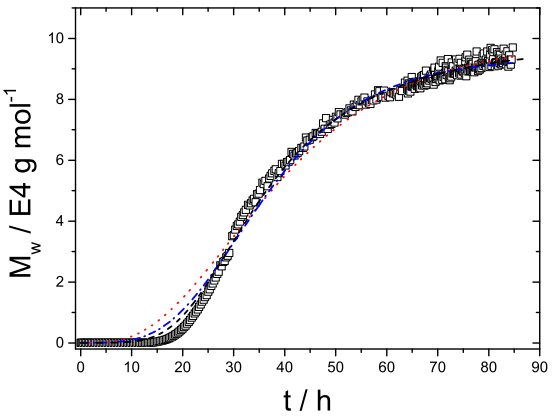

Figure 3.30.: Comparison of the evolution of M_w at an initial silica content of 400 ppm (□) at pH 7 in pure water with different model fits: (– – –) NG-model (overlays with NG-equ-B), (···) NG-A (overlays with N-equ-A), (–·–) NG-A+B.

Table 3.4.: Model parameters obtained from the optimization process for all variations of the NG-model. The parameters k_p, $k_{p,back}$, k_n, k_e and χ^2 correspond to the rate constant of the precursor reaction, the precursor back-reaction, the nucleation, the growth step and the residuals respectively.

	k_p / h^{-1}	$k_{p,back}$ / h^{-1}	k_n / h^{-1}	k_e / L (mol h)$^{-1}$	χ^2
NG	4.39E-2		6.45E-5	5.00E4	8.96E2
NG-equ-B	4.39E-2	7.03E-10	6.45E-5	5.00E4	8.92E2
NG-A	4.31E-2		7.47E-21	2.98E12	1.12E4
NG-equ-A	5.64E-2	5.14E-8	7.77E-21	3.94E12	1.12E4
NG-A+B	5.09E-2		6.06E-5	2.17E4	3.19E3

initial silica content of 400 ppm has been used. As it is illustrated by Table 3.3 and Figure 3.30 none of the variations of the original NG-model improves the fit to the experimental data. Under the assumption that A acts as a monomer in the monomer-addition growth (NG-A), the fit is not able to follow adequately the initial increase of the weight-averaged molar mass. If both species A and B are considered as a possible monomer (NG-A+B) the residuals are reduced in comparison to NG-A, but in comparison to the original NG-model NG-A+B agrees less well with the experimental curve. Assumption of an equilibrium for the precursor reaction (NG-equ-A, NG-equ-B) has no positive effect on the fit. In fact, the optimization process leads to an accurate overlay of the fits of NG and NG-equ-B on the one hand and NG-A and NG-equ-A on the other hand. The model parameters and the corresponding residuals from the optimization process for all NG-model variations can be extracted from Table 3.4.

Based on the comparison of these model fits we can state that among the variations

selected, the original NG-model describes the kinetics of the silica polymerization in the best way. This result let us to conclude that the formation of a reactive monomer via a precursor reaction, is required to reproduce the induction period in a proper way. However, it remains to be scrutinized if a growth model with a size dependent growth rate constant k_e or the assumption of a nucleus size n>1 might be similarly successful.

3.5.3. Nucleation Growth with Equilibrium (NGE-Model)

The previously introduced models bear a few severe simplifications. First, no equilibrium state of the monomers is taken into account, as only growth and no degradation of the particles is permitted. Second, the results for the rate constant of the precursor step vary over several orders of magnitude depending on the initial silica concentration, which is difficult to explain with physics. This likely happened because the nucleation step in which one monomer acts as a nucleus is too simple to account for the complex nucleation or initiation step in reality. This deficiency may have been compensated by the variation of the rate constant of the precursor step which helped to vary the induction period with changing initial silica content. Third, nucleation is a simple first order reaction. In the following an improved model shall be introduced, denoted as Nucleation-Growth-Equilibrium-model (NGE-model). The model incorporates two improvements: (i) growth via monomer addition is a true equilibrium reaction, as it considers explicitly depolymerization as the back reaction of addition and (ii) the nucleation allows for a variation of the size of a nuclei indicated by the degree of polymerization n. Improvement (ii) enables to consider qualitatively that the size of critical nuclei on average vary with the initial concentration of monomers.

Equations 3.20 describe the three basic reactions (i) precursor reaction, (ii) nucleation at variable size of the nuclei and (iii) reversible monomer addition.

$$\begin{aligned} &\text{Monomer Formation} && A \xrightarrow{k_p} B \\ &\text{Nucleation} && nB \xrightarrow{k_n} C_i \\ &\text{Addition and Degradation} && B + C_i \underset{k_{-e}}{\overset{k_e}{\rightleftharpoons}} C_{i+1} \end{aligned} \tag{3.20}$$

In Equation 3.20 the degree of polymerization of growing particles i is $i \geq n$. With these modifications the master equation (Equation 3.6) from the NG-model changes to

$$\frac{d[C_i]}{dt} = k_n[B]^n\delta_{in} + k_e[B][C_{i-1}](1-\delta_{in}) - k_e[B][C_i] - k_{-e}[C_i](1-\delta_{in}) + k_{-e}[C_{i+1}] \tag{3.21}$$

where k_{-e} is the rate constant of the degradation. A derivation in analogy to Equation 3.6 leads to the following expressions for the particle moments and is shown stepwise in the Appendix in Chapter A.2.

$$\frac{d[C]^{(0)}}{dt} = k_n[B]^n \tag{3.22}$$

$$\frac{d[C]^{(1)}}{dt} = k_n[B]^n n + k_e[B][C]^{(0)} - k_{-e}[C]^{(0)} \tag{3.23}$$

$$\frac{d[C]^{(2)}}{dt} = k_n[B]^n n^2 + k_e[B](2[C]^{(1)} - [C]^{(0)}) - k_{-e}(2[C]^{(1)} - [C]^{(0)}) \tag{3.24}$$

The decrease of the monomer concentration can be described as

$$\frac{d[B]}{dt} = k_p[A] - nk_n[B]^n - k_e[B][C]^{(0)} + k_{-e}[C]^{(0)}. \tag{3.25}$$

Equations 3.22-3.25 together with the single exponential decay of the precursor reaction Equation 3.14 form a system of differential equations, which can be integrated numerically giving the concentrations of the precursor, of the monomers and the zeroth, first and second moment depending on time. Numerical calculations were performed similar to the NG-model with Matlab software and the implemented ordinary differential equation solver ode45. Optimal parameters have been found by variation of k_p, k_n and k_e, using the simplex search method by Lagarias[100] by means of the "fminsearch" command. The weight-averaged molar mass is accessible via Equation 3.17. The equilibrium concentration of the monomers links rate constant of the monomer release with the rate constant of the monomer addition via the equilibrium concentration.

$$k_{-e} = k_e[B]_{equ} \tag{3.26}$$

$[B]_{equ}$ denotes the equilibrium concentration and adopts the value of 170 ppm respectively $2.829 \cdot 10^{-3}$ mol/l of SiO_2. Although the NG- and the NGE-model simulate the nucleation/initiation of the silica formation process in a very simple way, they provide a clear benefit for the interpretation of time-resolved light scattering data. Both models do not only allow to simulate the consumption of the monomers and with that the changing supersaturation with time, but also to calculate the variation of the moments of the particle ensemble with time, which makes possible for the first time a direct comparison with the weight-averaged molar mass detected via SLS. Beyond doubt the strength of the model lies on the description of particle growth, which is exactly what is recorded by TR-SLS/DLS.

The simple NG-model did not account for the equilibrium state of the reaction. In the actual model this could be implemented. As a proof of concept Figure 3.31 depicts typical trends with time t of the precursor concentration and the monomer concentration resulting from a calculation with the NGE-model. It is a calculation example based on an initial silica concentration of 350 ppm. At first the monomer concentration increases with decreasing precursor concentration and after passing a maximum it decreases until the equilibrium concentration of 170 ppm is reached. Furthermore Figure 3.31 shows the evolution of the number of growing particles, which is reflected by the zeroth moment $[C]^{(0)}$. From the latter trend it is obvious that particles can only occur, if the monomer concentration lies above the equilibrium concentration.

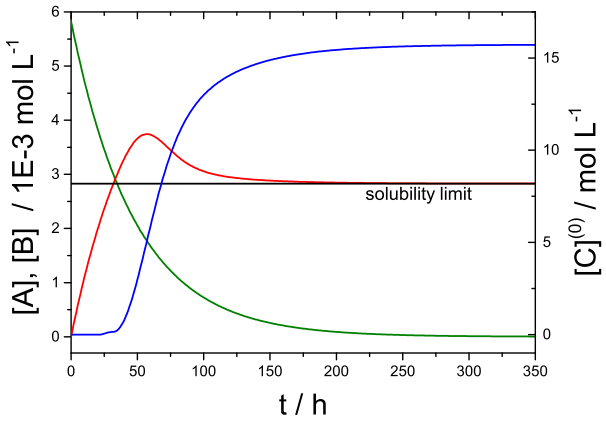

Figure 3.31.: Trends calculated by the NGE-model for an initial silica concentration of 350 ppm: precursor concentration [A] (—), monomer concentration [B] (—) and zeroth moment $[C]^{(0)}$ (—), which corresponds to the concentration of polymers/particles. The horizontal black line indicates the equilibrium concentration of 170 ppm.

The results of experiments where no salt has been added will be used first to discuss the performance of the NGE-model in comparison to that of the simple NG-model. Figure 3.32 represents a comparison of the fitting results obtained by the original NG-model and the new NGE-model. A significant improvement could be achieved for the silica contents 350 and 400 ppm. The fit with the NGE-model is particularly improved in the time range of the initial increase of the particle mass. In case of the highest silica contents of 500 and 750 ppm the NGE-model does not significantly improve the fit quality achieved with the NG-model, but helps to confine k_p to a range much narrower than in case of the NG-model. A more detailed presentation of the fits with the NGE-model with regard to the weight-averaged molar mass, the monomer concentration and the concentration of particles, given by the zeroth moment $[C]^{(0)}$ is plotted in Figure 3.33. The evolution of the monomer concentration based on the model calculations show a clear difference between the two lower silica contents (350 ppm, 400 ppm) and the two higher silica contents (500 ppm, 750 ppm). For low silica contents the precursor reaction is slow, the end of the induction period correlates with the time when the monomer concentration $[B]$ reaches the equilibrium concentration. Nucleation is allowed from that time on. Successively the monomer concentration passes a maximum value, as consumption of monomers by nucleation and growth is slower than the generation of monomers via the precursor reaction. If the precursor reaction ends, monomers are still incorporated into growing particles until the equilibrium concentration of the monomers is reached. In case of higher silica contents (500 ppm and 750 ppm) the precursor reaction is fast, the equilibrium concentration is reached already after $t \approx 1$ h, simultaneously the rate constant of nucleation k_n and the rate constant of monomer addition k_e is high. Active monomers, which are generated by the precursor reaction are directly consumed by nucleation and

growth and an excess of $[B]$ cannot be reached. The monomer concentration increases up to its equilibrium concentration and stays constant at this value, but formation and consumption of monomers is still going on.

The result of an increased rate constant of nucleation and an increased rate constant of monomer addition with increasing silica concentration is in line with previous assumptions based on detailed considerations of the experimental data in Chapter 3.1.1. In this preceding discussion these two trends have been assumed, because the size of the silica particles is decreasing with increasing initial silica content. An increasing nucleation rate leads to a higher number of nuclei with the ability to grow. Remaining monomers which can participate in the particle growth process have to be shared by more nuclei as in case of a lower initial silica content, as a result the particles reach a smaller final size as in case of a lower initial silica content.

Classical nucleation theory[51,54–56] predicts a decreasing nucleus size with increasing supersaturation. In the light of this theory the concentration series has an increasing initial degree of supersaturation in going from 350 ppm to 750 ppm SiO_2. The NGE-model enables us to consider this feature qualitatively by varying the size n of the critical nucleus. However, one has to keep in mind that during the growth process obeying classical nucleation theory the critical nucleus size increases with decreasing monomer concentration (with decreasing degree of supersaturation), which is not accounted for by the NGE-model. In order to determine the optimal nucleus size for each initial silica concentration, the fitting has been performed for different nucleus sizes in the range of $1 \leq n \leq 30$. The fit with the lowest χ^2-value (Equation 3.19), has been used to identify the optimal nucleus size. As the value χ^2 depends on the absolute mass values, residuals from different concentrations cannot be compared directly. Only the χ^2-values among one single silica concentration can be used to define the optimal nucleus size. The resulting optimal n-values are summarized in Table 3.5. Unfortunately, identification of n based on χ^2 values could not be achieved with the same degree of significance for all four silica contents (see Figure 3.35). However, the data show that the most suitable nucleus size n (3.5) is decreasing with increasing initial silica content, which is in line with the predictions of the classical nucleation theory. It has to be stressed that the formation and growth of silica particles is based on the incorporation of monomeric building units via chemical bonding corresponding to a three dimensional polymerization or polycondensation reaction, which may well differ considerable from a pure crystallization following a classical nucleation process.

Unlike the behavior in the presence of salt, silica particles generated in a solution of 750 ppm do not show particle–particle aggregation in the absence of added salt. In that case the concentration threshold, which marks the beginning of a particle–particle aggregation, lies well above 750 ppm. However, as inferred from the poorer performance of the NG and NGE model at the two silica contents 500 and 750 ppm in salt-free solution, those two higher silica contents are much less dominated by particle growth. After a very fast increase the hydrodynamic radius remains constant within experimental uncertainty at a value of 4-5.5 nm while the weight-averaged molar mass is still slightly increasing. This behaviour suggests that the increase of M_w is dominated by the further formation of particles rather than by incorporation of monomers to growing particles. The experimen-

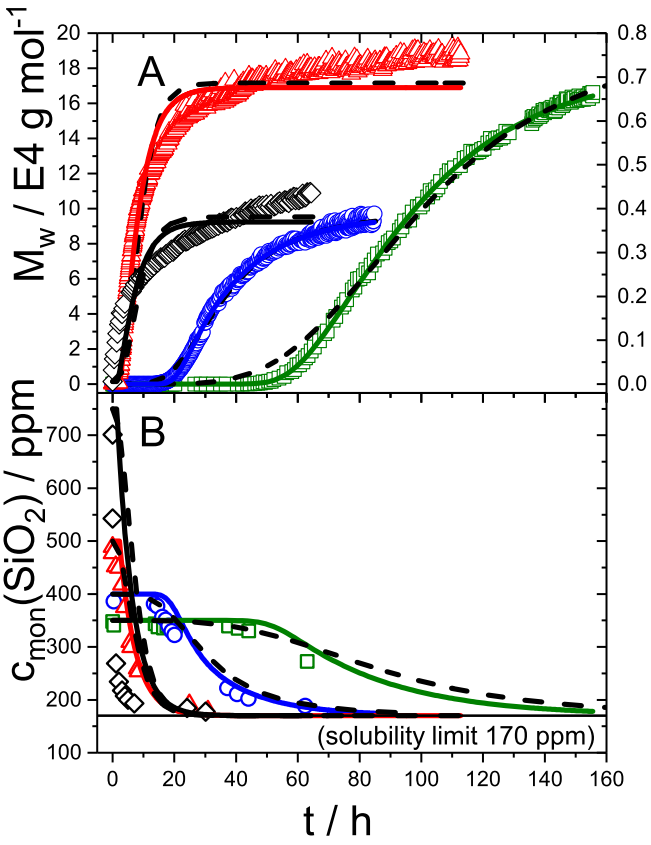

Figure 3.32.: Comparison of the experiments in the absence of additional electrolytes (350 ppm (□), 400 ppm (○), 500 ppm (△), 750 ppm (◇)) with the fits based on the NG-model (dashed line) and the NGE-model (solid line) in terms of the weight-averaged molar mass (A) and the monomer consumption (B). The experimental mass values refer to two different scales with arrows pointing to the corresponding axis.

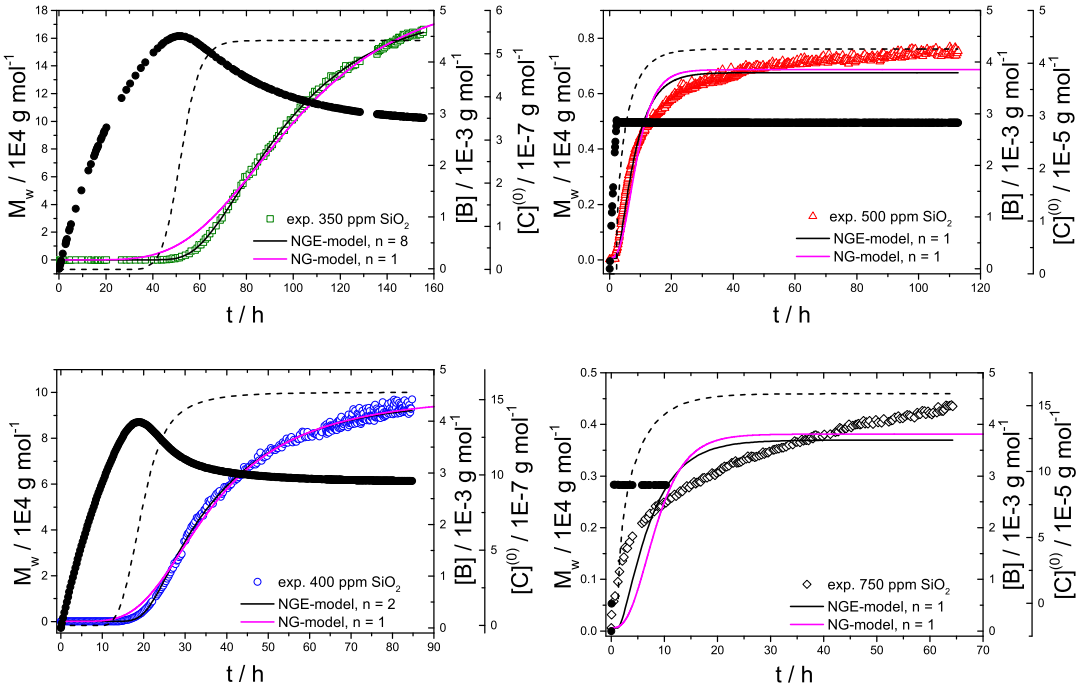

Figure 3.33.: Comparison of the experimental weight-averaged molar mass M_w of experiments in pure water with the corresponding fits at variable silica contents performed with the NG-model (—) and the NGE-model (—). In case of the NG-model the critical nucleus size is $n = 1$, as for this model no variation of n was implemented. In case of the NGE-model the fits with the optimal nucleus size are shown. The silica content and the nucleus size are indicated in the respective graph. The model calculations based on the NGE-model are additionally represented in terms of the concentration of particles $[C]^{(0)}$ (– – –) and the concentration of active monomers $[B]$ (●).

tally observed generation of particles with the size around 4-5.5 nm at 500 and 750 ppm of SiO_2 is interpreted as follows by the NGE model. A very large nucleation rate leads to the final amount of particles in a short time. These particles have to add the remaining monomers necessary to reach the final mass values also very quickly in order not to compete with further nucleation, since further nucleation would make the final particle mass too low. Accordingly, the fits lead to a constant size and weight-averaged molar mass of the particles soon after nucleation, which appears not to be fully compatible with data from 500 and 750 ppm. A simple increase of the nucleation rate cannot describe gradually increasing mass at later stages of the reaction.

In order to follow at least the initial phase of nucleation the fits for 750 ppm and 500 ppm have been repeated based on a reduced data set. The results are shown in Figure 3.34. The data have been cut off at $t \approx 10$ h for 750 ppm and at $t \approx 16$ h for 500 ppm. This reduced data set should represent only the initial nucleation and neglect the regime,

Table 3.5.: Rate constants at variable silica contents in the absence of salt at pH 7 from fits with the NGE-model to data from the concentration series in salt-free solution. The value n describes the size of the theoretical nuclei in Equation 3.20 which yields the smallest χ^2-value, k_p is the rate constant for the precursor reaction, k_n for the nucleation and k_e for the growth reaction in Equation 3.20. The asterisk indicates the fits to the reduced data set. The data has been cut off at $t \approx 10$ h for 750 ppm and at $t \approx 16$ h for 500 ppm.

	$c_{0,exp}$ [ppm]	n (fixed)	n (optimal)	k_p [h^{-1}]	k_n [$(L/mol)^{n-1}$ h^{-1}]	k_e [$L(mol\ h)^{-1}$]	χ^2 [$g\ mol^{-1}$]
	350		8	3.15E-2	5.25E14	8.67E4	1.70E1
	350	1		2.05E-2	1.42E-5	2.03E5	3.69E1
	400		2	5.50E-2	1.04E-1	1.86E5	4.85E1
salt-	400	1		4.99E-2	1.06E-4	2.42E5	5.12E1
free	500		1	1.91E-1	1.03	6.15E6	3.92E1
	500*		1	2.42E-1	5.21-1	2.06E6	6.29
	750		1	1.94E-1	5.08	3.81E6	8.15E1
	750*		1	8.12E-1	4.24	1.16E6	4.25E1

where the mass values increase and the hydrodynamic radius is constant. As indicated by Table 3.5 the fit can be improved by cutting off experimental data from a certain time on especially for 500 ppm SiO_2 but in case of 750 ppm SiO_2 improvement is only marginal.

Evaluation with the NGE-model shall be concluded with a focus on the different rate constants. Table 3.5 summarizes the optimized rate constant of the precursor reaction k_p derived from the fits to the experimental data for silica in salt-free solution at pH 7 for different nucleus sizes n. The upper graph of Figure 3.36 shows the rate constant of the precursor reaction k_p obtained by the fits depending on the nucleus size n. For all initial silica contents we see an increase of the rate constant k_p with increasing nucleus size. The precursor reaction was introduced in order to model the induction period, because a simple formation model consisting of a nucleation and a growth reaction with a rate constant independent of the degree of polymerization is not able to reveal an induction period. We expected a constant value for k_p for all initial silica contents. In this respect the NG-model failed, since the rate constant of the precursor reaction was increasing by several orders of magnitude with increasing silica content. The NGE-model (Table 3.5) with its nucleation/initiation reaction of variable order n significantly improved this issue. In comparison to the NG-model (Table 3.2) the rate constant of the precursor reaction with the NGE-model only varies in the range of one order of magnitude.

The lower graph of Figure 3.36 shows the trend of the rate constant for the growth k_e with increasing nucleus size. For all silica contents, we see a clear decrease of k_e with increasing nucleus size. In case of 750 ppm this decrease extends over four orders of magnitude. This huge variation is in line with the fact the NGE-model reproduces the evolution of mass poorest for this high silica content. The rate constant k_e is in the order of

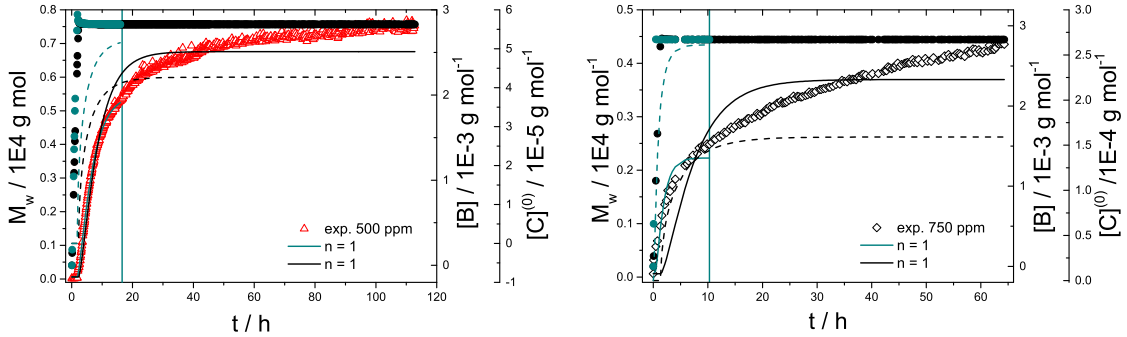

Figure 3.34.: Effect of data cut-off in case of experiments in salt free solution. Fits with the NGE-model for the silica contents 500 ppm (left) and 750 ppm (right) to the weight-averaged molar mass M_w (—), the concentration of particles $[C]^{(0)}$ (– – –) and the concentration of monomers $[B]$ (●). Black curves show the results of a fit using the whole range of available experimental data and the cyan curves represent the results of a fit up to the cyan, vertical line. Thus for 500 ppm the fit ends at $t \approx 16$ h and for 750 ppm at $t \approx 10$ h.

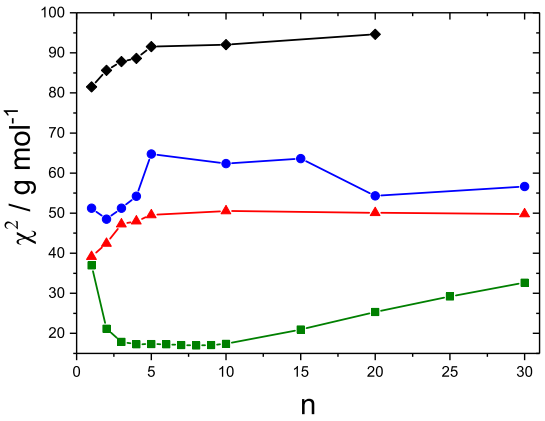

Figure 3.35.: Quality of the fits based on the NGE-model in terms of the value χ^2 as a function of the nucleus size n. Silica contents in pure water at pH 7: 350 ppm (■), 400 ppm (●), 500 ppm (▲) and 750 ppm (◆).

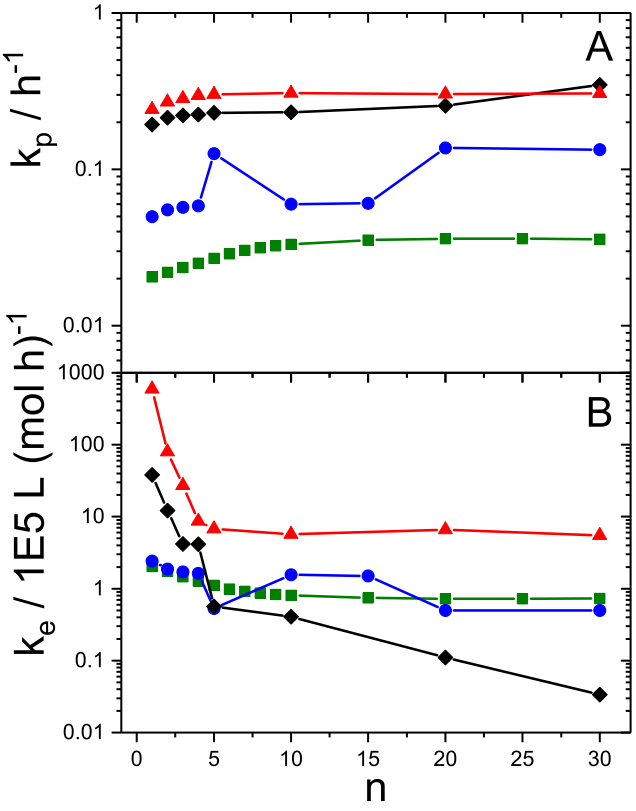

Figure 3.36.: Rate constants k_p (A) and k_e (B) as a function of the nucleus size n by applying the NGE-model at variable silica contents in the absence of additional salt at pH 7: 350 ppm (■), 400 ppm (●), 500 ppm (▲) and 750 ppm (◆).

10^5 L(mol h)$^{-1}$ at 350 ppm and 400 ppm of silica and increases by one order of magnitude at the higher silica contents. This jump is a hint for deficiencies in the NGE-model as soon as the growth is not the dominating part any more.

We conclude that modelling of the silica polymerization could be improved by the NGE-model with respect to the following aspects. The variation of the rate constant of the precursor reaction could be confined to two orders of magnitude, which is significantly narrower than the respective variation over eleven orders of magnitude observed with the NG-model. If we consider only the two lowest silica concentrations, for which we have unambiguously demonstrated, that a monomer-addition mechanism is dominating, the deviations in k_p are even lower. Variation of the nucleus size has shown that the silica polymerization follows the trend of a decreasing nucleus size with increasing degree of supersaturation, which is in accordance with classical nucleation theory. The equilibrium

state of the silica polymerization could be successfully modelled by the implementation of a depolymerization reaction in which the polymers release monomers. A possible explanation for the deficiencies of the NG and NGE-model observed with the two higher silica contents would be an ongoing generation of nuclei as particles similar in size during the entire experimental time period, with a single type of particle being formed within a short period of time compared to the length of the overall period. Such a feature could in fact also be described by the NGE-model if n would be fixed at values large enough to correspond to 3-4 nm in size and if the rate constant of this nucleation would be very high in comparison to the rate constant of the monomer-addition. This results in a transfer of the main fraction of the active monomers into nuclei with a size large enough to fit M_w values in the order of $4 \cdot 10^3 - 8 \cdot 10^3$ g mol^{-1} and R_h values close to 4 nm. However, such size and mass values of a nucleus which are much larger as the n values observed at low silica contents would not be compatible with the classical nucleation theory because the size of nuclei are expected to get smaller as the dregree of supersaturation (i.e. c_0) increases and not larger. A possible explanation is that the initiation reaction as part of step 1 is not fully in accordance with the nucleation in the sense of classical nucleation theory.

After having evaluated the NGE-model with the data recorded under salt-free conditions, experiments in the presence of Ca^{2+}+Mg^{2+} and in the presence of additional Na^+ shall now be interpreted with the NGE-model. The experimental data corresponding to a silica content of 750 ppm has been excluded from the optimization process, as the correlation of the size with the mass-values (shown in Figure 3.12, right hand site) revealed that the particle formation is dominated by a step-growth like particle-particle aggregation. The fits with the NGE-model are represented in Figure 3.37 and the corresponding rate constants obtained from the optimization applied to the mass evolution of the experiments in the presence of metal cations are given in Table 3.6. For each silica content the results corresponding to the optimal nucleus size determined by the smallest χ^2-value are shown. Further details of the fits, like the evolution of the concentration of active monomers $[B]$ and the zeroth moment $[C]^{(0)}$ describing the concentration of growing particles are shown in the Appendix (Figure A.2 and A.3).

The optimal nucleus size generally drops with increasing silica content in the presence of Ca^{2+}+Mg^{2+}. The optimal nucleus size of n = 8 for 350 ppm is determined with an acceptable significance, as χ^2 as a function of time shows a clear minimum (Figure 3.38). However, at 400 ppm no minimum could be determined for χ^2 with increasing n. For data recorded at 500 ppm n = 1 is the optimal nucleus size. Fitting of the experimental data measured in the presence of additional Na^+ reveals an optimal nucleus size of n = 10 (400 ppm) and n = 1 (500 ppm). χ^2 as a function of n is gradually decreasing for data recorded at 350 ppm thus prohibiting identification of an optimal n in this case (Figure 3.39). As just mentioned, in the case of 400 ppm (with Ca^{2+}+Mg^{2+}) and 350 ppm (with Na^+) the variation of n shows no minimum. An explanation could be that the experimental data of these two samples had not been recorded long enough to show the final plateau value. Despite the fact that the optimal nucleus size is not always significant, a decreasing trend of the optimal nucleus size with increasing supersaturation independent on the salt conditions is obvious. As the reaction order is changing with the applied nucleus size,

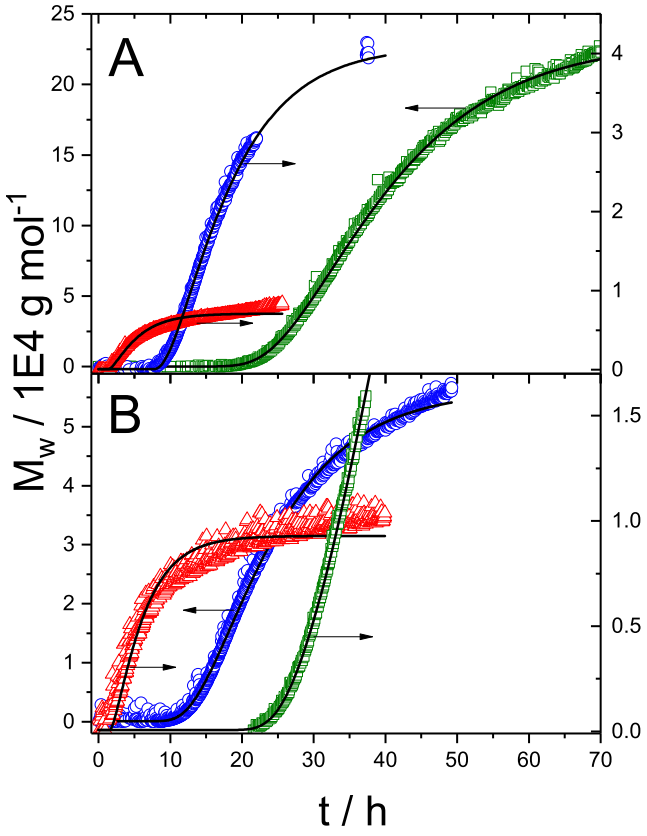

Figure 3.37.: Comparison of the experimental weight-averaged molar mass M_w with the corresponding fits at variable silica contents and with the optimal nucleus size. (A) Experiments in the presence of Ca^{2+}+Mg^{2+}-ions; (B) experiments in the presence of Na^{+}-ions. Note that the experimental data have different scales for a better overview. The arrows point to the corresponding axis. The model calculations based on the NGE-model are represented as solid line.

Table 3.6.: Rate constants at variable silica contents in the absence of salt at pH 7 from fits with the NGE-model to data from the concentration series in salt-free solution. The value n describes the size of the theoretical nuclei in Equation 3.20 which yields the smallest χ^2-value, k_p is the rate constant for the precursor reaction, k_n for the nucleation and k_e for the growth reaction in Equation 3.20. The asterisk indicates cases when χ^2 was continuously decreasing with n and where the values correspond to the fit with the maximum possible n.

	$c_{0,exp}$ [ppm]	n (fixed)	n (optimal)	k_p [h^{-1}]	k_n [$(L/mol)^{n-1}$ h^{-1}]	k_e [$L(mol\ h)^{-1}$]	χ^2 [$g\ mol^{-1}$]
	350		8	9.39E-2	2.26E14	2.08E5	7.91E1
	350	1		5.97E-2	1.89E-5	3.83E5	1.43E2
Ca^{2+}+	400		20*	1.29E-1	5.07E51	1.18E5	6.66E1
Mg^{2+}	400	1		9.89E-2	5.83E-4	2.50E5	8.98E1
	500		1	2.94E-1	4.12	2.71E7	3.87E1
	350		30*	1.16E-1	2.37E71	4.01E4	7.03
	350	1		4.49E-2	1.37E-4	1.09E5	8.12
Na^+	400		10	2.16E-1	1.12E19	4.46E4	8.82E1
	400	1		1.58E-1	8.00E-5	5.39E4	1.33E2
	500		1	2.60E-1	5.23	5.90E7	7.29E1

the parameters corresponding to a fit with $n = 1$ are used to compare the rate constant of nucleation. With the reaction order fixed to 1, which corresponds to a nucleus size $n = 1$ the rate constant of the nucleation is increasing with increasing silica content. In the presence of additional Na^+ this trend is less pronounced, the rate constant for the nucleation at 350 ppm and 400 ppm are nearly equal. As mentioned in the preceding paragraph at 350 ppm silica in the presence of Na^+ the experimental data do not cover the entire growth process including the plateau value of the weight-averaged molar mass and we expect the uncertainty of the fit parameters to be higher in this case.

The corresponding trend of the rate constant of the precursor reaction and the growth reaction are depicted in Figure 3.40 (in the presence Ca^{2+}+Mg^{2+}-ions) and Figure 3.41 (in the presence of additional Na^+-ions). For all considered silica contents independent of the salt conditions the rate constant of the precursor reaction increases with increasing value of nucleus size. The variation of the rate constant of the precursor reaction in the presence of salt extends over one order of magnitude only and hence is similar to that of the salt-free case. The rate constant of the growth reaction shows a decreasing trend with increasing nucleus size in the presence of salt and in the salt-free case. It lies again in the order of magnitude $\sim 10^5$ $L(mol\ h)^{-1}$ at silica contents lower than 500 ppm and can be considered as constant within the range of uncertainty. We thus can conclude that the absence or presence of Ca^{2+}+Mg^{2+} or Na^+ does not significantly affect the rate constant k_e of the particle growth. As the reaction order is changing with the applied nu-

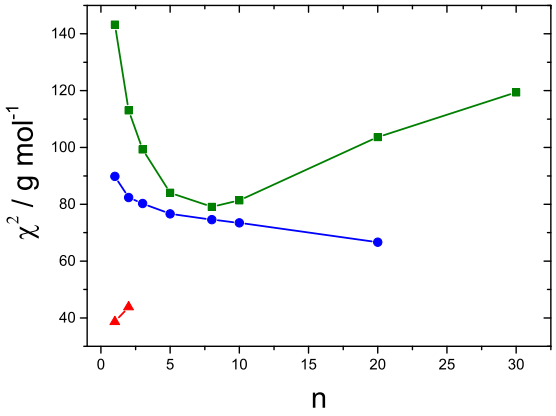

Figure 3.38.: Quality of the fits with the NGE-model in terms of the value χ^2 as a function of the nucleus size n. Silica polymerization in the presence of Ca^{2+}+Mg^{2+} at pH 7 at three different silica contents: 350 ppm (■), 400 ppm (●), 500 ppm (▲).

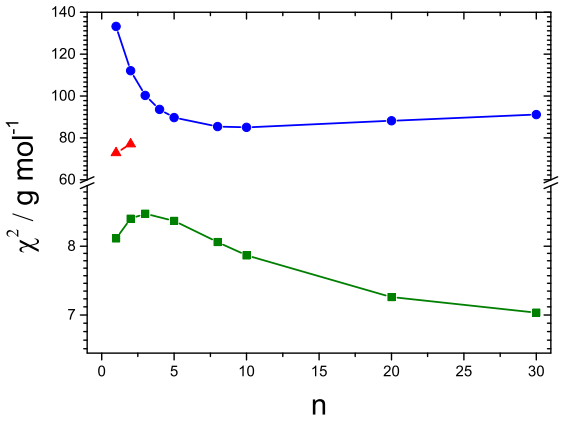

Figure 3.39.: Quality of the fits with the NGE-model in terms of the value χ^2 as a function of the nucleus size n. Silica polymerization in the presence of additional Na^+ at pH 7 at three different silica contents: 350 ppm (■), 400 ppm (●) and 500 ppm (▲).

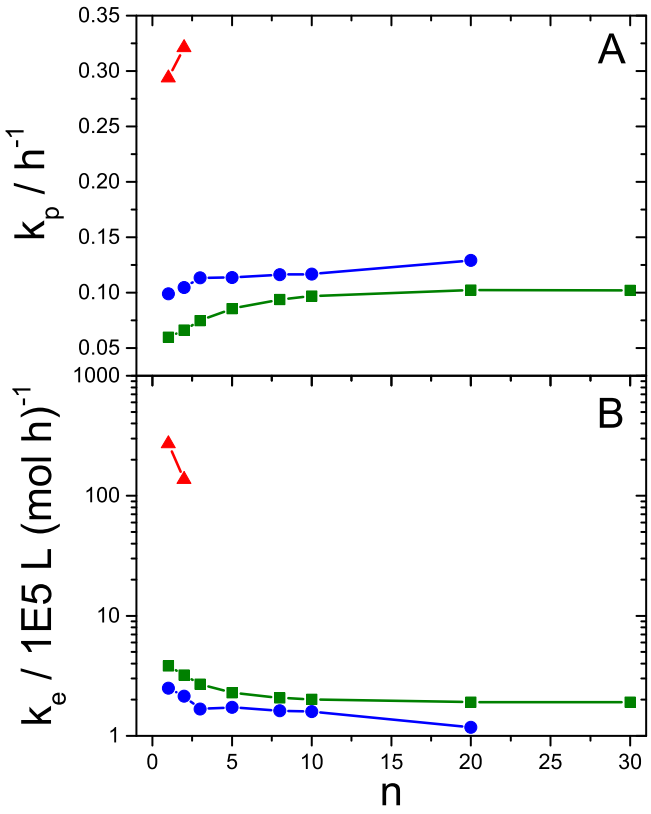

Figure 3.40.: Rate constants k_p (A) and k_e (B) at three different silica contents as a function of the nucleus size n by applying the NGE-model. Silica contents in the presence of Ca^{2+}+Mg^{2+}-ions at pH 7: 350 ppm (■), 400 ppm (●) and 500 ppm (▲).

cleus size, the parameters corresponding to a fit with n = 1 are used to compare the rate constant of nucleation. With the reaction order fixed to 1, which corresponds to a nucleus size n = 1 the rate constant of the nucleation is increasing with increasing silica content.

A characteristic magnitude for the nucleation/initiation is the number of generated particles, which is described by the zeroth moment. Figure 3.42 compares the final value of the zeroth moment, depending on the silica content and the reaction conditions. The particle number is clearly increasing with increasing silica content, which confirms that the nucleation/initiation is accelerated and plays a more dominating role with increasing supersaturation. However, the influence of the presence of salt has only a minor effect on the number of formed particles and shows no clear trend.

To summarize, the NGE-model unlike to the NG-model can reproduce the evolution of mass at variable initial silica concentration by an interplay of the rate constant of

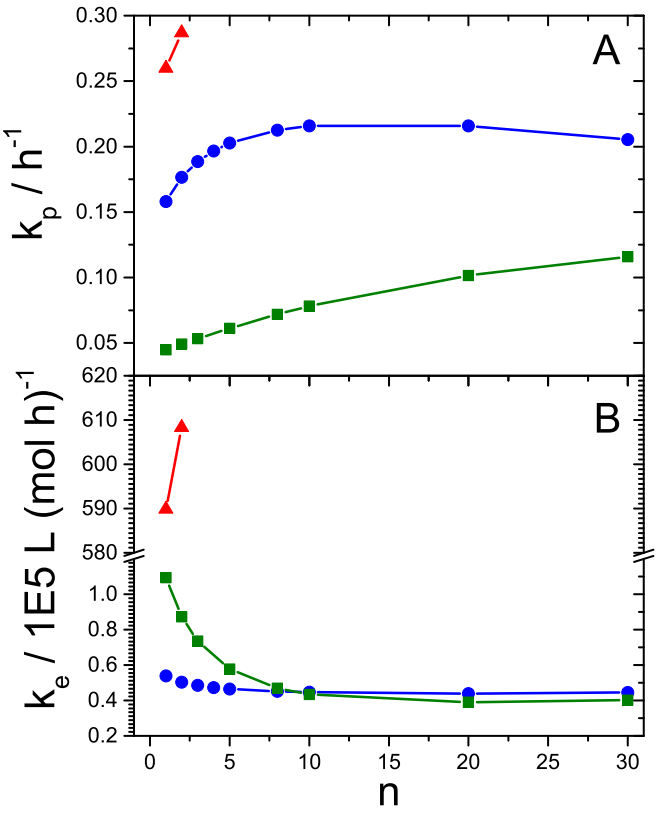

Figure 3.41.: Rate constants k_p and k_e at three different silica contents as a function of the nucleus size n from fits with the NGE-model. Silica contents in the presence of additional Na^+-ions at pH 7: 350 ppm (■), 400 ppm (●), 500 ppm (▲).

the precursor reaction and the size of the nuclei, which is connected with a change in the reaction order of the nucleation step. This works satisfactorily in case of the lowest silica concentrations 350 ppm and 400 ppm independent of the conditions, suggesting that the addition of salt does not influence the general mechanistic features of the reaction. It has to be emphasized that the precursor reaction together with the initiation/nucleation reaction of the NG- and NGE-model establish the first step of the 3-step mechanism. This first step usually denoted as nucleation step is increasingly dominating the process of particle formation, once the silica content increases beyond 400 ppm and the NGE-model like the NG-model performs progressively poorer. This becomes obvious not only in terms of the decreasing fit quality but also in terms of the resulting rate constants of the growth reaction, which at 500 ppm are deviating from those obtained at the lower silica contents.

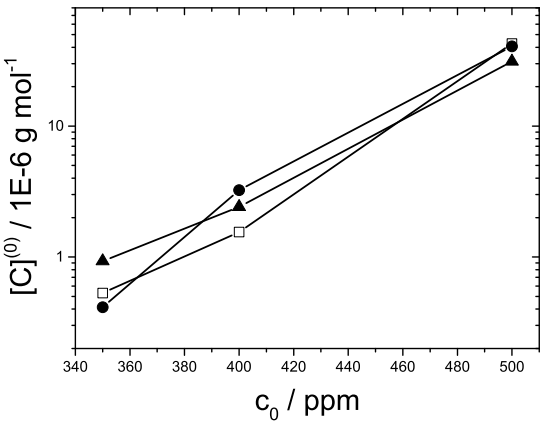

Figure 3.42.: Final number of particles represented as zeroth moment based on the optimal fit with the NGE-model for the corresponding silica content for different conditions: Silica in the absence of additional salt (□); in the presence of additional Na^+ (▲) and in the presence of Ca^{2+}+Mg^{2+} (●).

3.6. Review of the Kinetic Considerations

The detailed mechanistic studies on the silica concentration series in water, in the presence of Ca^{2+}+Mg^{2+} and in the presence of additional Na^+ have confirmed the findings based on the discussion of the experimental data obtained by time-resolved combined DLS/SLS and the molybdenum blue method. In line with the literature a three step process can be identified for the silica polymerization, characterized by (1) a nucleation/initiation step, (2) a particle growth stage and (3) agglomeration of the particles generated in step 2. Confinement of the monomer-addition mechanism and the aggregation of the particles formed during this process was not only indicated by the size-mass correlation and along with it a changing morphology from compact spherical structures to fractal-like structures, aggregation was also proven by the explicit linear dependencies of the size and the weight-averaged molar mass with the experimental time in a double logarithmic scale, identifying the aggregation as diffusion-limited particle-particle aggregation (DLCA). In addition, a lack of linear dependencies of the size and mass with time indicated conditions preventing agglomeration and confirmed once more in these cases the monomer-addition mechanism. The investigation under different salt conditions clarified that the threshold concentration, marking the starting point for the particle-particle aggregation, depends on the presence of metal cations. While it lies above 750 ppm SiO_2 in the absence of additional salt, the presence of 0.01 N Ca^{2+}+Mg^{2+} or Na^+ leads to a shift of this threshold concentration below 750 ppm SiO_2.

Two kinetic models have been used to simulate the evolution of the weight-averaged molar mass and the consumption of the monomeric silica. The moments of the particle ensemble has been deduced from the kinetic differential equations and could be calculated numerically, yielding the time-dependent weight-averaged molar mass, which

enables direct comparison to the static light scattering data. Whereas the NG-model could satisfactorily reproduce the evolution of the weight-averaged particle mass as well as the consumption of monomers at 350 ppm and 400 ppm, its performance turned out to be poorer at the higher silica contents of 500 ppm and 750 ppm. This is attributed to an increasing influence of the initiation/nucleation reaction with increasing silica content. Another drawback of the NG-model was the broad variation for the rate constant of the precursor reaction, which cannot be explained adequately with physics. The NGE-model include two improvements, the nucleation is now accounted with a variable reaction order, as the nucleus size n is variable and the equilibrium concentration is established by the introduction of monomer release as depolymerization. By these implementations it was achieved that the rate constant of the precursor reaction only varies in one order of magnitude which is a significant improvement. The rate constant of the growth reaction also remains constant independent from the initial silica concentration. Furthermore determination of the optimal nucleus size for the respective initial silica content gives a clear trend of a decreasing nucleus size with increasing supersaturation. This result is in line with the classical nucleation theory.

The poorer performance of the NG- and the NGE-model for the higher silica contents is related to the increasing importance of the initiation/nucleation step with increasing silica concentration. The nucleation reaction is extended over the entire reaction time generating more particles of the same size, leading to a constant hydrodynamic radius and a slightly increasing weight-averaged molar mass. The growth process in terms of the addition of monomers to the nuclei is only of minor importance. Simulation of such a process with the NGE-model is only possible if the nucleus size is drastically increased to a size similar to that observed as hydrodynamic radius and a very small rate constant of the growth reaction. However, this would contradict the result of a decreasing nucleus size with increasing supersaturation and therefore also contradicting the classical nucleation theory.

3.7. Silica Polymerization in the presence of polymeric additives

One of the most challenging problems in water-treatment applications is scaling and fouling. Deposition of inorganic or organic materials from feed water onto the surface of equipments like boilers, heat exchangers and membranes lead to increased maintenance costs. Especially all membrane separation processes including the technology of reverse osmosis (RO), which became the leading technique in the desalination industry, suffer from this problem. The depositions consist mainly of calcium carbonate, calcium sulfate, barium sulfate, strontium sulfate, calcium phosphate, silicates and alumino-silicates. Among these deposits silica scaling is the most problematic in the extraction of drinking water from seawater via the RO technology. In seawater or brackish water silica is present at low concentrations, below the critical supersaturation. However, next to the surface of the membrane, the concentration is drastically increased, resulting in a local supersatura-

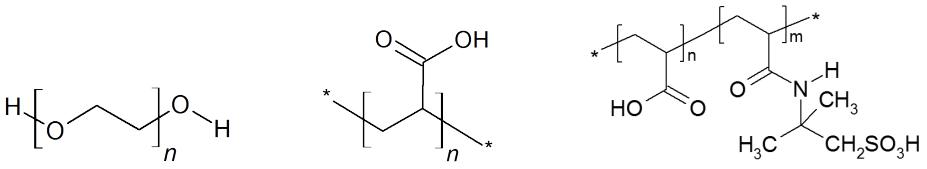

Figure 3.43.: Chemical structure of poly(ethylene) oxide (left), poly(acrylic acid) (center) and acrylic acid-2-acrylamido-2-methylpropane sulfonic acid copolymer (right).

tion and the formation of silica depositions. These depositions on the membranes lead to a reduced flux and with that to reduced RO efficiencies and increasing energy losses. The maintenance costs for desalination plants are increased by the occurrence of fouling as equipment has to be cleaned more often, causing plant shut-downs and costs for cleaning materials or even an exchange of the membrane.[101] Therefore there is a great interest in developing polymeric additives, which are able to reduce silica fouling and scaling.

Several approaches exist to inhibit silica polymerization, including the increase of the solubility limit of silica and the dispersion of precipitated silica by means of polymeric additives. In this context, the previously discussed experiments (see Chapter 3.1 and 3.2) characterizing the process of silica polymerization from supersaturated aqueous solutions should serve as reference for the investigation of the silica polymerization in the presence of polymers. In order to transfer the results for the silica polymerization in the presence of polymeric additives to the situation at a RO membrane, the experiments are performed under conditions typical for an operating RO membrane (neutral pH, temperature 37 °C, 5 mM Ca^{2+}+Mg^{2+}(mimicking hard water)).

In the following we want to discuss the influence of a few selected water-soluble polymers (see Figure 3.43) on the silica polymerization under these conditions and their ability to inhibit the formation of silica particles. For this purpose the results obtained via time-resolved SLS/DLS and the molybdenum blue method are compared with the results from the reference experiments already discussed in Chapter 3.1 and 3.2. We investigated the influence of the negatively charged polyelectrolytes, poly(acrylic acid) (PA) as a weak polyelectrolyte and the copolymer poly(acrylic acid)-2-acrylamido-2-methylpropane sulfonic acid (AA-AMPS) as a polyelectrolyte which is more hydrophilic and more acidic. As a neutral polymer poly(ethylene oxide) (PEO) has been chosen. In order to make the comparison of the polymer experiments with the reference experiments from Chapter 3.1 and 3.2 as significant as possible and in order to reveal the role of the presence of salt ions for the interactions between polymers and silica, the silica polymerization in the presence of the polymeric additives have also been investigated in the presence of salt (Ca^{2+}+Mg^{2+}) as well as under salt-free conditions.

3.7.1. Influence of Poly(ethylene oxide)

The influence of poly(ethylene oxide) (PEO) has been investigated at silica contents of 400, 500 and 750 ppm in pure water and in the presence of Ca^{2+}+Mg^{2+}. The prepara-

tion of the solutions has been performed in the same way as described in Chapter 2.5. The addition of a PEO stock solution has been done right after the pH adjustment for experiments under salt-free conditions. In case of experiments in the presence of salt, the pH-adjustment successively is followed by the addition of the salt stock solution and the PEO stock solution. The concentration of PEO in the resulting solution is 15 ppm. The solution has been investigated in analogy to the reference experiments via the molybdenum blue method and time-resolved static light scattering. Figure 3.44 summarizes the time-dependent weight-averaged molar mass obtained for the silica polymerization process in the presence of PEO. Both measurement series, in the presence and in the absence of salt, show a lag-time at silica contents lower than 750 ppm SiO_2. During the lag-time no increase in the scattering intensity and with that no increase in the weight-averaged molar is detected. However, the consumption of monomers, which is presented in Figure 3.44B, does not show a significant drop at the time when the molar mass increases. A direct correlation between the increase of the molar mass and the consumption of the monomers, like it was observed for the silica polymerization in the absence of polymers, is only obvious for the silica content of 750 ppm, which exhibits no lag-time. In case of 500 ppm and 400 ppm SiO_2 the monomer concentration decreases only slightly over the entire observation time. Regardless of the extremely weak variation of the monomer concentration we want to compare the lag-time in the presence of PEO, determined by means of the initial increase of the weight-averaged molar mass, with the lag-time obtained for the silica polymerization without PEO. Figure 3.45 compares the lag-time τ for all experimental conditions, applied in our experiments. A clear trend can be found: SiO_2 > SiO_2 + PEO > SiO_2 + Ca^{2+}+Mg^{2+} > SiO_2 + PEO + Ca^{2+}+Mg^{2+}. Additionally all these measurement series show a decreasing lag-time with increasing degree of supersaturation. At this point we have to state that it cannot be distinguished between a possible mechanistic influence of PEO on the oligomerization process of silica resulting in a decreased lag-time or an indirect influence of PEO on the lag-time, as PEO leads to an increase of the solubility limit and with that to a decrease of the degree of supersaturation.

In the following we want to compare the results for the weight-averaged molar mass and the monomer consumption obtained in the presence of PEO with the results from the reference experiments in the absence of PEO, this comparison is given in Figure 3.46 and Figure 3.47. The absolute values of the weight-averaged molar mass M_w lie several orders of magnitude higher in the presence of PEO than in case of the silica experiments without addition of PEO. Additionally these high values of weight-averaged molar mass are reached within a shorter time, if PEO is present in the solution. The monomer consumption at 750 ppm are comparable for all investigated conditions, the addition of 15 ppm PEO has no effect. We see a fast decrease of the monomer concentration without an appearance of a lag-time until the equilibrium concentration of 170 ppm is reached. At 400 and 500 ppm a clear influence of PEO can be constituted. Only a small amount of the initially available monomeric silica is consumed by the formation of silica particles, this is the more pronounced, the lower the initial silica concentration gets. At 500 ppm SiO_2 the monomer concentration is reduced to ~ 400 ppm during the entire experiment, corresponding to a decrease of about 16-17%. If the initial silica content amounts to 400 ppm we detect a decrease of about 6% to a final monomer concentration of ~ 380 ppm. Within

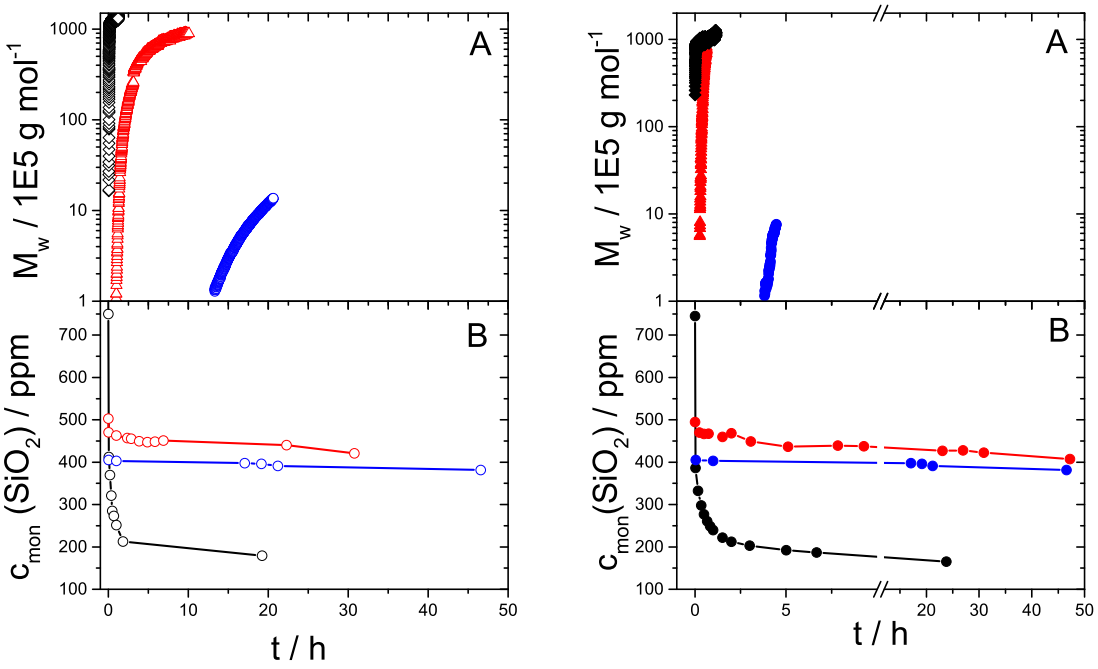

Figure 3.44.: Silica particle growth at pH 7 in the presence of 15 ppm PEO and at variable silica content: 400 ppm (○, ●), 500 ppm (△, ▲), 750 ppm (◇, ◆). Graph A shows the evolution of the weight-averaged molar mass obtained from SLS and graph B the consumption of the monomeric silica determined with the molybdenum blue method. Experiments in pure water (empty symbols) are presented on the left hand site and experiments in the presence of Ca^{2+}+Mg^{2+} (full symbols) on the right hand site.

the range of uncertainty of the measurement this is valid for the experiments in the absence as well as in the presence of Ca^{2+}+Mg^{2+}-ions. The reduced monomer consumption in the presence of such a low concentration of poly(ethylene oxide) shows its good performance in inhibiting the silica polymerization. The inhibition effect of PEO is based on the fact that at least 52.5% more monomeric silica remains in solution and is prevented from polymerizing. The bar chart in Figure 3.48 compares the final value for the concentration of monomeric silica at variable conditions. For SiO_2 contents of 500 ppm and lower PEO increases drastically the solubility limit of the amorphous silica. At concentrations as high as 750 ppm, PEO shows no effect any more, most likely the concentration of PEO is too low in relation to this high concentration of silica.

The trends for the weight-averaged molar mass in the presence of PEO showed higher mass values than for the reference experiments. Therefore also a considerably higher size of the particles is expected if PEO is present. Figure 3.49 compares the final values of the particle size in terms of the radius of gyration R_g for experiments with PEO

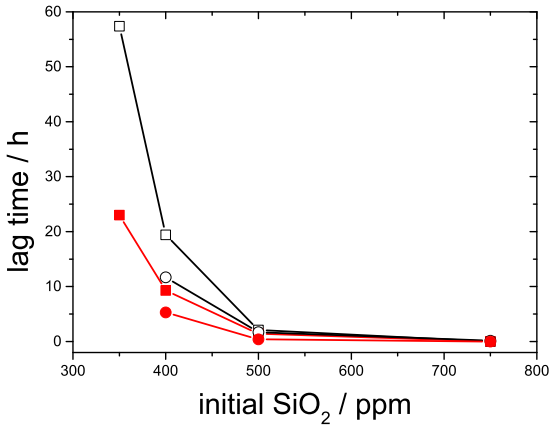

Figure 3.45.: Induction period depending on the initial silica concentration for silica polymerization at variable conditions: SiO_2 in pure water: (□), SiO_2 in pure water + 15 ppm PEO: (○), SiO_2 in water + 5 mM Ca^{2+}+Mg^{2+}: (■), SiO_2 in water + 15 ppm PEO + 5 mM Ca^{2+}+Mg^{2+} (●).

and in terms of the hydrodynamic radius R_h for the reference experiments. The silica particles formed in reference experiments exhibit particle sizes below 20 nm. These particles are formed via a monomer-addition mechanism (see Chapter 3.1.1 and 3.2). Only the sample with a silica content of 750 ppm in the presence of Ca^{2+}+Mg^{2+} has a particle size of 50 nm at the end of the measurement, due to the onset of particle-particle aggregation after a fast period of monomer-addition growth, as already discussed in Chapter 3.2. However, the addition of PEO leads to particle sizes above 150 nm.

Concerning the radius of gyration R_g determined for the experiments in the presence of PEO, two aspects have to be mentioned. (i) The values shown in Figure 3.49 are not necessarily describing the final size of the particles, as the particle formation was not finished when the last measurement was taken. (ii) In order to avoid a progressively ill-determined radius of gyration via the Guinier approximation the experimental data had to be cut-off, once the radius of gyration reached a value of ~ 200 nm. Deviations of the true radius of gyration and the one, evaluated via the Guinier approximation, are attributed to the fact that the Guinier regime is shifted to lower q, if the radius of gyration is increasing. Unfortunately, a static light scattering experiment is based on a fixed q-regime and with that the Guinier regime is escaping the q-regime of the present set-up with increasing particle size. The values of R_g shown in Figure 3.49 reflect only the size of intermediate agglomerates, as aggregation of the particles proceeds beyond the experimental observation time. One day after initiation of the experiment, the solutions with PEO even show a clearly visible flocculation. Unlike to the impact of PEO, the solutions of the reference experiments remain clear over weeks. In order to illustrate this a photography of one of the solutions in the absence and in the presence of PEO, respectively, is given in Figure 3.50.

From the literature it is known that low molecular weight PEO forms aggregates

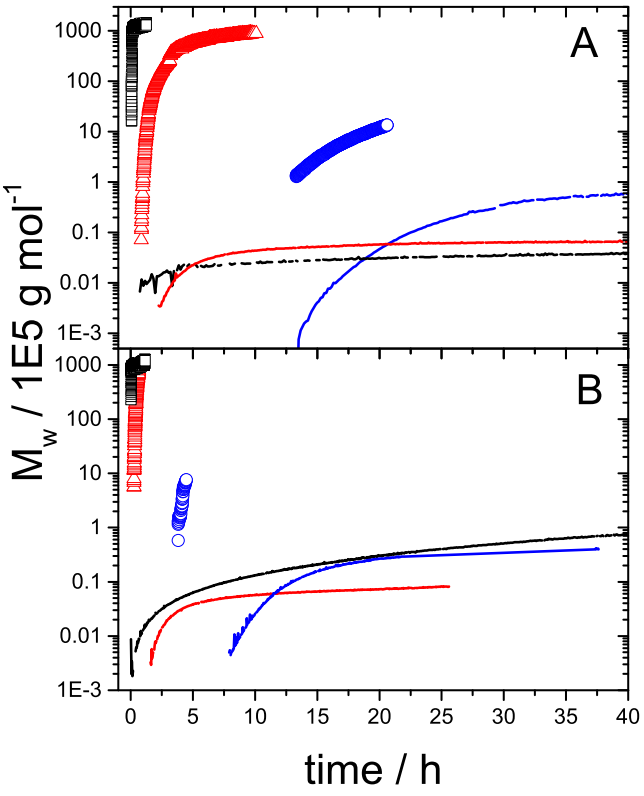

Figure 3.46.: Silica particle formation in terms of the weight-averaged molar mass M_w in water (A) and in the presence of 5 mM Ca^{2+}+Mg^{2+} (B). Empty symbols denote experiments in the presence of 15 ppm PEO, experiments in the absence of PEO are depicted as lines. The silica contents are 400 ppm (○, —), 500 ppm (△, —), 750 ppm (◇, —).

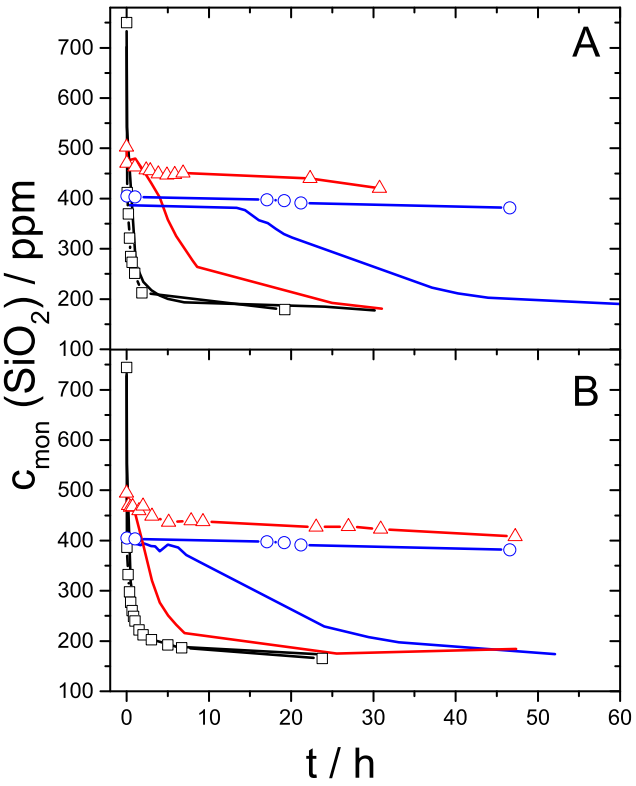

Figure 3.47.: Consumption of the monomeric silica depending on time determined via the molybdenum blue method. Graph A shows the results from experiments in water and graph B from experiments in the presence of 5 mM Ca^{2+}+Mg^{2+}. Empty symbols denote experiments in the presence of 15 ppm PEO and experiments in the absence of PEO are depicted as lines. The silica contents are 400 ppm (○, —), 500 ppm (△, —), 750 ppm (◇, —).

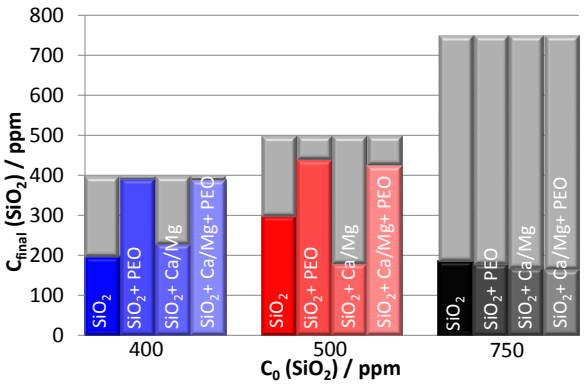

Figure 3.48.: Final values for the concentration of monomeric silica at variable conditions. The grey highlighted part corresponds to the amount of monomeric silica, which has been polymerized and incorporated into particles.

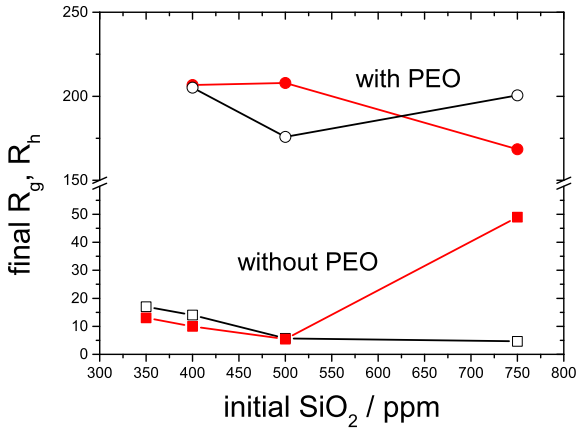

Figure 3.49.: Final size of particles formed via silica polymerization at pH 7 in terms of the hydrodynamic radius R_h (squares) or the radius of gyration R_g (circles) depending on the initial silica concentration. Empty symbols indicate experiments in pure water and full symbols indicate experiments in the presence of Ca^{2+}+Mg^{2+}. Experiments in the presence of PEO (circles, R_g) and experiments in the absence of PEO (squares, R_h).

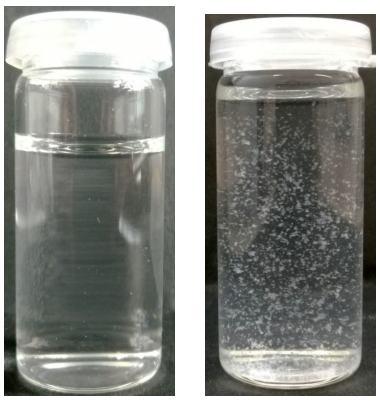

Figure 3.50.: Photography of the silica solutions under salt-free conditions 24 hour after initiation of the experiment in the absence (left) and in the presence of 15 ppm poly(ethylene oxide)(right).

in aqueous solution, due to hydrophobic interactions.[102] In order to compare the possible aggregates with the particles formed in the presence of silica, a solution of PEO (10000 g/mol) in pure water with a concentration of 1 g/mol has been also characterized via SLS. Figure 3.51 shows the corresponding Guinier plot. At low q-values the scattering curve shows a strong bending, which indicates the existence of large aggregates. A radius cannot be estimated, as the aggregates are much larger than 200 nm and therefore a precise Guinier approximation is not possible. In the higher q-regime the linear approximation gives a radius of gyration of R_g = 32.2 nm and a weight-averaged molar mass of M_w = 228000 g/mol, which is much higher than the value specified for the PEO sample. From this analysis we can conclude that PEO in pure water is present as aggregates with a broad size distribution. Although the PEO sample used for the present experiments with SiO_2 has a slightly lower molecular weight (M_w = 6550 g/mol) than the PEO sample analysed in Figure 3.51 by SLS, it is assumed that singular aggregates are also present in the mixture with SiO_2. In our experiments with SiO_2 + PEO we did not detect any significant net scattering signal during the induction period. Due to the very low concentration of PEO (15 ppm) in the mixture with SiO_2, these aggregates are either not present at all or cannot be detected.

For all initial silica contents in the presence of PEO a similar particle size is reached, although the available amount of silica is deviating drastically. With decreasing initial silica concentration a higher amount of silica remains in the solution as monomeric silica. If the particle size is similar, either much less particles are formed or the particles exhibit a significant smaller mass density.

Figure 3.52 depicts the correlation of radius of gyration and weight-averaged molar mass in order to provide information about the structure of the particles formed in the presence of PEO. It is a comparison of the trends in salt-free water and in the presence of Ca^{2+}+Mg^{2+}. With decreasing silica content the curves are shifted to lower mass values, which indicates that the mass density of the particles is decreasing. In pure water at silica contents of 400 and 500 ppm the correlation follows at least over one decade of mass val-

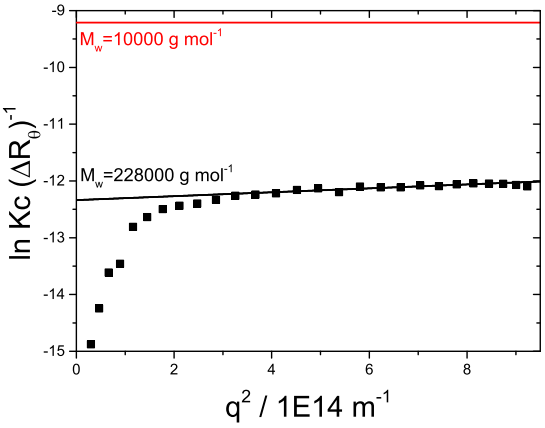

Figure 3.51.: Guinier plot evaluated from a SLS measurement of a solution of PEO in water with a concentration of 1 g/mol. The molar mass of PEO was specified with 10000 g/mol. The strong bending in the low q-regime indicates large aggregates. The linear approximation in the higher q-regime reveals a weight-averaged molar mass of 228000 g/mol. M_w is calculated with a dn/dc = 0.1317 cm^3/g[102]. The radius of gyration R_g is determined to 32.2 nm. The intercept corresponding to the specified weight-averaged molar mass of 10000 g/mol is indicated by the horizontal red line.

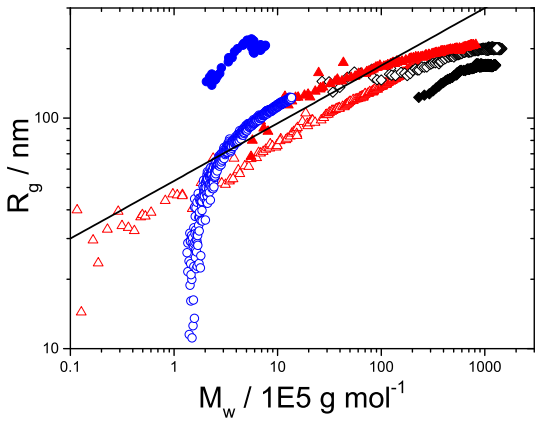

Figure 3.52.: Correlation of the radius of gyration and the weight-averaged molar mass for the silica particles formed at pH 7 in the presence of PEO: Empty symbols denote experiments in salt-free water and full symbols denote experiments in the presence of 5 mM Ca^{2+}+Mg^{2+}. The silica contents are 400 ppm (○, ●), 500 ppm (△, ▲) and 750 ppm (◇, ◆). The straight line denotes an exponent of $\alpha = 1/2$.

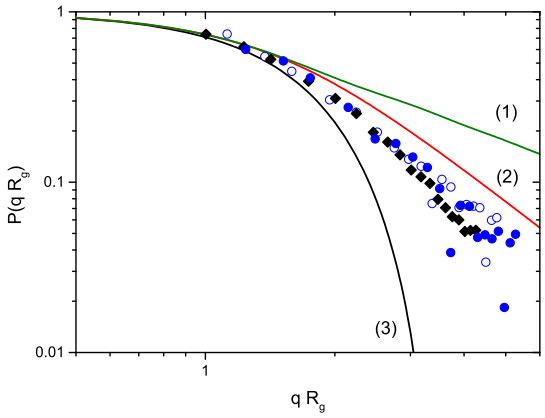

Figure 3.53.: Formfactor from the experiment with a silica content of 750 ppm (◆), taken at t = 0.8 h and 400 ppm (●), taken at t = 6.8 h in the presence of PEO and Ca^{2+}+Mg^{2+} and 400 ppm (○), taken at t = 30.3 h in the presence of PEO in pure water. Theoretical formfactors as $P(u = qR_g)$ for stiff rod[65] (1), a monodisperse coil[66] (2) and a monodisperse, compact sphere[67] (3).

ues a slope of ~ 1/4. An exponent of $\alpha = 1/4$ lies below the limiting cases of an ideal coil ($\alpha = 1/2$) and a compact sphere ($\alpha = 1/3$). If we consider the exponent under the assumption of a particle formation via a monomer-addition we have to multiply the determined exponent by a factor of two, as the weight-averaged mass values detected via light scattering describe the ensemble of growing particles and monomer units. Assuming this, we get an exponent of $\alpha = 1/2$, which would indicate a fractal-like structure. These fractal-like particles would grow by addition of small units to the fractals. All other experiments show no clear linear trend in the correlation of size and mass. For very high mass values the slope of the trends in the presence of Ca^{2+}+Mg^{2+} is decreasing with increasing mass. That means that the particle size remains constant, whereas the mass keeps increasing, indicating an increasing mass density or an increasing number of particles.

The determination of the structure-sensitive parameter ρ is not possible as the silica solutions with PEO have not been investigated via dynamic light scattering. Still, further information about the particle structure is available via the formfactor. Figure 3.53 represents the formfactor of the experiment with a silica content of 750 ppm and 400 ppm in the presence of PEO and Ca^{2+}+Mg^{2+} and a silica content of 400 ppm in the presence of PEO in pure water in comparison to the theoretical formfactors of a stiff rod, a monodisperse coil and a monodisperse, compact sphere. The experimentally obtained formfactors are very similar to the formfactor of a coil. Hence, the formfactor suggests also a fractal-like structure of the silica particles formed in the presence of PEO.

In Chapter 3.1.1 and 3.2 we could unambiguously show that silica forms homogeneous spherical particles with a size below 20 nm via a monomer-addition mechanism. Only in case of a silica content above 500 ppm in the presence of Ca^{2+}+Mg^{2+} a step-growth like agglomeration of the spherical particles to fractal-like domains sets in. The

silica polymerization is strongly influenced by the presence of PEO. Large fractal-like particles are growing in size and mass. This growth sets in after a lag-time which depends on the initial silica concentration and which is reduced in comparison to the lag-time observed in the absence of PEO. The existence of this lag-time is a hint that the particle formation depends on interactions between PEO and silica and that silica is possibly incorporated in these particles or co-aggregates with PEO, as an aggregation of PEO independent on the presence of silica should be time-independent.

Poly(ethylene oxide) shows a powerful inhibition effect for the silica polymerization. A relatively small concentration of 15 ppm PEO with a molar mass of 6550 g/mol is able to change the solubility limit of silica and stabilizes more than the twofold of the equilibrium concentration of monomeric silica in case of the absence of PEO in solution. In this way the amount of silica which is incorporated into amorphous silica is decreased. Thereby the inhibition effect is depending on the ratio of silica and PEO, as the effect gets weaker the higher the silica concentration gets.

However, the exact mechanism of the inhibition effect remains unknown. In general antiscalants can be divided by their functional features. Antiscalants with an inhibition function are able to prevent the precipitation of silicates, as they increase the solubility limit thereby maintaining a greater amount of silica in solution. A second feature is the dispersion function, in this case the antiscalant prevents agglomeration of silica particles and hence prevents surface attachment and deposition of silica particles. The investigation of the evolution of the monomeric silica in the presence of PEO indicates that the inhibition is based on an increase of the solubility limit of silica by PEO. Possibly the ether-groups of PEO act as proton acceptors and can form a hydrogen bond with monomeric silica, higher silica oligomers or even small particles of amorphous silica. Accordingly, the entire PEO backbone can be decorated with silica. However, for the water-treatment industry poly(ethylene oxide) is not a suitable antiscalant, as the PEO-silica particles undergo flocculation (see Figure 3.50, right hand site), eventually leading to depositions.

Concerning the particle structure it is not possible to interpret the data from SLS in a clear way. The correlation of R_g with M_w reveals no distinct linear dependency except for silica contents of 400 and 500 ppm in salt-free solution. Only the consideration of the formfactor indicates that the particles have a fractal-like structure, as the formfactor is similar to that of a Gaussian coil[66].

3.7.2. Influence of Poly(acrylic acid)

Poly(acrylic acid) (PA) has been used as a model polymer in order to investigate the influence of anionic polyelectrolytes on the silica particle formation. Solutions with a silica concentration of 500 ppm or 750 ppm silica, a concentration of 50 ppm poly(acrylic acid) and 5 mM Ca^{2+}+Mg^{2+} has been analysed via time-resolved DLS and SLS. In addition, the monomeric silica has been monitored via the molybdenum blue method and the resulting particles are characterized by means of scanning electron microscopy. Preparation of the solutions has been performed according to the descriptions in Chapter 2.5. After the pH adjustment of the aqueous silica solution, 5 ml of a salt stock solution with a concentra-

tion of $[Ca^{2+}]+[Mg^{2+}]$=0.2 M at a ratio of Ca : Mg = 4 : 1 is added. Subsequently a stock solution of poly(acrylic acid) in water is added, yielding a concentration of 50 ppm PA in the sample. A solution without SiO_2 but with a concentration of 50 ppm poly(acrylic acid) and a concentration of 5 mM Ca^{2+}+Mg^{2+} served as an additional reference experiment (PA-reference).

Figure 3.54A compares the weight-averaged molar mass obtained from SLS. Unfortunately, consideration of the weight-averaged molar mass bears a few drawbacks. The composition of the particles formed under the investigated conditions is unknown. We cannot say whether the entire silica or just a fraction of silica, present in the solution, is incorporated into the PA-particles or whether silica particles are only formed independent of the PA-particles, following the same mechanism as if no PA would be present. Therefore neither the exact mass concentration of the growing particles is known nor the ratio of the two components PA and SiO_2 and all values of the weight-averaged molar mass are apparent and depend on the mass concentration and the dn/dc used for their calculation. The mass values shown in Figure 3.54A have been calculated based on the PA concentration in case of the PA-reference experiment. In case of the experiments with PA and SiO_2 the initial concentration of silica was used (c_0 = 500 or 750 ppm). That means, that the polymer concentration was neglected for the experiments with the mixture of silica and PA. This is an acceptable approach as the fraction of PA was small in relation to the silica concentration. We also have to concede that by using the initial silica concentration for the calculation of M_w this M_w is a weight-average of monomers and SiO_2 polymers in case of a monomer-addition process.

Noteworthy, the mass values are lower for experiments with mixtures of SiO_2 and PA than for the PA-reference and the mass is even further decreased if the silica concentration is increased. This suggests that the more silica is present in the solution, the lower the detectable scattering intensity gets, whereas the corresponding evolution of the size of the particles is comparable for all experiments (Figure 3.55). This result is counterintuitive. If the silica content is increased and particles of the same size are always generated we would expect that a higher particle concentration would result in a higher weight-averaged molar mass, as more particles are formed.

The phenomenon of a decreasing intensity with increasing concentration could be explained by a negative refractive index increment of either NaPA or SiO_2. However, measurement of the refractive index increment of poly(acrylic acid) in pure water gave a dn/dc-value of 0.158 cm^3/g. The dn/dc-value of silica in pure water has been determined to 0.454 cm^3/g, so that a negative dn/dc of the mixture of PA and silica in water is very unlikely. Unfortunately dn/dc of a mixture of poly(acrylic acid), silica and $CaCl_2/MgCl_2$ could not be measured due to the particle formation, which would distort the measurement of the refractive index increment. It must be assumed that the decreasing weight-averaged molar mass with increasing silica content has to have its origin in the mechanism of particle formation. But at the moment this issue cannot be explained in a satisfactorily way.

The consumption of the monomeric silica is shown in Figure 3.54B, the trends of the experiments with 500 ppm and 750 ppm SiO_2 in the presence of PA are compared with the trends from experiments with the same silica content in the absence of PA. All

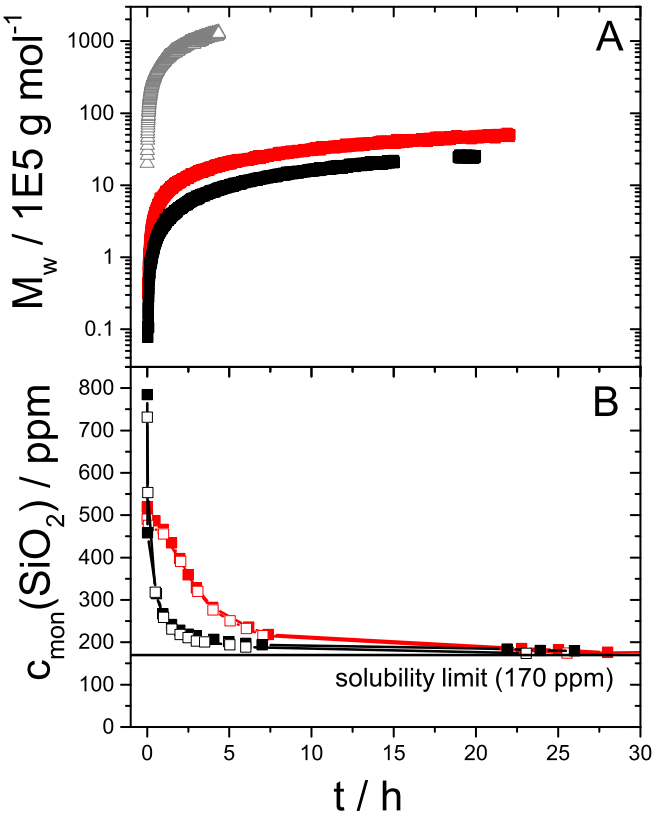

Figure 3.54.: Particle formation depending on time in a solution of 500 ppm (■) and 750 ppm (■) SiO_2 with 50 ppm PA and a concentration of 5 mM Ca^{2+}+Mg^{2+} in terms of the weight-averaged molar mass (A) (M_w is calculated with $c_{0,Si}$=500 ppm or 750 ppm, $(dn/dc)_{Si}$ = 0.454 cm^3/g). As a reference (△) the measurement of a solution containing 50 ppm PA and 5 mM Ca^{2+}+Mg^{2+} (M_w is calculated with $c_{0,PA}$ = 50 ppm, $(dn/dc)_{PA}$ = 0.158 cm^3/g) is shown. Graph B shows the consumption of the monomeric silica in the presence of PA (■, ■) compared with results in the absence of PA (□, □). All experiments have been performed under salt-conditions.

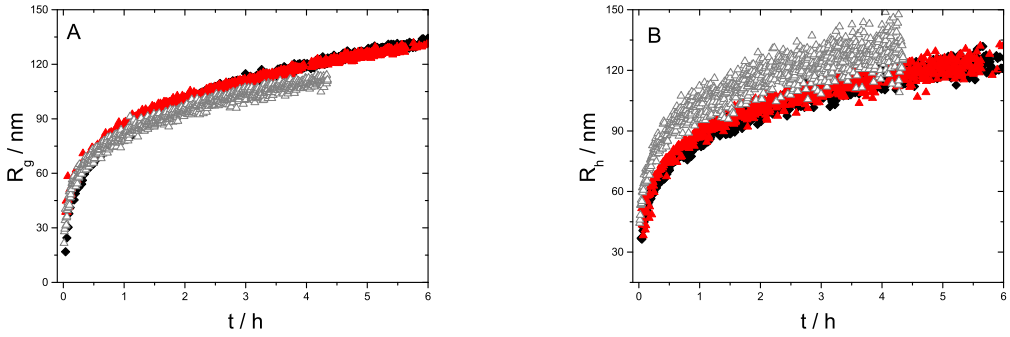

Figure 3.55.: Size of silica particles in the presence of Ca^{2+}+Mg^{2+} and PA in comparison to the reference solution (PA and Ca^{2+}+Mg^{2+}). (A) Radius of gyration R_g as a function of time; (B) hydrodynamic radius R_h as a function of time. The symbols denote the following systems: 500 ppm SiO_2 in the presence of 50 ppm PA and 5 mM Ca^{2+}+Mg^{2+} (■), 750 ppm SiO_2 in the presence of 50 ppm PA and 5 mM Ca^{2+}+Mg^{2+} (■), reference solution with 50 ppm PA and 5 mM Ca^{2+}+Mg^{2+} (△).

measurements have been performed in the presence of Ca^{2+}+Mg^{2+}. For both silica contents the trends for the monomer consumption are almost identical in the presence and in the absence of PA, therefore an influence of PA on the monomer concentration can be excluded.

It is known that poly(acrylic acid) in dilute solution is specifically interacting with divalent cations like calcium and magnesium. Schweins et al.[103,104] and Lages et al.[105] investigated the behaviour of poly(acrylic acid) in the presence of calcium ions and observed an aggregation of collapsed spherical coils to compact sphere-like structures. A light scattering measurement of the PA-reference solution shows the formation of particles reaching a size of R_g = 100 nm at the final experimental time, suggesting particle growth (see Figure 3.55). The final hydrodynamic radius is with ~ 135 nm slightly larger than R_g. The ratio ρ of the radius of gyration and the hydrodynamic radius reveals information about the particle structure and is given in Figure 3.56 as a function of time for the PA-reference measurement and the measurement with the mixture of silica and PA. As the data for the hydrodynamic radius in case of the PA-reference is quite noisy, the ρ-value exhibits fluctuations between ρ = 0.7 – 0.95. The theoretical ρ-value for a compact sphere is 0.77. Hence, the PA-reference in the presence of Ca^{2+}+Mg^{2+} indicates also compact spherical structures for poly(acrylic acid) in line with the findings of Schweins[103,104] and Lages[105].

For the experiments in the presence of silica we can observe the formation of particles with a very similar size compared to that observed in the absence of silica. Furthermore also the increase in size is comparable. Only a small difference is obvious between pure PA and the mixture of PA and SiO_2, the radius of gyration (see Figure 3.55A) of the particles is slightly larger and the hydrodynamic radius (see Figure 3.55B) is slightly smaller in case of the experiments with mixtures of PA and silica. This is also reflected in

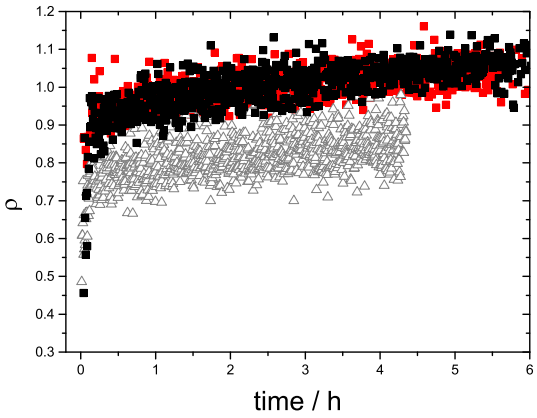

Figure 3.56.: Shape-sensitive factor $\rho = R_g/R_h$ as a function of time for the following experiments: 500 ppm SiO_2 in the presence of 50 ppm PA and 5 mM Ca^{2+}+Mg^{2+} (■), 750 ppm SiO_2 in the presence of 50 ppm PA and 5 mM Ca^{2+}+Mg^{2+} (■), PA-reference with 50 ppm PA and 5 mM Ca^{2+}+Mg^{2+} (△).

the structure-sensitive parameter $\rho = R_g/R_h$ (Figure 3.56). Particles formed in a solution with PA, silica and Ca^{2+}+Mg^{2+} exhibit with $\rho \sim 1.0$ a higher value than observed for the pure PA-particles induced by the presence of Ca^{2+}+Mg^{2+}. As a ρ-value of 0.77 is the lowest possible value describing compact structures, a higher value is connected to structures with a lower compactness. A more expanded structure like a unperturbed Gaussian chain adopts values close to 1.3. From these results we conclude that the hybrid PA-SiO_2 particles are slightly less compact than pure PA-particles.

A consideration of the formfactor of the particles at the end of the experiment confirms the previous results about the particle structure. Figure 3.57 shows the formfactor of the particles formed in the PA-reference solution and in a solution of 500 ppm silica, 50 ppm PA and 5 mM Ca^{2+}+Mg^{2+} in comparison to the theoretical formfactor of a stiff rod[65], a monodisperse coil[66] and a monodisperse compact sphere[67]. In agreement with the previous results from the structure-sensitive ratio ρ, the formfactor of the experiment in the absence of SiO_2 is slightly closer to the formfactor of a sphere than the particles with SiO_2. However, both trends led us assume that the structure of the particles is close to that of a compact, sphere.

An analysis of the correlation functions via a bi-exponential fit should provide more information about this issue. In case of a simultaneous formation of independent silica particles and PA-particles we should observe two species with different particle sizes by means of a bi-exponential fit large PA aggregates and small SiO_2-spheres. The analysis is performed in analogy to the process already described in Chapter 3.4. Exemplarily the fit was performed to the experimental data of the sample with a silica content of 500 ppm, a PA concentration of 50 ppm and a concentration of 5 mM Ca^{2+}+Mg^{2+}. The results according to Equation 3.2 are shown in Figure 3.58. The two particle species identified by the time-dependent hydrodynamic radius and the corresponding count rate determined

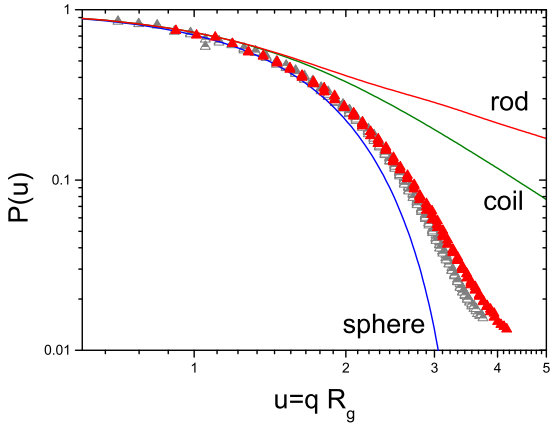

Figure 3.57.: Formfactor taken at the end of the experiment with a silica content of 500 ppm in the presence of PA and Ca^{2+}+Mg^{2+} (▲) and of the PA-reference (50 ppm PA and Ca^{2+}+Mg^{2+}) (△). Theoretical formfactors as $P(u = qR_g)$ for a stiff rod[65], a monodisperse coil[66] and a monodisperse, compact sphere[67].

via the bi-exponential fit are close to each other and show very similar trends. A second species with a smaller hydrodynamic radius than the PA-particles, which exhibits a final radius of ~ 120 nm, cannot be identified. If de facto the correlation function describes only one particle mode, the bi-exponential fit forces the two particle fractions to be so close to each other that they virtually overlay. In comparison to the trend of the hydrodynamic radius evaluated by means of the cumulant fit $R_{h,cum}$ the analysis with the bi-exponential fit shows a higher fluctuation of R_h. However, the entire experimental data is used for the fitting, which includes also the parts of the correlation function with high fluctuations and possible artefacts. This can lead to higher deviations. Neglecting the strong fluctuations of R_h from the bi-exponential fit, it can be assumed that the trends of the size based on the cumulant analysis and the bi-exponential fit are comparable. Thus a parallel, independent growth of the silica particles beside the formation of the PA-particles can be excluded. The analysis of the correlation functions led to the assumption that the observed particles are a hybrid material of poly(acrylic acid) and silica.

If we assume that the formed particles are composed of silica and PA, we can correct the concentration which is used for the calculation of the weight-averaged molar mass accordingly. The scattering intensity ΔR_θ has to be related to the sum of the concentration of PA (c_{PA} = 50 ppm) and the concentration of silica $c_{part,Si}$ (see Equation 3.1), corresponding to the actual amount of silica, which has been already undergone condensation reactions and are not detectable via the molybdenum blue method. Also the dn/dc value has be corrected and is calculated as the sum of the refractive index increment for PA and silica weighted by the corresponding mass fraction contributing to the actual mass concentration of the hybrid particles ($c_{PA} + c_{part,Si}$), resulting in a contrast factor $K_{PA,Si}$ corresponding to the hybrid particles. Figure 3.59 shows the evolution of

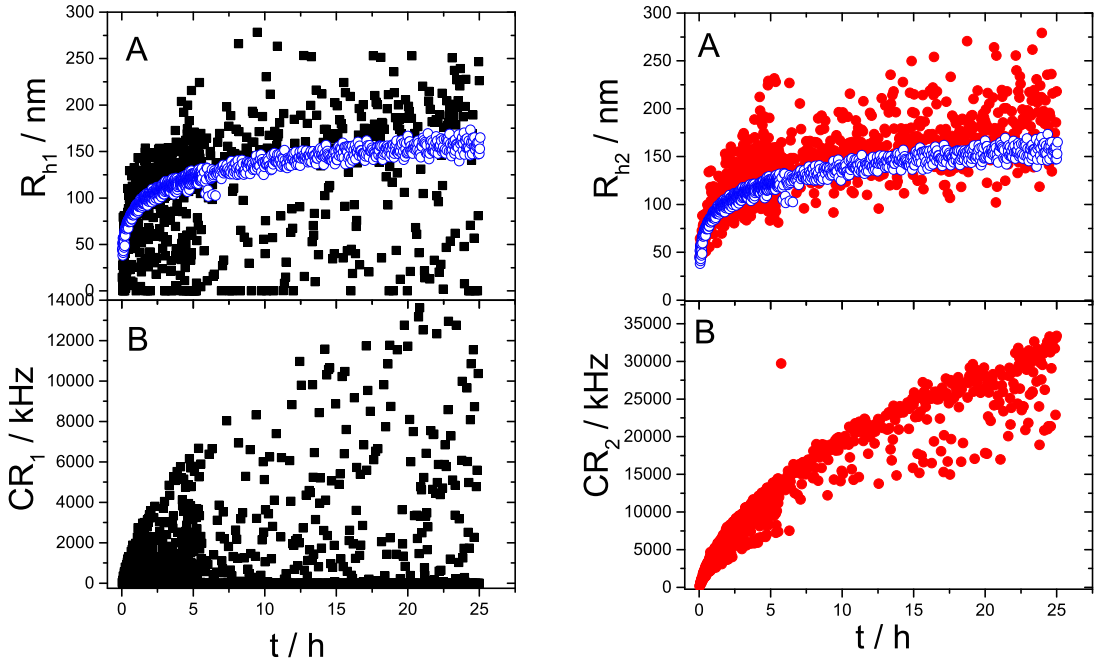

Figure 3.58.: Results of the bi-exponential fit according to Equation 3.2 to the correlation functions detected at scattering angle of $\theta = 20°$ of the experiment with the composition: 500 ppm SiO_2, 50 ppm, 5 mM Ca^{2+}+Mg^{2+}. **Left**: Hydrodynamic radius R_{h1} (A) and the corresponding count rate CR_1 (B) of particle species 1 (■). **Right**: Hydrodynamic radius R_{h2} (A) and the corresponding count rate CR_2 (B) of particle species 2 (●). For a comparison of the results of the bi-exponential fit with the results of the cumulant analysis, $R_{h,cum}$ determined via the cumulant analysis is additionally plotted (○) in (A).

the corrected weight-averaged molar mass for the silica contents 500 ppm and 750 ppm in the presence of Ca^{2+}+Mg^{2+} in comparison to the reference experiment with PA in the presence of Ca^{2+}+Mg^{2+}. In case of the reference experiment the scattering intensity ΔR_θ is related to the concentration of PA (50 ppm) and the dn/dc of PA (0.158 cm^3/g). The weight-averaged molar mass is still increasing with decreasing silica concentration. Since the size of the particles under all three conditions show a very similar evolution, with decreasing silica content a higher number of particles or more compact particles have to be formed. In case of the silica content of 750 ppm the trend of M_w has been only slightly shifted to higher mass values by using the corrected concentration (c_{PA} + $c_{part,Si}$). For the silica content of 500 ppm, consideration of the time-dependent increase of the silica concentration in the particles has a significant influence on the trend of the mass values. Within the first hour a fast increase in the mass is observed which proceeds parallel to the mass increase of the PA-reference experiment. This increase is followed by a decrease,

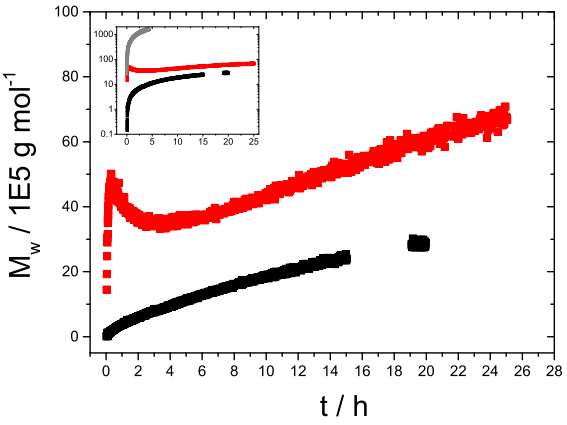

Figure 3.59.: Evolution of the weight-averaged molar mass calculated with the corrected concentration $c_{PA} + c_{part,Si}$ for the experiments with the silica content 500 ppm (■) and 750 ppm (■) SiO_2 in the presence of Ca^{2+}+Mg^{2+} and of PA. A comparison to the PA-reference (△) is shown in the inset graph.

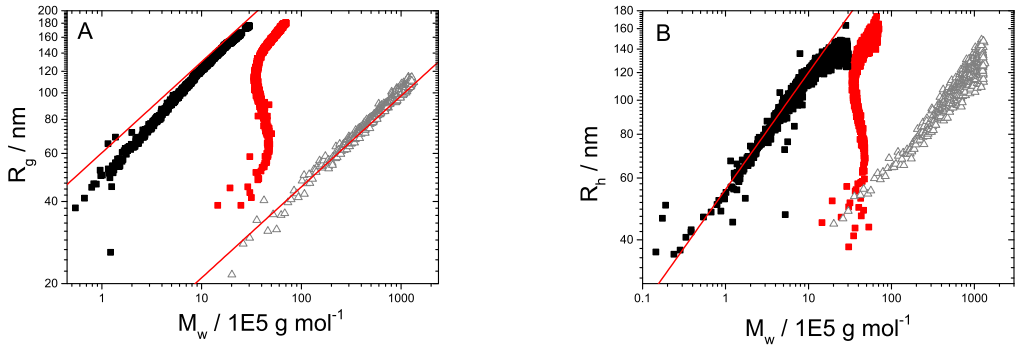

Figure 3.60.: Correlation of the particle size with the weight-averaged molar mass. (A) Radius of gyration R_g with M_w and (B) hydrodynamic radius R_h with M_w. Silica particle formation in the presence of 50 ppm PA and 5 mM Ca^{2+}+Mg^{2+}: 750 ppm SiO_2, $M_w = \Delta R_\theta / (K_{PA,Si}(c_{PA} + c_{part,Si}))$ (■) and 500 ppm SiO_2, $M_w = \Delta R_\theta / (K_{PA,Si}(c_{PA} + c_{part,Si}))$ (■). For a comparison the correlation of the reference experiment with 50 ppm PA in the presence of 5 mM of Ca^{2+}+Mg^{2+}, $M_w = \Delta R_\theta / (K_{PA} c_{PA})$ (△) is shown. The solid lines indicate a slope of 1/3.

a short plateau between 1 h and 3 h and a second increase of the mass, which proceeds linearly with time until the end of the measurement time.

The foregoing analysis concerning the ρ factor and formfactor revealed a compact, spherical structure. Correlation of the radius of gyration R_g and the hydrodynamic radius R_h with the corrected weight-averaged molar mass M_w (Figure 3.60) should give further insight. In case of the PA-reference experiment the correlation of R_g as well as of R_h with M_w exhibit a clear linear dependency with a slope of $\alpha = 1/3$, indicating compact, spherical structures. This is in line with the findings of Schweins[103,104] and Lages[105], who attributed this structure to the aggregation of collapsed, spherical coils. The correlation for the silica experiments in the presence of PA differ significantly from that of the PA-reference experiment and is influenced by the silica content.

At 750 ppm the correlation of R_g with M_w approaches the slope of $\alpha = 1/3$ in the regime of high mass values. For the lower mass values the slope is slightly steeper. Correlation of R_h with M_w follows the slope of 1/3 over the entire mass regime. Only, for the highest mass values the slope is decreasing, indicating, that the mass is increasing although the hydrodynamic radius remains nearly constant.

In comparison to results at 750 ppm the trend at 500 ppm is shifted to higher mass values. With increasing mass a small regime of a slope of 1/3 is followed by a period, in which the radius of gyration as well as the hydrodynamic radius is increasing and the mass is even decreasing. Noteworthy, this period coincides with the decrease of the concentration of monomeric silica. Possibly, a rearrangement of the PA-aggregates induced by the presence of amorphous silica particles lead to this extraordinary trend of the size with the mass. After this period of decreasing mass values similar to the behaviour of the PA-reference experiment and the experiments with a silica content of 750 ppm the trend of the correlation approaches a slope of 1/3. The interactions between poly(acrylic acid) and the divalent-cations lead to the aggregation of collapsed, spherical coils. This structure is also obtained in the presence of SiO_2. Although the particle size in terms of R_h and R_g are very similar for all measurement conditions the mass of the particles is decreasing the more SiO_2 is present in the solution. From this it can be concluded that the incorporation of silica into the particles is leading to a decrease of the compactness of the particles. This is confirmed by the fact that in case of a silica content of 500 ppm especially in the period, in which silica is transformed from monomeric silica to polymeric silica the size of the particles is increasing whereas the mass decreases.

A further proof for the existence of compact spherical particles are given by the analysis of the particles by means of scanning electron microscopy. For this purpose a solution of 750 ppm SiO_2 with 75 ppm PA and a concentration of 5 mM Ca^{2+}+Mg^{2+} have been prepared. At a later stage of the growth process the solution was investigated via light scattering, which yield a radius of gyration of R_g = 125 nm. Simultaneously a small portion of the solution was analysed with the scanning electron microscope, giving the SEM micrographs shown in Figure 3.61 and 3.62. The first micrograph (Figure 3.61) shows an overview on the sample. The close-up view focusses in the upper part almost equally dispersed, spherical particles. This upper part is delimited from the lower part by some large agglomerates of the spherical particles. Most likely these agglomerates have been formed during the drying process of the sample on the sample holder and were not

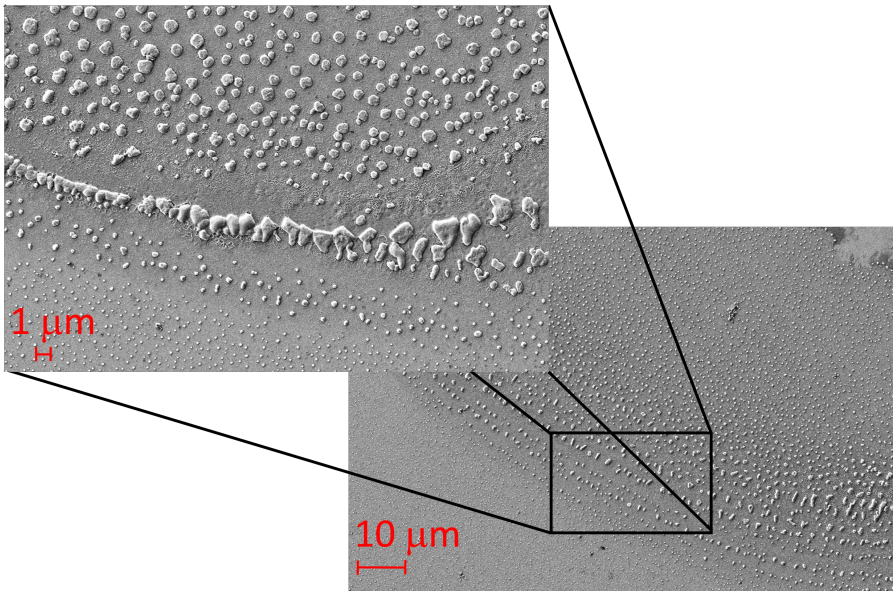

Figure 3.61.: SEM micrograph of a solution containing 750 ppm SiO_2, 75 ppm PA and 5 mM Ca^{2+}+Mg^{2+}, the characterization of the sample was performed ~ 3 h after initiation of the reaction via pH adjustment. The image shows an overview and a close-up of the sample. A ring structure of larger particles is visible. These larger structures maybe formed by coalescence of the smaller particles, during the drying procedure.

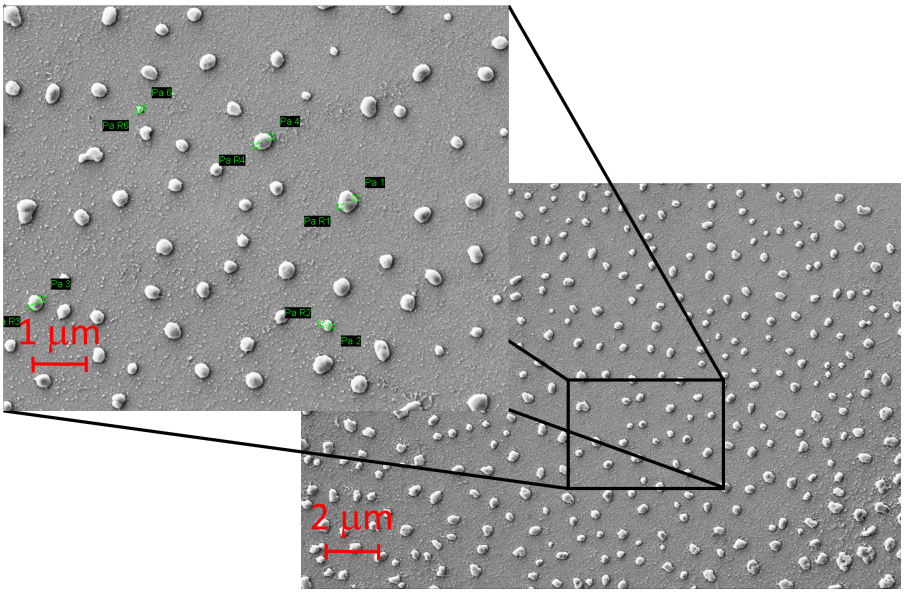

Figure 3.62.: SEM micrograph of a solution containing 750 ppm SiO_2, 75 ppm PA and 5 mM Ca^{2+}+Mg^{2+}. The characterization of the sample was performed ~ 3 h after initiation of the reaction via pH adjustment. The image shows a detailed view of the spherical structures.

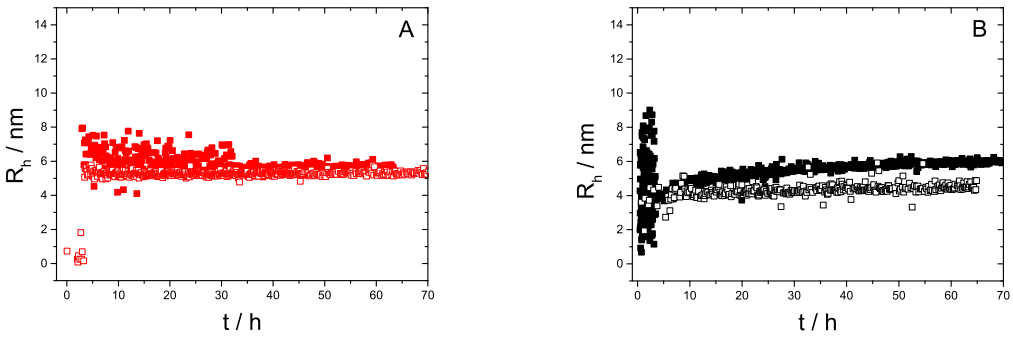

Figure 3.63.: Comparison of the evolution of the size of the particles with time in terms of the hydrodynamic radius R_h in pure water at two silica contents: 500 ppm (A) and 750 ppm (B). Empty symbols denote experiments in the absence of PA and full symbols in the presence of 50 ppm PA.

existent in solution. Figure 3.62 presents the spherical structures in more detail. Size measurements yield a size range of 250-345 nm in diameter, which is in line with the value of the radius of gyration obtained via light scattering (Figure 3.55, p.113).

A possible interaction between silica and PA in the absence of Ca^{2+}+Mg^{2+} is investigated by inducing the silica polymerization only in the presence of PA. The solutions contained a silica concentration of 750 ppm and 500 ppm and a PA concentration of 50 ppm. The evolution of the particle size is given in Figure 3.63 in comparison to results in the absence of PA. Discussion is limited to the hydrodynamic radius as the particles are to small (below 20 nm), to give reliable radii of gyration via static light scattering. The silica polymerization in pure water is unaffected by the presence of PA, the trends of the size are similar. The absolute hydrodynamic radius reached within the experimental time is slightly higher in the presence of PA. However, this effect could still be within the range of the experimental uncertainty.

An influence of PA on the silica polymerization becomes relevant only once Ca^{2+}+Mg^{2+} is present in the solution. In contrast to the silica particle formation in the absence of PA under salt conditions, the particle formation in the presence of PA shows no lag-time at a silica content of 500 ppm. A fast increase of the particle size and the particle mass can be observed for both silica contents if PA is present in the solution. However, the particles formed in the presence of PA reach a larger size and a higher mass. In the absence of PA under salt conditions we could observe two different particle structures depending on the silica content. At 500 ppm SiO_2 homogeneous spherical structures are formed. At a silica content of 750 ppm SiO_2 the threshold concentration for the particle-particle aggregation of these spherical particles is exceeded, resulting in fractal-like structures (see Chapter 3.2). In the presence of PA independent on the initial silica content the particles can be characterized by means of the formfactor and the structure-sensitive parameter ρ as compact, sphere-like structures.

The experiments on silica formation in the presence of poly(acrylic acid) has

shown that PA unlike to the results for poly(ethylene) oxide has no effect on the consumption of the monomeric silica. Hence, an inhibition of the silica polymerization by poly(acrylic acid) cannot occur by increase of the solubility limit of the amorphous silica. This could be a hint that at least the early stages of the silica polymerization follow the same mechanism independent on whether PA is present or absent. Particles formed in the presence of silica and PA reach significantly larger radii ($R_g \sim 135$ nm, $t = 6$ h) if simultaneously alkaline earth cations are present, which interact specifically with PA. The interaction with divalent cations leads to a chain collapse and to compact sphere-like PA-aggregates. Since beside these PA-aggregates no second species of a size below 10 nm can be determined, it is assumed that the small silica particles are incorporated into the aggregating matrix of PA chains. Therefore modulation of the silica polymerization by poly(acrylic acid) is based on a distribution of the small silica particles throughout the aggregates. The correlation trends of the size with the mass and the formfactor showed a decreasing mass density respectively a decreasing compactness of the hybrid aggregates with increasing silica content. These PA-silica aggregates are unlike to the PEO silica particles stable and do not flocculate. In Figure A.4 in the Appendix a photography taken several days after initiation of the reaction of the silica samples in the presence of PA and Ca^{2+}+Mg^{2+} is depicted. The solutions stay clear independent on the silica content.

A direct comparison of the weight-averaged molar mass, obtained in the absence and in the presence of PA, is connected with a few assumptions. In case of the mixture of silica and PA the exact mass concentration of the growing particles is unknown. The weight-averaged molar mass can only be calculated on the assumption whether PA and/or silica is incorporated into the particles. We showed here two possibilities to present the weight-averaged molar mass. In Figure 3.54 it was assumed that the particles consists only of silica and mass values are calculated using the initial silica concentration. In contrast in Figure 3.59 we assumed that the formation of PA-particles is very fast and that these particles act as template for silica. Silica oligomers or small silica particles are then time-dependently incorporated into these PA-particles. Whereas the incorporation of silica is correlating with the consumption of monomeric silica. This scenario leads to an increasing mass concentration of the particles and an increasing dn/dc of the particles depending on time, due to the increasing silica fraction in the particles with time.

3.7.3. Influence of Poly(acrylic acid)-2-acrylamido-2-methylpropane sulfonic acid (AA-AMPS)

As a third model polymer the influence of a copolymer of acrylic acid and 2-acrylamido-2-methylpropane sulfonic acid on the silica polymerization is investigated. This polymer exhibits a higher polarity due to the sulfonic groups and therefore is more hydrophilic and more acidic in comparison to poly(acrylic acid). Experiments have been performed with silica contents of 750 ppm and 500 ppm and a concentration of AA-AMPS of 50 ppm in the presence and in the absence of Ca^{2+}+Mg^{2+}. Like in case of the experiments with the two model polymers PEO and NaPA the preparation of the solution was performed according to the descriptions in Chapter 2.5 and 3.7.1. The pH adjustment of the silica so-

lution is followed by addition of the salt stock solution if needed and then followed by the addition of the AA-AMPS stock solution. The solutions have been investigated via time-resolved DLS and SLS, the molybdenum blue method and scanning electron microscopy. For a comparison a solution containing 50 ppm AA-AMPS and 5 mM Ca^{2+}+Mg^{2+} in water has been investigated. However, this sample showed no significantly higher scattering intensity than the solvent measurement, no formation of any particles could be observed. Figure 3.64 compares the silica polymerization in the presence of Ca^{2+}+Mg^{2+} under the influence of AA-AMPS with the corresponding experiments in the absence of AA-AMPS. The represented mass values (Figure 3.64A) have been related to the silica content ($Kc/\Delta R$ with $c = c_0 = 500$ ppm or 750 ppm). The concentration of AA-AMPS is neglected in this case. The addition of AA-AMPS leads to an increase of the weight-averaged molar mass in case of both silica contents. During the silica polymerization with and without AA-AMPS at 500 ppm the mass approaches a plateau value after a short time whereas at 750 ppm the mass keeps increasing during the experimental time, both with and without AA-AMPS. This is closely related to the lag-time observed at 500 ppm with and without the presence of AA-AMPS. As the inlet of Figure 3.64A illustrates, the lag-time is independent of the presence or the absence of AA-AMPS. Concerning the disappearance of monomers, only at 500 ppm SiO_2 an influence of AA-AMPS can be observed. The concentration of monomeric silica in a solution with AA-AMPS and 500 ppm SiO_2 decreases significantly slower than in a solution without AA-AMPS. In general silica polymerization at 500 ppm in the presence of AA-AMPS indicates the same behaviour as the experiment in the absence of AA-AMPS. An increase in the weight-averaged molar mass is only achieved when simultaneously monomeric silica is consumed. This is a strong hint for particle formation via monomer-addition.

For the evolution of the particle size, a similar behaviour can be monitored (see Figure 3.65). At 500 ppm the general trend of a short lag-time followed by a fast increase which approaches a plateau value is given independent of the presence or the absence of the polymer. Only the radius (R_h) lies 13% higher with AA-AMPS than without it. At a silica content of 750 ppm the evolution of the hydrodynamic radius in the presence and in the absence of AA-AMPS proceeds in the same way up to $t \sim 5$ h, from this time on the particles formed in the presence of AA-AMPS show a faster increase in their size. This onset of deviation between the two trends approximately coincides with the time when the monomer concentration approaches the equilibrium value. From the investigations on the system of silica in the presence of 5 mM Ca^{2+}+Mg^{2+} but in the absence of polymer (see Chapter 3.2) it is known, that at 500 ppm homogeneous, compact structures are formed via a monomer-addition mechanism, whereas at 750 ppm a step-growth like particle-particle agglomeration generates fractal-like structures.

A correlation of the size with the corresponding mass is expected to give details concerning the structure of the particles formed in the presence of AA-AMPS. Figure 3.66 shows the correlation of the hydrodynamic radius with the weight-averaged molar mass comparing the experiments in the presence and in the absence of AA-AMPS for both silica contents of 750 ppm and 500 ppm. The slope of the trends is independent of the presence or the absence of the polymer. At 750 ppm the size versus mass correlation follows a slope of 1/2 and at 500 ppm it goes with 1/6. A slope of 1/3 indicates compact,

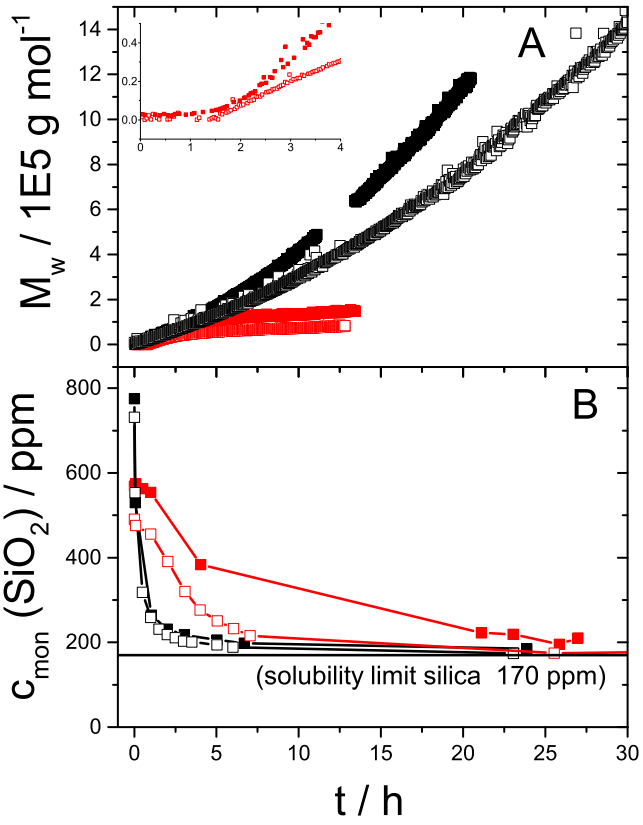

Figure 3.64.: Particle formation as a function of time in a solution of 750 ppm (■) and 500 ppm (■) SiO_2 with 50 ppm AA-AMPS and 5 mM Ca^{2+}+Mg^{2+} compared with results of the experiments with the same conditions but without the addition of AA-AMPS (□, □) in terms of the weight-averaged molar mass (A) and the consumption of the monomeric silica (B). The mass values are calculated based on the concentration of silica c_0

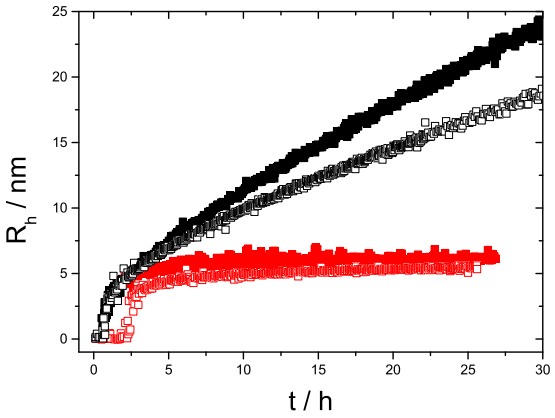

Figure 3.65.: Particle size as a function of time for the silica contents 750 ppm (■, □) and 500 ppm (■, □). All investigated solutions contained 5 mM Ca^{2+}+Mg^{2+}. Full symbols denote experiments in the presence of 50 ppm AA-AMPS and empty symbols denote experiments in the absence of AA-AMPS.

spherical particles and an exponent of 1/2 indicates fractal-like structures. In analogy to the discussion of the exponent in Chapter 3.1 we assume that the exponent of 1/6, which is too small to describe a certain topology stems from the fact, that M_w is a weight-average of growing particles and monomers. This leads to an exponent reduced by a factor of 2. Therefore this exponent indicates in analogy to the experiment without polymer homogeneous particles, which are formed during a monomer-addition process. This is nicely supported by the coincidence of monomer decrease and increase of the weight-averaged molar mass (see Figure 3.64). If we assume in the same way the presence of monomers and growing particles for the experiments at 750 ppm SiO_2, the exponent of 1/2 obtained from R_h versus M_w would correspond to a topology based exponent of 1, indicating rod-like structures. Since rod-like structures are very unlikely for silica particles, we conclude that the exponent obtained from the size versus mass correlation yields directly the topology based exponent, describing fractal-like structures.

The radius of gyration accessible via SLS could only be determined at a silica content of 750 ppm as in this case the particle size reaches values above 20 nm. In Figure 3.66 it is shown the correlation of R_g with M_w for the experiment at 750 ppm in the presence of AA-AMPS and Ca^{2+}+Mg^{2+}. Although the uncertainty is higher and the values are fluctuating strongly the general trend of 1/2 is also obvious for R_g. The fractal-like structure is confirmed by the corresponding shape-sensitive factor ρ, which is given in Figure A.6 in the Appendix, it fluctuates around $\rho = 1.2$.

Further evidence of the fractal-like structure of the particles formed at a silica content of 750 ppm is provided by the detection of a formfactor taken at 42.5 h after initiation, which is similar to the formfactor of a monodisperse coil (see Figure 3.67). The corresponding size of the particles was R_g = 98.1 nm. The SLS measurement giving the formfactor has been performed with a solution, which contained 750 ppm SiO_2, 5 mM

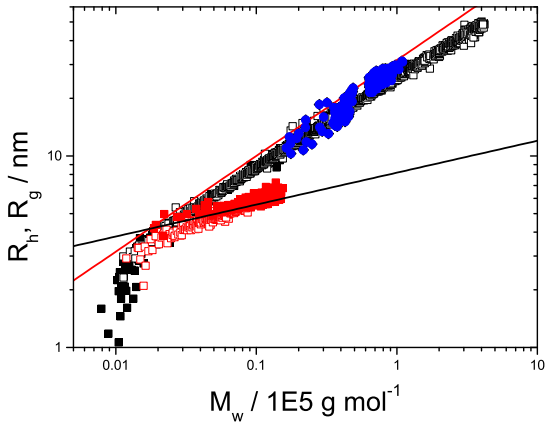

Figure 3.66.: Correlation of the particle size represented by the hydrodynamic radius and the weight-averaged molar mass for the experiments in the presence of AA-AMPS (■, ■) and in the absence of AA-AMPS (□, □). Two silica contents are compared 750 ppm SiO_2 (black) and 500 ppm SiO_2 (red). R_g versus M_w (●) is shown for the experiment with 750 ppm and AA-AMPS. All experiments have been performed in the presence of 5 mM Ca^{2+}+Mg^{2+}. The black line indicates a slope of 1/2 and the red line a slope of 1/6.

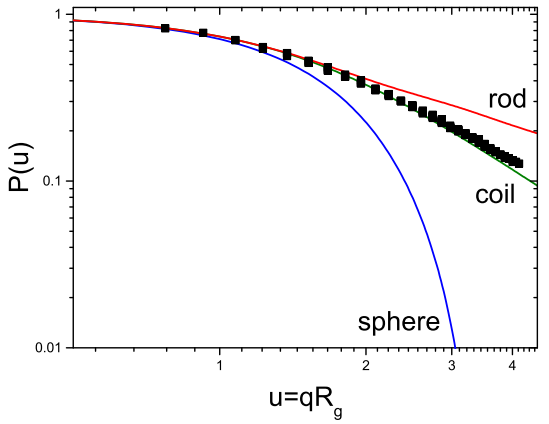

Figure 3.67.: Formfactor taken 42.5 h after initiation of an experiment with a silica content of 750 ppm in the presence of 75 ppm AA-AMPS and 5 mM Ca^{2+}+Mg^{2+} (■). The corresponding radius of gyration amounted to 98.1 nm. Theoretical formfactors as $P(u = qR_g)$ for a stiff rod[65], a monodisperse coil[66] and a monodisperse, compact sphere[67].

Ca^{2+}+Mg^{2+} and 75 ppm AA-AMPS. Although the polymer concentration is in this case higher than in case of the one discussed in Figure 3.66 at 50 ppm of AA-AMPS, the particle structures are comparable. This can be verified by a superposition of size versus mass correlation of the two measurements, which is given in Figure A.5 in the Appendix.

From the same sample used for the formfactor measurement a small portion was taken and characterized via scanning electron microscopy. The SEM micrographs (Figure 3.68) show evenly distributed branched or fractal-like structures. Some isolated sphere-like particles can also be observed. A detailed consideration of these sphere-like particles (Figure 3.68C) and a size analysis gives a variable diameter between 30 and 130 nm. The fluctuating size of these sphere-like particles can be a hint, that these structures do not correspond to those observed with SLS with a radius of gyration of R_g=98.1 nm, but rather may have been generated during the drying process of the sample. The SEM image suggests that the fractal-like structures evenly distributed over the entire sample corresponds to the fractal-like particles observed via light scattering. Due to the missing delimitation of the particles on the SEM sample holder a size analysis via SEM is not possible.

The addition of AA-AMPS has no significant effect on the silica polymerization in the presence of Ca^{2+}+Mg^{2+}. The structural and mechanistic features of the particles generated in the presence of AA-AMPS remain the same as in the absence of AA-AMPS. The time-dependent trends of the weight-averaged molar mass and the particles size are very similar. Small differences in M_w and R_h or R_g lie in the range of the experimental uncertainty. At 500 ppm SiO_2 compact, sphere-like particles are formed, since the correlation of the size with the mass shows the same characteristics as in the absence of AA-AMPS. Therefore we conclude that silica particles in the presence of AA-AMPS are also formed via monomer-addition of monomers or oligomers. Similarly at 750 ppm SiO_2 agglomeration of the spherical particles to fractal-like structures can be observed also in the presence of AA-AMPS. The fractal-like structure of the agglomerates is characterized via the size versus mass correlation, the formfactor and SEM micrographs.

Finally the effect of an addition of AA-AMPS on silica polymerization shall also be analysed if no Ca^{2+} and Mg^{2+} cations are present. Silica particles generated in pure water do not undergo agglomeration, as the negatively charged surface inhibits this process and no cations are present to screen the charges. For the case of silica polymerization in pure water, we also see no agglomeration if AA-AMPS is added to the solution. The characteristic quantities obtained via SLS and DLS and molybdenum blue method, weight-averaged molar mass, hydrodynamic radius and the consumption of monomeric silica for the silica polymerization in pure water in the presence and in the absence of AA-AMPS are given in Figure 3.69 and Figure 3.70. The evolution of the weight-averaged molar mass show very similar trends in the presence and in the absence of AA-AMPS. The disappearance of the monomers is significantly faster at 500 ppm with and without AA-AMPS. In close analogy to the mechanism observed without AA-AMPS under these conditions this could be connected with a faster nucleation. A faster nucleation would lead to more critical nuclei and with that to a higher number of growing particles. Since the amount of monomer, which is distributed to the growing particles, remains the same, the particles have a smaller final size. This would explain the slightly smaller particles

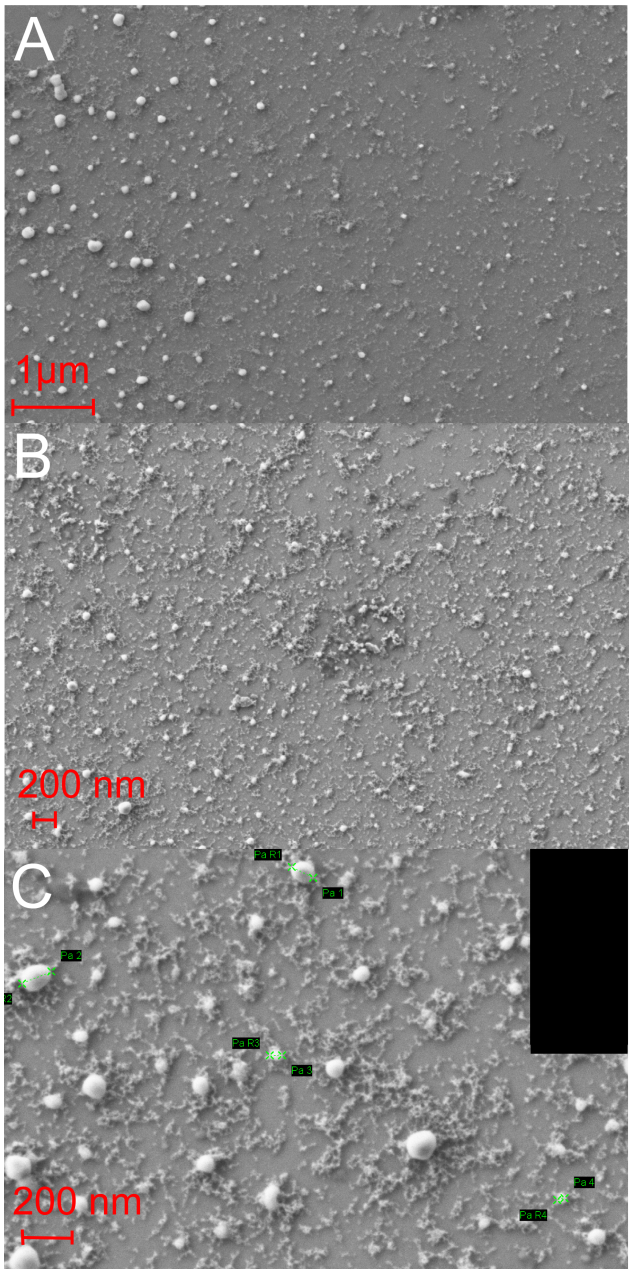

Figure 3.68.: SEM micrographs of particles stemming from the same sample used in Figure 3.67 (750 ppm SiO_2, 5 mM Ca^{2+}+Mg^{2+} and 75 ppm AA-AMPS). SEM samples were prepared from the solution 42.5 h after initiation of the reaction. Micrograph A shows an overview of the sample, B and C are more detailed close-ups.

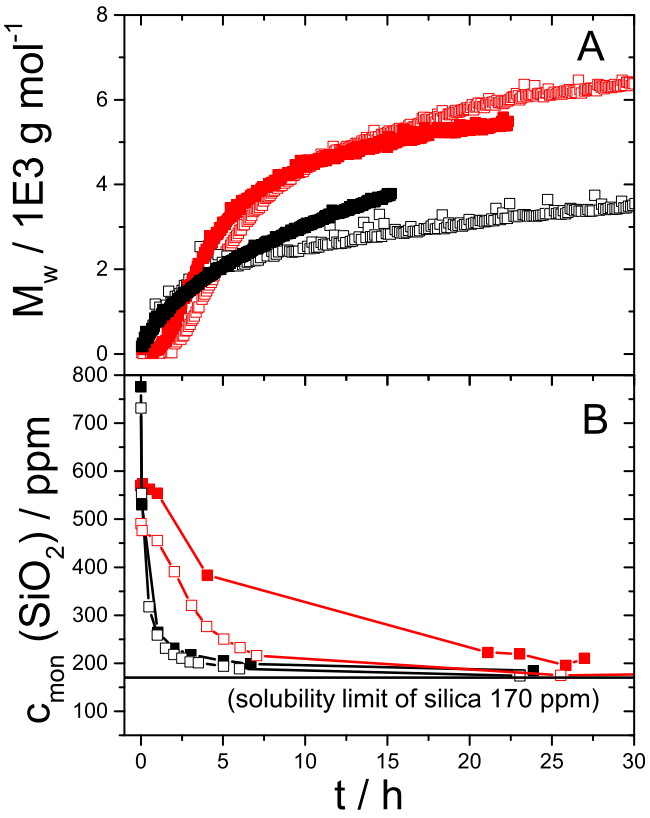

Figure 3.69.: Particle formation as a function of time in a solution of 750 ppm (■, □) and 500 ppm (■, □) SiO_2 with 50 ppm AA-AMPS compared to results of the experiments with the same conditions but without the addition of AA-AMPS in terms of the weight-averaged molar mass (A) and the consumption of the monomeric silica (B). Full symbols denote experiments in the presence of AA-AMPS and empty symbols denote experiments in the absence of AA-AMPS. The mass values are calculated based on the concentrations of silica c_0.

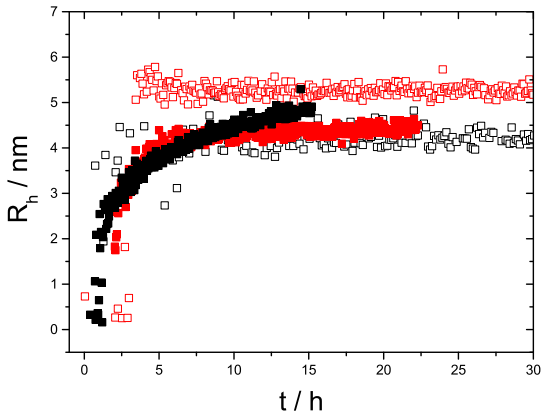

Figure 3.70.: Particle size as a function of time for the silica contents 750 ppm (■, □) and 500 ppm (■, □). Full symbols denote experiments in the presence of 50 ppm AA-AMPS and empty symbols denote experiments in the absence of AA-AMPS.

at 500 ppm SiO_2 in the presence of AA-AMPS in comparison to particles generated in the experiment in the absence of AA-AMPS. But in general we have to admit that these deviations still lie in the range of experimental uncertainty. At 750 ppm the consumption of the monomers is identical to the trend without AA-AMPS. The particle radius is with ~ 4 – 5.5 nm too small to provide more information about the particle structure via the radius of gyration or the formfactor. A correlation of the hydrodynamic radius with the mass is also not possible, as the range covered by the increase of R_h is too small.

The experiments have shown that the copolymer AA-AMPS has no significant influence on the silica polymerization. The general mechanistic features are not changed by the presence of AA-AMPS. Neither the formation of compact, sphere-like particles via a monomer-addition growth, nor the agglomeration of these compact particles is affected by AA-AMPS. Accordingly, there is evidence that AA-AMPS just does not interact in the formation of silica particles, at least at the applied concentration. An inhibition effect of AA-AMPS cannot be determined. The solubility limit of silica is not increased, which would be a sign for an inhibition mechanism, similar to PEO. Although AA-AMPS is known to be a good scale inhibitor for calcium phosphate, calcium carbonate and zinc scale and although it is commercially available for this purpose, our investigations have shown that it has no effect on silica formation at the applied concentration. Since the particle size is almost not at all influenced and also the aggregation of the silica particles is not inhibited, we have to suggest that AA-AMPS has also no dispersing effect on the silica particles.

4. Conclusions

The present study investigated the silica polymerization from supersaturated dilute aqueous solutions in the near neutral pH regime. The formation of silica particles have been monitored with the in-situ technique of time-resolved combined dynamic and static light scattering providing information about the particle mass in terms of the weight-averaged molar mass and the particle size in terms of the hydrodynamic radius as well as the radius of gyration. Structural features of the silica particles could be derived from the correlation of the particle size with the particle mass, the structure sensitive parameter ρ which is the ratio of R_g and R_h and the formfactor obtained by static light scattering. The consumption of monomeric silicic acid has been followed by UV-vis spectrometry revealing the molybdate-reactive silica according to the molybdenum blue method. The combination of these methods enabled us to monitor simultaneously the disappearance of the monomers and the growth of the silica particles and based on that data to calculate the actual concentration of growing particles.

Initiation of the silica polymerization was performed by acidification of an alkaline solution of sodium silicate ($Na_2H_2SiO_4 \cdot 8H_2O$) to pH 7 or pH 8. The silica content of the solutions covered a regime between 350 ppm and 3000 ppm. The influence of electrolytes on the process of silica polymerization has been investigated with experiments in the presence of 5 mM of a mixture of calcium chloride and magnesium chloride at a ratio of Ca : Mg of 4 : 1, simulating conditions of hard water and 10 mM sodium chloride, representing the most simple and inert type of salt. Independent of the conditions and the degree of supersaturation of the solutions an equilibrium concentration at $t = t_\infty$ of 170 ppm SiO_2 was determined via the molybdenum blue method.

Based on many studies from the last decades silica polymerization is assumed to follow a 3-step mechanism, identified by (1) a nucleation step, (2) a phase of particle growth and (3) the agglomeration of particles. Most of the former works derived these mechanistic features from the consumption of the molybdate-reactive silica and from an indirect determination of the silica particle size, based on the solubility of silica. Only a few recent studies[46,48] applied new scattering techniques to analyse directly the evolution of the growing species.

The analytical approach applied in the present study enabled us to confirm the 3-step mechanism with direct in-situ techniques and to discriminate unambiguously between the three different steps. In line with previous findings for low degrees of supersaturation a lag-time is observed, which is identified by the lack of particle formation due to a scattering intensity which is similar to the scattering intensity of the solvent and due to preservation of the monomer concentration. This lag-time is reduced by either a decrease of the initial silica concentration, corresponding to a decrease of the supersaturation, the presence of additional salt or the increase of the pH-value.

During the second step, we could unambiguously demonstrate that the loss of molybdate-reactive silica coincides with the formation of particles until the equilibrium concentration of silica is reached, thereby indicating a growth according to monomer-addition. The monomers may include monomeric silicic acid and oligomers thereof. From the characteristic power laws of $R_h \sim M_w^{1/6}$ given by the correlation of particle size (from DLS) with particle mass (from SLS) it could be concluded that in this second step homogeneous particles, most likely with spherical shape are formed. The final radius of these homogeneous particles lay in the range between 4.5 nm and 20 nm, with a value decreasing with increasing initial silica content. This suggests an increase of the nucleation rate represented by a faster monomer loss with increasing silica content.

Agglomeration as the third step sets in once the concentration of silica is large enough. It proceeds via a step-growth like particle-particle agglomeration. As extracted from SLS/DLS-data, the resulting agglomerates have a fractal dimension close to 2. The onset of particle agglomeration according to this step-growth process, which in pure water was first observed at a silica content of 2000 ppm is shifted to lower values by adding salt. Agglomeration takes place already at 750 ppm in the presence of both types of cations. Hence the presence of cations destabilizes particles with respect to particle-particle agglomeration. An increase of the pH value has a reverse effect, the particles are more stabilized and the threshold concentration for the particle-particle agglomeration is shifted above 2000 ppm. However, the presence of Ca^{2+}+Mg^{2+} and the presence of Na^{+} does not affect the fractal dimension of the growing intermediates. Even more strikingly, the presence of an additional salt does not even affect the nature of the constituting particles. Independent on whether salt is present or absent nucleation succeeded by growth via monomer-addition leads to particles with the same critical size of a few nanometers which then agglomerate to a unique type of fractal. Correlation of the particle size and the particle mass with time indicated that the particle-particle aggregation proceeds according to a diffusion-limited reaction and confirmed based on an alternative consideration of the experimental data once again the discrimination of the last two steps of the 3-step model.

The evolution of the weight-averaged molar mass describing the formation of particles during step 2 has been interpreted with a simple kinetic scheme, the NG-model, which consists of three reactions (1) precursor reaction, (2) nucleation/initiation and (3) particle growth by monomer-addition. This model could not only reproduce the evolution of M_w, but also the consumption of monomers at 350 ppm and 400 ppm, however, its performance turned out to get poorer at the higher silica contents of 500 ppm and 750 ppm. This was attributed to an increasing influence of the nucleation/initiation step as the silica content increases. The NG-model suffers from two points of criticism, (i) it does not allow to simulate a real equilibrium state, as the particles are not permitted to release monomers and (ii) the obtained rate constant of the precursor reaction varies over several orders of magnitude depending on the silica content. Therefore, the simple NG-model was refined with respect to two aspects, the variation of the size *n* of the nuclei which are formed in a simple reaction of order *n* and the explicit consideration of a monomer release step as depolymerization, leading to what is called the NGE-model. In order to provide suitable reference data, the NGE-model was first verified with the data collected in pure water. Several features demonstrated a better performance of the refined NGE-model. The fit

improved particularly in the regime of the lower silica contents. The rate constant of the precursor reaction could be successfully confined to a range extending only over one order of magnitude which is much better than the spread of the rate constant over eleven orders of magnitude observed for the NG-model. Further on, the NGE-model indicated a decrease of the nucleus size with increasing silica content in line with classical nucleation theory.

Taking advantage of such knowledge, which aside from being of fundamental relevance serves as excellent reference data, we investigated the influence of three model polymers on the formation of silica particles with the same analytical methods and complemented the results with a characterization of the generated particles via scanning electron microscopy. The investigations in the presence of poly(ethylene oxide), poly(acrylic acid) and poly(acrylic acid)-2-acrylamido-2-methylpropane sulfonic acid were confined to a silica concentration regime between 350 ppm and 750 ppm. The effect of electrolytes on the polymer assisted silica particle formation was studied by addition of a mixture of calcium and magnesium salt. The analysis provided information on the ability of these polymers to inhibit the silica polymerization and/or prevent the formation of silica depositions, which being considered as a candidate to act as a powerful antiscalant in the water-treatment industry. Poly(ethylene oxide) showed a strong inhibition of the polymerization reaction expressed as a considerable increase of the solubility limit of silica. However, poly(ethylene oxide) promotes also flocculation of silica particles, leading eventually to depositions. Experiments on the silica polymerization in the presence of poly(acrylic acid) revealed that PA has no significant effect on the monomer consumption of silica. It is known from literature [103–105], that if alkaline earth cations are present the interactions between cations and the PA-chains lead to a coil collapse and to an aggregation of the chains to compact, spherical clusters. Since our analysis of the mixed system also reveals only one particle species, we hypothesize that silica is rather incorporated into the aggregating matrix of PA chains, leading to hybrid aggregates. This outcome reveals PA as an antiscalant candidate due to its dispersing power on the silica particles. Unlike to the other two investigated polymers the presence of poly(acrylic acid)-2-acrylamido-2-methylpropane sulfonic acid had no significant effect on the process of silica particle formation or the consumption of monomeric silica independent on the salt conditions.

A. Appendix

A.1. DLS Data of Silica Solutions in Water at pH 7

Experiments on silica polymerization at 500 ppm and 750 ppm SiO_2 in water showed a constant particle size preceding a very fast increase. During the time of the constant particle size, the weight-averaged molar mass is still slightly increasing. The values of the hydrodynamic radius have been evaluated via the cumulant analysis. At this point we want to demonstrate the reliability of the cumulant fit by a comparison of the correlation-functions obtained by DLS measurements at a scattering angle of $\theta = 20°$ at different times. Figure A.1 summarizes some selected correlation functions presented as $I_I(\tau)$ versus τ for a silica content of 500 ppm and 750 ppm. The signal-to-noise-ratio, which is represented by the intercept of the correlation-function is increasing with time. Excluding the two earliest correlation-functions, which are of poor quality due to the very small scattering intensity in the beginning of the experiment, the slope of the correlation-functions is not changing. Therefore the results confirm the constant particle size already obtained by the cumulant fit.

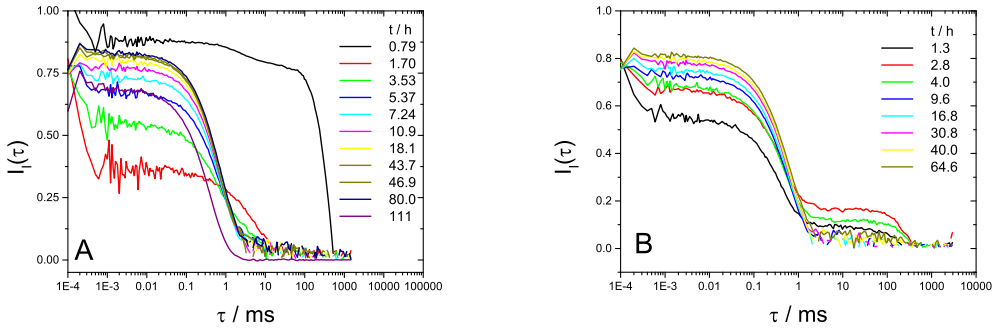

Figure A.1.: Intensity-time-correlation-function $I_I(\tau)$ at different times t obtained by DLS measurements at a scattering angle of $\theta = 20°$ of the sample with a silica content of 500 ppm (A) and 750 ppm (B) in water at pH 7. The exact time is indicated in the graph, respectively.

A.2. Derivation of the moments of the ensemble based on the reaction scheme of the NGE-model

The general definition of the kth moment of a particle distribution is

$$[C]^{(k)} = \sum_i i^k [C_i]. \tag{A.1}$$

Based on the fundamental three steps of the NGE-model (Equation 3.20), the reaction rate for a growing particle with the degree of polymerization i is given by

$$\frac{dC_i}{dt} = k_n[B]^n\delta_{in} + k_e[B][C_{i-1}](1-\delta_{in}) - k_e[B][C_i] - k_{-e}[C_i](1-\delta_{in}) + k_{-e}[C_{i+1}] \tag{A.2}$$

it is n the number of monomers, which can form a nucleus and δ_{in} the Kronecker-delta, which equals 0 if $i \neq n$ and 1 if $i = n$. Inserting Equation A.2 in Equation A.1 gives the following expressions for the zeroth, first and second moment.

$$\begin{aligned}
\frac{d[C]^{(0)}}{dt} &= \sum_{i=n}^{\infty} i^0 (k_n[B]^n\delta_{in} + k_e[B][C_{i-1}](1-\delta_{in}) - k_e[B][C_i] - k_{-e}[C_i](1-\delta_{in}) + k_{-e}[C_{i+1}]) \\
&= k_n[B]^n + k_e[B](\sum_{i=n}^{\infty}[C_{i-1}](1-\delta_{in}) - \sum_{i=n}^{\infty}[C_i]) - k_{-e}(\sum_{i=n}^{\infty}[C_i](1-\delta_{in}) - \sum_{i=n}^{\infty}[C_{i+1}]) \\
&= k_n[B]^n
\end{aligned} \tag{A.3}$$

$$\begin{aligned}
\frac{d[C]^{(1)}}{dt} &= \sum_{i=n}^{\infty} i^1 (k_n[B]^n\delta_{in} + k_e[B][C_{i-1}](1-\delta_{in}) \\
&\qquad - k_e[B][C_i] - k_{-e}[C_i](1-\delta_{in}) + k_{-e}[C_{i+1}]) \\
&= k_n[B]^n n + k_e[B](\sum_{i=n}^{\infty} \underbrace{i[C_{i-1}]}_{1}(1-\delta_{in}) - \sum_{i=n}^{\infty} i[C_i]) \\
&\qquad - k_{-e}(\sum_{i=n}^{\infty} \underbrace{i[C_i]}_{2}(1-\delta_{in}) - \sum_{i=n}^{\infty} i[C_{i+1}])
\end{aligned}$$

$$\begin{aligned}
&\text{with } i[C_{i-1}] = (i-1)[C_{i-1}] + [C_{i-1}] \text{ for term 1} \\
&\text{with } i[C_i] = (i-1)[C_i] + [C_i] \text{ for term 2}
\end{aligned} \tag{A.4}$$

$$\begin{aligned}
&= k_n[B]^n n + k_e[B](\sum_{i=n}^{\infty}(i-1)[C_{i-1}](1-\delta_{in}) + \sum_{i=n}^{\infty}[C_{i-1}](1-\delta_{in}) - \sum_{i=n}^{\infty} i[C_i]) \\
&- k_{-e}(\sum_{i=n}^{\infty}(i-1)[C_i](1-\delta_{in}) + \sum_{i=n}^{\infty}[C_i](1-\delta_{in}) - \sum_{i=n}^{\infty} i[C_{i+1}])
\end{aligned}$$

$$\begin{aligned}
&= k_n[B]^n n + k_e[B][C]^{(0)} - k_{-e}[C]^{(0)} \\
&= k_n[B]^n + [C]^{(0)}(k_e[B] - k_{-e})
\end{aligned}$$

$$\frac{d[C]^{(2)}}{dt} = \sum_{i=n}^{\infty} i^2 (k_n[B]^n \delta_{in} + k_e[B][C_{i-1}](1-\delta_{in}) - k_e[B][C_i] - k_{-e}[C_i](1-\delta_{in}) + k_{-e}[C_{i+1}])$$

$$= k_n[B]^n n^2 + k_e[B](\sum_{i=n}^{\infty} \underbrace{i^2[C_{i-1}]}_{1}(1-\delta_{in}) - \sum_{i=n}^{\infty} i^2[C_i])$$

$$- k_{-e}(\sum_{i=n}^{\infty} \underbrace{i^2[C_i]}_{2}(1-\delta_{in}) - \sum_{i=n}^{\infty} i^2[C_{i+1}])$$

with $i^2[C_{i-1}] = (i-1)^2[C_{i-1}] + 2i[C_{i-1}] - [C_{i-1}]$ for term 1
with $i^2[C_i] = (i-1)^2[C_i] + 2i[C_i] - [C_i]$ for term 2

$$= k_n[B]^n n^2$$

$$+ k_e[B](\sum_{i=n}^{\infty}(i-1)^2[C_{i-1}](1-\delta_{in}) + \sum_{i=n}^{\infty} 2i[C_{i-1}](1-\delta_{in}) - \sum_{i=n}^{\infty}[C_{i-1}](1-\delta_{in}) - \sum_{i=n}^{\infty} i^2[C_i]) \quad \text{(A.5)}$$

$$- k_{-e}(\sum_{i=n}^{\infty}(i-1)^2[C_i](1-\delta_{in}) + \sum_{i=n}^{\infty} 2i[C_i](1-\delta_{in}) - \sum_{i=n}^{\infty}[C_i](1-\delta_{in}) - \sum_{i=n}^{\infty} i^2[C_{i+1}])$$

$$= k_n[B]^n n^2 + k_e[B](\sum_{i=n}^{\infty} 2i[C_{i-1}](1-\delta_{in}) - \sum_{i=n}^{\infty}[C_{i-1}](1-\delta_{in}))$$

$$- k_{-e}(\sum_{i=n}^{\infty} 2i[C_i](1-\delta_{in}) - \sum_{i=n}^{\infty}[C_i](1-\delta_{in})$$

$$= k_n[B]^n n^2 + k_e[B](2[C]^{(1)} - [C]^{(0)}) - k_{-e}(2[C]^{(1)} - [C]^{(0)})$$

A.3. Fits with the NGE-model to Data in the Presence of Metal Cations

A more detailed overview on the fits to the data recorded in the presence of metal cations shall be given in Figure A.2 (in the presence of Ca^{2+}+Mg^{2+}-ions) and Figure A.3 (in the presence of Na^{+}). The figures compare the weight-averaged molar mass with the fit based on the NGE-model and show the evolution of the monomer concentration $[B]$ and the evolution of the number of particles $[C]^{(0)}$.

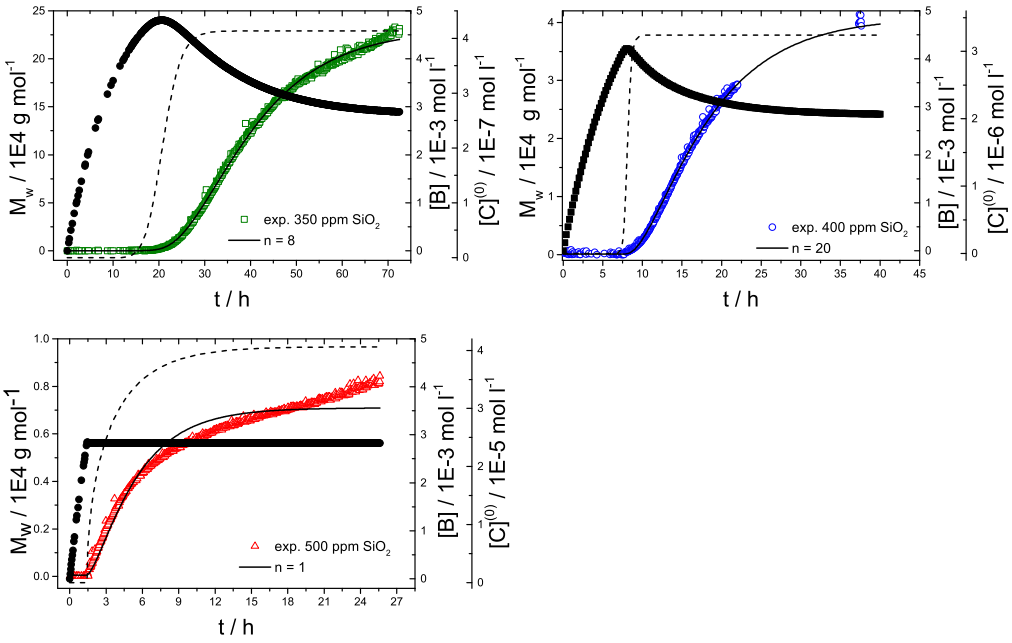

Figure A.2.: Comparison of the experimental weight-averaged molar mass M_w with the corresponding fits with the optimal nucleus size at variable silica contents in the presence of Ca^{2+}+Mg^{2+}-ions. The initial silica content and the nucleus size are indicated in the respective graph. The model calculations based on the NGE-model are represented in terms of the weight-averaged molar mass (—), the zeroth moment $[C]^{(0)}$ which is equal to the concentration of particles (– – –) and the concentration of active monomers $[B]$ (●).

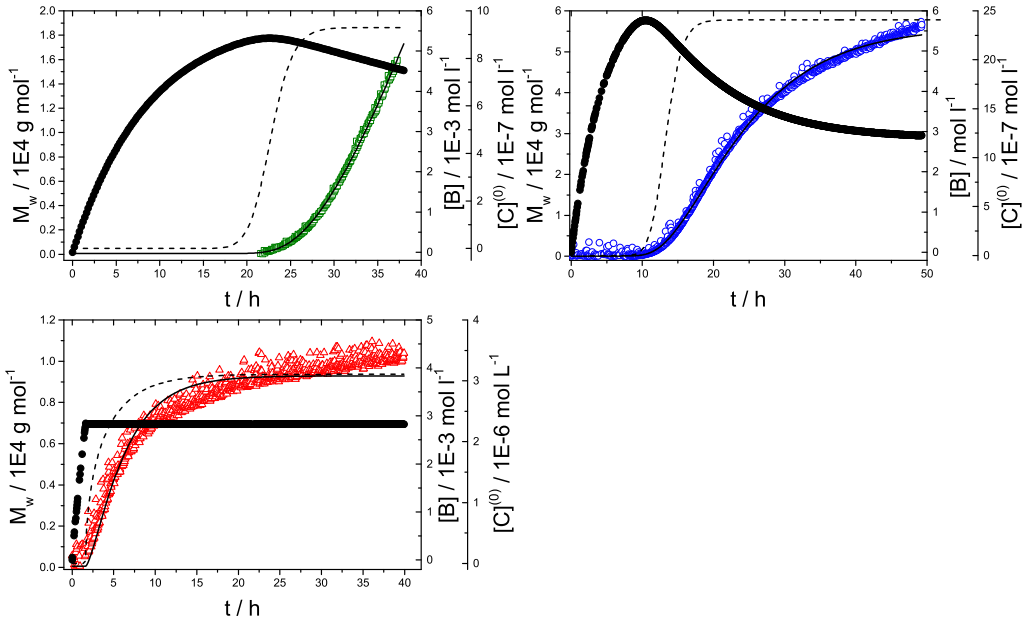

Figure A.3.: Comparison of the experimental weight-averaged molar mass M_w with the corresponding fits with the optimal nucleus size at variable silica contents in the presence of Na^+-ions. The initial silica content and the nucleus size are indicated in the respective graph. The model calculations based on the NGE-model are represented in terms of the weight-averaged molar mass (—), the zeroth moment $[C]^{(0)}$ which is equal to the concentration of particles (– – –) and the concentration of active monomers $[B]$ (●).

A.4. Silica Polymerization in the Presence of Polymeric Additives

A.4.1. Silica Polymerization in the Presence of PA

Figure A.4 shows a photography of the silica solutions in the presence of PA and Ca^{2+}+Mg^{2+} 24 h after initiation of the silica polymerization. Unlike to the solutions in the presence of PEO, no flocculation is observed.

Figure A.4.: Photography of the silica solutions in the presence of Ca^{2+}+Mg^{2+} and 50 ppm PA 24 hour after initiation of the experiment with 750 ppm (left) and 500 ppm (right) SiO_2.

A.4.2. Silica Polymerization in the Presence of AA-AMPS

Figure A.5 compares the correlation of the particle size and the particle mass of a silica solution in the presence of 50 ppm AA-AMPS with a silica solution in the presence of 75 ppm AA-AMPS. The curves overlay perfectly, this indicates that the structure of the particles in these two solutions is comparable and independent of the concentration of AA-AMPS.

As a further verification of the fractal-like structure of the particles formed in a solution with a silica content of 750 ppm in the presence of Ca^{2+}+Mg^{2+} and 50 ppm AA-AMPS Figure A.6 represents the shape-sensitive factor ρ as a function of time. ρ is fluctuating around 1.2, which is in line with the predictions of $\rho \sim 1.3$ for fractal structures or unperturbed linear chains.[71–73]

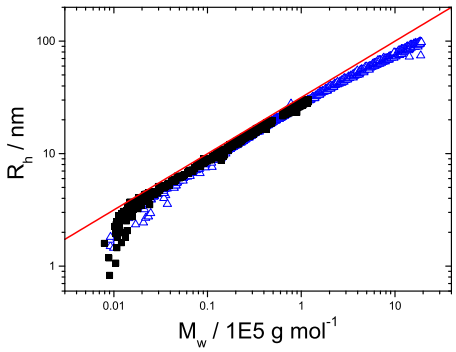

Figure A.5.: Correlation of the hydrodynamic radius and the weight-averaged molar mass for the experiments in the presence of AA-AMPS with the following conditions: 750 ppm SiO_2, 50 ppm AA-AMPS, 5 mM Ca^{2+}+Mg^{2+} (■) and 750 ppm SiO_2, 75 ppm AA-AMPS, 5 mM Ca^{2+}+Mg^{2+} (△).

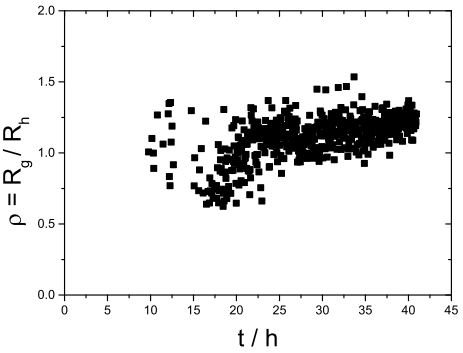

Figure A.6.: Shape-sensitive factor $\rho = R_g/R_h$ as a function of time, determined for the sample with 750 ppm SiO_2, 50 ppm AA-AMPS and 5 mM Ca^{2+}+Mg^{2+} (■).

A.5. List of Symbols

Symbol	Explanation
μ_{sol}	chemical potential of the solute
μ_{eq}	chemical potential at the equilibrium state
k	Boltzmann constant
T	temperature
a	chemical activity
a_{eq}	chemical activity at the equilibrium state
μ_{crys}	chemical potential of the solid phase
n	cluster size
n^*	critical cluster size
G	Gibbs free energy
G_{ex}	cluster excess free energy

ΔG^*	Gibbs free energy corresponding to the critical nucleus size
σ	surface tension
a	effective radius of the monomer unit
J	rate of nucleation
Z	Zeldovich factor
f^*	rate of attachment of monomers to nucleus
$P(n,t)$	concentration of embryos
k_n	rate constant of nucleation
D	diffusion coefficient
ΔR_θ	Rayleigh ratio at scattering angle θ
$R_{\theta,std}$	absolute scattering intensity of toluene, tabulated
$r_{\theta,sol}$	scattering intensity of the solution
$r_{\theta,solv}$	scattering intensity of the solvent
$r_{\theta,std}$	scattering intensity of toluene, measured
k_i	wave vector of the primary beam
k_s	wave vector of the scattered beam
q	scattering vector
n_{solv}	refractive index of the solvent
θ	scattering angle
K	contrast factor in a light scattering experiment
M_w	weight-averaged molar mass
R_g	radius of gyration
A_2	second virial coefficient
N_A	Avogadro constant
λ_0	wavelength of laser light in vacuum
n_{tol}	refractive index of toluene
$\frac{\partial n}{\partial c}$	refractive index increment
$P(q)$	formfactor
$g_I(\tau)$	intensity-time-autocorrelation function
$g_E(\tau)$	field-time-autocorrelation function
τ	lag-time
β	spacial coherence factor
Γ_i	time constant corresponding to species i
γ_i	weighting factor of species i
K_0	constant from cumulant analysis describing signal-to-noise ratio
K_1	constant from cumulant analysis, z-averaged time constant
K_2	constant from cumulant analysis, variance of time constant
D_z	z-averaged diffusion coefficeint
D_0	diffusion coefficient extrapolated to zero concentration
R_h	hydrodynamic radius
η	viscosity of the solvent
ρ	shape-sensitive factor
α	exponent of the size-mass correlation

c_{part}	mass concentration of growing particles
c_0	initial concentration of silica
$c_{mon}(t)$	actual monomer concentration
d_f	fractal dimension
$[A]$	concentration of the precursor
$[B]$	concentration of the active monomer
$[C_i]$	concentration of the polymer with degree of polymerization i
k_p	rate constant of the precursor reaction
$k_{p,back}$	rate constant of the reaction from active monomer to precursor
k_n	rate constant of the nucleation
k_e	rate constant of the growth reaction
k_{-e}	rate constant of the monomer release
δ_{in}	Kronecker delta
$[C]^{(k)}$	kth moment of the particle distribution
M_0	molecular weight of the monomer unit
χ^2	residuals of the kinetic fit to the experimental data

A.6. List of Abbreviations

Symbol	Explanation
SLS	static light scattering
DLS	dynamic light scattering
PEO	poly(ethylene oxide)
PA	poly(acrylic acid)
AA-AMPS	poly(acrylic acid)-2-acrylamido-2-methylpropane sulfonic acid
TEOS	tetraethylorthosilicate
TMOS	tetramethylorthosilicate
SAXS	small angle x-ray scattering
NMR	nuclear magnetic resonance
SEM	scanning electron microscopy
EDX	energy dispersive spectroscopy
RLCA	reaction-limited cluster-cluster aggregation
DLCA	diffusion-limited cluster-cluster aggregation
NG-model	model for nucleation and growth
NGE-model	model for nucleation and growth with equilibrium

B. Bibliography

[1] F. Liebau. *Structural chemistry of silicates: Structure, bonding, and classification*. Springer-Verlag, Berlin and New York, 1985.

[2] A. F. Holleman and N. Wiberg. *Lehrbuch der anorganischen Chemie*. De Gruyter Reference Global. De Gruyter, Berlin [u.a.], 102., stark umgearb. und verb. aufl. von Nils Wiberg edition, 2007.

[3] W. Stöber, A. Fink, and E. Bohn. Controlled growth of monodisperse silica spheres in the micron size range. *Journal of Colloid and Interface Science*, 26(1):62–69, 1968.

[4] C. J. Brinker and G. W. Scherrer. *Sol-Gel-Science- The Physics and Chemistry of Sol-Gel Processing*. Academic Press, Inc., London, 1990.

[5] D. J. Belton, O. Deschaume, and C. C. Perry. An overview of the fundamentals of the chemistry of silica with relevance to biosilicification and technological advances. *The FEBS journal*, 279(10):1710–1720, 2012.

[6] H. Boukari, J. S. Lin, and M. T. Harris. Probing the dynamics of the silica nanostructure formation and growth by saxs. *Chemistry of Materials*, 9(11):2376–2384, 1997.

[7] H. Boukari, G. G. Long, and M. T. Harris. Polydispersity during the formation and growth of the stober silica particles from small-angle x-ray scattering measurements. *Journal of colloid and interface science*, 229(1):129–139, 2000.

[8] T. Norisuye, M. Inoue, M. Shibayama, R. Tamaki, and Y. Chujo. Time-resolved dynamic light scattering study on the dynamics of silica gels during gelation process. *Macromolecules*, 33(3):900–905, 2000.

[9] D.L Green, J.S Lin, Yui-Fai Lam, M.Z.-C Hu, D. W. Schaefer, and M.T Harris. Size, volume fraction, and nucleation of stober silica nanoparticles. *Journal of colloid and interface science*, 266(2):346–358, 2003.

[10] S. Fouilloux, O. Taché, O. Spalla, and A. Thill. Nucleation of silica nanoparticles measured in situ during controlled supersaturation increase. restructuring toward a monodisperse nonspherical shape. *Langmuir*, 27(20):12304–12311, 2011.

[11] K. Lee, J. Look, M. T. Harris, and A. V. McCormick. Assessing extreme models of the stöber synthesis using transients under a range of initial composition. *Journal of colloid and interface science*, 194(1):78–88, 1997.

[12] D. Pontoni, T. Narayanan, and A. R. Rennie. Time-resolved saxs study of nucleation and growth of silica colloids. *Langmuir*, 18(1):56–59, 2002.

[13] K. Lee, A. N. Sathyagal, and A. V. McCormick. A closer look at an aggregation model of the stöber process. *Colloids and Surfaces A: Physicochemical and Engineering Aspects*, 144(1-3):115–125, 1998.

[14] S. Carroll, E. Mroczek, M. Alai, and M. Ebert. Amorphous silica precipitation (60 to 120°C): Comparison of laboratory and field rates. *Geochimica et Cosmochimica Acta*, 62(8):1379–1396, 1998.

[15] R. L. Brutchey and D. E. Morse. Silicatein and the translation of its molecular mechanism of biosilicification into low temperature nanomaterial synthesis. *Chemical reviews*, 108(11):4915–4934, 2008.

[16] M. Hildebrand. Biological processing of nanostructured silica in diatoms. *Progress in Organic Coatings*, 47(3-4):256–266, 2003.

[17] D. Volkmer. Von Biomineralien zu biomimetischen Materialien: Der Weg ist das Ziel. *Chemie in unserer Zeit*, 33(1):6–19, 1999.

[18] S. V. Patwardhan, S. J. Clarson, and C. C. Perry. On the role(s) of additives in bioinspired silicification. *Chemical communications (Cambridge, England)*, (9): 1113–1121, 2005.

[19] T. Ookoshi and M. Onaka. A remarkable Mo catalyst for olefin metathesis: Hexagonal mesoporous silica-supported molybdenum oxide (MoO_3/HMS). *Chemical Communications*, (21):2399–2400, 1998.

[20] S. A. Pelster, F. Schuth, and W. Schrader. Detailed study on the use of electrospray mass spectrometry to investigate speciation in concentrated silicate solutions. *Analytical chemistry*, 79(15):6005–6012, 2007.

[21] R. Y. Ning. Reactive silica in natural waters — a review. *Desalination and Water Treatment*, 21(1-3):79–86, 2010.

[22] R. K. Iler. *The chemistry of silica: Solubility, polymerization, colloid and surface properties, and biochemistry*. Wiley, New York, 1979.

[23] A. Pavlova, T. T. Trinh, R. A. van Santen, and E. J. Meijer. Clarifying the role of sodium in the silica oligomerization reaction. *Physical Chemistry Chemical Physics*, 15(4):1123–1129, 2013.

[24] E. Weitz, H.-G. Franck, and M. Giller. Untersuchungen an Kieselsäuren. *Zeitschrift für anorganische und allgemeine Chemie*, 331(5-6):249–255, 1964.

[25] S. A. Pelster, W. Schrader, and F. Schuth. Monitoring temporal evolution of silicate species during hydrolysis and condensation of silicates using mass spectrometry. *Journal of the American Chemical Society*, 128(13):4310–4317, 2006.

[26] S. A. Pelster, B. Weimann, B. B. Schaack, W. Schrader, and F. Schuth. Dynamics of silicate species in solution studied by mass spectrometry with isotopically labeled compounds. *Angewandte Chemie (International ed. in English)*, 46(35): 6674–6677, 2007.

[27] G. B. Alexander. The polymerization of monosilicic acid. *J. Am. Chem. Soc*, 76 (8):2094–2096, 1954.

[28] C. Okkerse. Submicroporous and macroporous silica, 1961.

[29] H. Baumann. Polymerisation und Depolymerisation der Kieselsäure unter verschiedenen Bedingungen. *Kolloid-Zeitschrift*, (162):28–35, 1959.

[30] G. B. Alexander. The effect of particle size on the solubility of amorphous silica in water. *The Journal of Physical Chemistry*, 61(11):1563–1564, 1957.

[31] A. R. Marsh, III, G. Klein, and T. Vermeulen. *Polymerization kinetics and equilibria of silicic acid in aqueous systems*. 1975.

[32] A. G. Walton. Nucleation of crystals from solution: Mechanisms of precipitation are fundamental to analytical and physiological processes. *Science (New York, N.Y.)*, 148(3670):601–607, 1965.

[33] A. C. Makrides, M. J. Turner, and J. Slaughter. Condensation of silica from supersaturated silicic acid solutions. *Journal of Colloid and Interface Science*, (73): 345–367, 1980.

[34] G. Engelhardt, W. Altenburg, D. Hoebbel, and W. Wieker. ^{29}Si-NMR-Spektroskopie an Silicatlösungen. IV. Untersuchungen zur Kondensation der Monokieselsäure. *Z. Anorg. Allg. Chem. (Zeitschrift für anorganische und allgemeine Chemie)*, 428(1):43–52, 1977.

[35] G. Engelhardt, W. Altenburg, D. Hoebbel, and W. Wieker. ^{29}Si-NMR-Spektroskopie an Silicatlösungen. V. Über die ^{29}Si-NMR-Spektren niedermolekularer Kieselsäuren. *Z. Anorg. Allg. Chem. (Zeitschrift für anorganische und allgemeine Chemie)*, 437(1):249–252, 1977.

[36] E. Richardson, J. A. Waddams. Use of silico-molybdate reaction to investigate the polymerization of low molecular weight silicic acids in dilute solutions. *Res. Corresp.*, S43(7), 1954.

[37] H.P Rothbaum and A.G Rohde. Kinetics of silica polymerization and deposition from dilute solutions between 5 and 180°C. *Journal of Colloid and Interface Science*, 71(3):533–559, 1979.

[38] O. Weres, A. Yee, and L. Tsao. Kinetics of silica polymerization. *Journal of Colloid and Interface Science*, 84(2):379–402, 1981.

[39] G. A. Icopini, S. L. Brantley, and P. J. Heaney. Kinetics of silica oligomerization and nanocolloid formation as a function of pH and ionic strength at 25°C. *Geochimica et Cosmochimica Acta*, 69(2):293–303, 2005.

[40] S. A. Greenberg and D. Sinclair. The polymerization of silicic acid. *The Journal of Physical Chemistry*, 59(5):435–440, 1955.

[41] R. C. Merrill and R. W. Spencer. The Gelation of Sodium Silicate. Effect of Sulfuric Acid, Hydrochloric Acid, Ammonium Sulfate, and Sodium Aluminatetrinht. *The Journal of Physical and Colloid Chemistry*, 54(6):806–812, 1950.

[42] T. M. Davis, T. O. Drews, H. Ramanan, C. He, Jingshan D., H. Schnablegger, M. A. Katsoulakis, E. Kokkoli, A. V. McCormick, R. L. Penn, and M. Tsapatsis. Mechanistic principles of nanoparticle evolution to zeolite crystals. *Nature Materials*, 5 (5):400–408, 2006.

[43] T. T. Trinh, A. P. J. Jansen, R. A. van Santen, and E. Jan Meijer. The role of water in silicate oligomerization reaction. *Physical Chemistry Chemical Physics*, 11(25): 5092–5099, 2009.

[44] T. T. Trinh, A. P. J. Jansen, R. A. van Santen, J. VandeVondele, and E. J. Meijer. Effect of counter ions on the silica oligomerization reaction. *ChemPhysChem*, 10 (11):1775–1782, 2009.

[45] X.-Q. Zhang, T. T. Trinh, R. A. van Santen, and A. P. J. Jansen. Mechanism of the initial stage of silicate oligomerization. *Journal of the American Chemical Society*, 133(17):6613–6625, 2011.

[46] D. J. Tobler, S. Shaw, and L. G. Benning. Quantification of initial steps of nucleation and growth of silica nanoparticles: An in-situ SAXS and DLS study. *Geochimica et Cosmochimica Acta*, 73(18):5377–5393, 2009.

[47] C. Noguera, B. Fritz, and A. Clement. Precipitation mechanism of amorphous silica nanoparticles: A simulation approach. *Journal of colloid and interface science*, 448:553–563, 2015.

[48] D. J. Tobler and L. G. Benning. In situ and time resolved nucleation and growth of silica nanoparticles forming under simulated geothermal conditions. *Geochimica et Cosmochimica Acta*, 114:156–168, 2013.

[49] D. Kashchiev. Solution of the non-steady state problem in nucleation kinetics. *Surface Science*, 14(1):209–220, 1969.

[50] D. Kashchiev. *Nucleation: Basic Theory with Apllications*. Butterworth-Heinemann, Boston, 2000.

[51] P. G. Vekilov. Nucleation. *Crystal Growth & Design*, 10(12):5007–5019, 2010.

[52] J. Čejka, A. Corma, and S. Zones. *Zeolites and catalysis: Synthesis, reactions and applications*. Wiley-VCH and [John Wiley, distributor], Weinheim and [Chichester], 2010.

[53] J. W. Gibbs. On the equilibrium of heterogeneous substances, transactions connecticut academy of sciences 3, 1876. In *The collected works*, volume 1, pages 108–248. Longmans & Green New York–London–Toronto, 1928.

[54] M. Volmer and A. Weber. Keimbildung in übersättigten Gebilden. *Zeitschrift für Physikalische Chemie*, (119):277–301, 1926.

[55] R. Becker and W. Döring. Kinetische Behandlung der Keimbildung in übersättigten Dämpfen. *Annalen der Physik*, (24):719–752, 1935.

[56] D. T. Robb and V. Privman. Model of nanocrystal formation in solution by burst nucleation and diffusional growth. *Langmuir*, 24(1):26–35, 2008.

[57] M. v. Smoluchowski. Versuch einer mathematischen Theorie der Koagulationskinetik kolloider Lösungen. *Zeitschrift für Physikalische Chemie*, (92):129–168, 1917.

[58] G. H. Weiss. Overview of theoretical models for reaction rates. *Journal of Statistical Physics*, 42(1-2):3–36, 1986.

[59] B. Chu. *Laser Light Scattering*. Academic Press, Inc., Boston, second edition edition, 1991.

[60] P. Kratochvil. *Classical Light Scattering From Polymer Solutions*. Elsevier, Amsterdam, 1987.

[61] M.B. Huglin. *Light Scattering From Polymer Solutions*. Academic Press, Inc., 1972.

[62] B. H. Zimm. Apparatus and methods for measurement and interpretation of the angular variation of light scattering; preliminary results on polystyrene solutions. *The Journal of Chemical Physics*, 16(12):1099–1116, 1948.

[63] A. Guinier and G. Fournet. *Small-angle scattering of X-rays*. Wiley, 1955.

[64] J. J. Hermans and S. Levinson. Some geometrical factors in light-scattering apparatus. *Journal of the Optical Society of America*, 41(7):460, 1951.

[65] Th. Neugebauer. Berechnung der Lichtzerstreuung von Fadenkettenlösungen. *Annalen der Physik*, 434(7-8):509–533, 1943.

[66] P. Debye. Molecular-weight determination by light scattering. *The Journal of Physical Chemistry*, 51(1):18–32, 1947.

[67] L. Rayleigh. On the diffraction of light by spheres of small relative index. *Proceedings of the Royal Society A: Mathematical, Physical and Engineering Sciences*, 90 (617):219–225, 1914.

[68] A.J.F. Siegert. On the fluctuations in signals returned by many independently moving scatteres. *MIT Radiation Laboratory Report*, (465):1–14, 1943.

[69] B. J. Berne and R. Pecora. *Dynamic Light Scattering: With Applications to Chemistry, Biology and Physics*. Dover Publications, New York, 2000.

[70] D. E. Koppel. Analysis of macromolecular polydispersity in intensity correlation spectroscopy: The method of cumulants. *The Journal of Chemical Physics*, 57(11): 4814–4820, 1972.

[71] W.. Burchard, M. Schmidt, and W. H. Stockmayer. Information on polydispersity and branching from combined quasi-elastic and intergrated scattering. *Macromolecules*, 13(5):1265–1272, 1980.

[72] W. Burchard, editor. *Static and dynamic light scattering from branched polymers and biopolymers*, volume 48 of *Advances in polymer science*. Springer-Verlag, Berlin, 1983. ISBN 978-3-540-12030-8.

[73] M. Schmidt and W. Burchard. Translational diffusion and hydrodynamic radius of unperturbed flexible chains. *Macromolecules*, 14(1):210–211, 1981.

[74] M. Schmidt. Combined integrated and dynamic light scattering by poly(γ-benzyl glutamate) in a helicogenic solvent. *Macromolecules*, 17(4):553–560, 1984.

[75] N. Donkai, H. Inagaki, K. Kajiwara, H. Urakawa, and M. Schmidt. Dilute solution properties of imogolite. *Die Makromolekulare Chemie*, 186(12):2623–2638, 1985.

[76] J. Liu, S. Pancera, V. Boyko, A. Shukla, T. Narayanan, and K. Huber. Evaluation of the particle growth of amorphous calcium carbonate in water by means of the porod invariant from saxs. *Langmuir*, 26(22):17405–17412, 2010.

[77] J. Liu, J. Rieger, and K. Huber. Analysis of the Nucleation and Growth of Amorphous $CaCO_3$ by Means of Time-Resolved Static Light Scattering. *Langmuir*, 24 (15):8262–8271, 2008.

[78] Gernod Baur, SLS-Systemtechnik. Differential refractometer: E-mail, 31.07.2016.

[79] B. A. Brice and M. Halwer. A differential refractometer. *J. Opt. Soc. Am.*, (41): 1033–1037, 1951.

[80] T. Witte. Untersuchungen zur Aggregation mesoskopischer Systeme mittels zeitaufgelöster, statischer Lichtstreuung. 2005.

[81] A. Becker and M. Schmidt. Time-resolved, static light scattering: New possibilities in polymer characterization. *Makromolekulare Chemie. Macromolecular Symposia*, 50(1):249–260, 1991.

[82] A. D. Eaton, L. S. Clesceri, and A. E. Greenberg. *Standard methods for the examination of water and wastewater*. American Public Health Association, Washington and D.C, 20 edition, 1998.

[83] V. W. Truesdale and C. J. Smith. The formation of molybdosilicic acids from mixed solutions of molybdate and silicate. *Analyst*, (100):203–212, 1975.

[84] C. G. Bochet, T. Draper, B. Bocquet, M. T. Pope, and A. F. Williams. ^{182}tungsten Mossbauer spectroscopy of heteropolytungstates. *Dalton transactions (Cambridge, England : 2003)*, (26):5127–5131, 2009.

[85] Coradin, Th. Eglin, D. and J. Livage. The silicomolybdic acid spectrophotometric method and its application to silicate/biopolymer interaction studies. *Spectroscopy*, (18):567–576, 2004.

[86] H.-H. Perkampus. *UV-VIS Spectroscopy and Its Applications: With 78 Figures and 21 Tables*. Springer, Berlin, 1992.

[87] Scheme of sem set-up, 08.06.2017. URL {http://nptel.ac.in/courses/115103030/17}.

[88] Interaction volume sem, 08.06.2017. URL {http://www.ammrf.org.au/myscope/sem/background/concepts/interactions.php}.

[89] P. G. de Gennes and T. A. Witten. Scaling concepts in polymer physics. *Physics Today*, 33(6):51–54, 1980.

[90] Y. Ikeda, M. Beer, M. Schmidt, and K. Huber. Ca^{2+} and Cu^{2+} Induced Conformational Changes of Sodium Polymethacrylate in Dilute Aqueous Solution. *Macromolecules*, 31(3):728–733, 1998.

[91] M. Schmidt and W. H. Stockmayer. Quasi-elastic light scattering by semiflexible chains. *Macromolecules*, 17(4):509–514, 1984.

[92] B. B. Mandelbrot. *The fractal geometry of nature*. W.H. Freeman, San Francisco, 1982.

[93] T. A. Witten and L. M. Sander. Diffusion-limited aggregation, a kinetic critical phenomenon. *Physical Review Letters*, 47(19):1400–1403, 1981.

[94] P. Meakin. Formation of fractal clusters and networks by irreversible diffusion-limited aggregation. *Physical Review Letters*, 51(13):1119–1122, 1983.

[95] M. Kolb, R. Botet, and R. Jullien. Scaling of kinetically growing clusters. *Physical Review Letters*, 51(13):1123, 1983.

[96] M. Y. Lin, H. M. Lindsay, D. A. Weitz, R. Klein, R. C. Ball, and P. Meakin. Universal diffusion-limited colloid aggregation. *Journal of Physics: Condensed Matter*, 2(13):3093, 1990.

[97] P. Meakin. Aggregation kinetics. *Physica Scripta*, 46(4):295–331, 1992.

[98] T. Vicsek and F. Family. Dynamic scaling for aggregation of clusters. *Physical Review Letters*, 52(19):1669–1672, 1984.

[99] T. O. Drews and M. Tsapatsis. Model of the evolution of nanoparticles to crystals via an aggregative growth mechanism. *International Symposium on Zeolite and Microporous Crystals 2006*, 101(1–2):97–107, 2007.

[100] J. C. Lagarias, J. A. Reeds, M. H. Wright, and P. E. Wright. Convergence properties of the nelder–mead simplex method in low dimensions. *SIAM Journal on Optimization*, 9(1):112–147, 1998.

[101] A. Kempter, T. Gaedt, V. Boyko, S. Nied, and K. Hirsch. New insights into silica scaling on ro-membranes. *Desalination and Water Treatment*, 51(4-6):899–907, 2013.

[102] W. F. Polik and W. Burchard. Static light scattering from aqueous poly(ethylene oxide) solutions in the temperature range 20-90°C. *Macromolecules*, 16(6):978–982, 1983.

[103] R. Schweins and K. Huber. Collapse of sodium polyacrylate chains in calcium salt solutions. *The European Physical Journal E*, 5(1):117–126, 2001.

[104] R. Schweins, G. Goerigk, and K. Huber. Shrinking of anionic polyacrylate coils induced by Ca^{2+}, Sr^{2+} and Ba^{2+}: a combined light scattering and ASAXS study. *The European physical journal. E, Soft matter*, 21(2):99–110, 2006.

[105] S. Lages, R. Michels, and K. Huber. Coil-Collapse and Coil-Aggregation due to the Interaction of Cu^{2+} and Ca^{2+} Ions with Anionic Polyacrylate Chains in Dilute Solution. *Macromolecules*, 43(6):3027–3035, 2010.